NEAR-INFRARED SPECTROSCOPY AND MATHEMATICAL MODELING FOR THE CHARACTERIZATION OF HUMAN CEREBRAL HEMODYNAMICS IN THE MICROVASCULATURE

A dissertation submitted by

Kristen T. Tgavalekos

in partial fulfillment of the requirements for the degree of

Doctor of Philosophy
in
Biomedical Engineering

Tufts University

May 2018

Advisor:
Sergio Fantini, Ph.D, Department of Biomedical Engineering, Tufts University

Committee Members:
Irene Georgakoudi, Ph.D, Department of Biomedical Engineering, Tufts University
Brian Tracey, Ph.D, Department of Electrical Engineering, Tufts University
Joshua Kornbluth, M.D., Department of Neurology, Tufts Medical Center

Abstract

Near-infrared spectroscopy (NIRS), in combination with coherent hemodynamics spectroscopy (CHS), provides information about the cerebral microvasculature in terms of cerebral blood flow, cerebral blood volume, and the cerebral metabolic rate of oxygen. We characterize the frequency-dependent relationship between tissue concentrations of oxyhemoglobin and deoxyhemoglobin, measured with NIRS, as well as the relationship between total hemoglobin concentration and arterial blood pressure in healthy subjects. We use the hemodynamic model of CHS for the analysis of the results to yield physiologic parameters such as absolute cerebral blood flow and cerebral autoregulation. Further, we demonstrate the application of NIRS-CHS in the clinical setting of the neurocritical care unit.

Acknowledgements

I would first like to thank my advisor Sergio Fantini. I am grateful to have had an advisor who is kind and patient while also pushing his students to maintain the highest standards for research. I have learned a great deal from you about how to think critically and also how to clearly communicate research through writing, creating good figures, and presenting. Thank you also for your often open office door.

I'd like to thank Angelo Sassaroli. No matter how vague or specific of a question I've had, I knew I could go to you to discuss. Our shared interests in simulations and in exploring new ways of analyzing data has been the source of many valuable conversations.

I'd like to thank Irene Georgakoudi for your guidance and feedback throughout the years – from my first research proposal for biophotonics class to my original research proposal. Thank you to Brian Tracey for being an excellent teacher in my favorite class at Tufts – digital signal processing. Thank you to Joshua Kornbluth for providing the clinical perspective to this work. From conversations with you, I've learned about pathophysiology of neurocritical care patients and the kinds of innovations doctors would find valuable. The goal of this work has been to develop tools that can ultimately help doctors and their patients. Working in your unit has been motivational, and the experiences I've had there I will carry with me for the rest of my life. Thank you also to Xuemei Cai for your guidance in performing studies in the neurocritical care unit.

Thank you to my lab mates from over the years- especially Nishanth Krishnamurthy, Thao Pham, and Xuan Zang. We’ve spent a lot of time together in dark windowless rooms. I’m grateful for your help with experiments and troubleshooting. Thank you also to Jana Kainerstorfer and Pami Anderson for your guidance.

Thank you to the organizers of the GIFT program and the fellows in my cohort. This was one of the best experiences of my time in graduate school. Your varied passions and commitment to research and teaching inspired me.

Thank you to my mentors from Northeastern University- Dana Brooks, Waleed Meleis, Charles DiMarzio, Mark Niedre, and Rick Moore. Thank you Dr. Kopans for the wisdom you’ve shared. Thank you to the Gordon-CenSSIS research program. From the moment I saw the presentation about engineering research my freshman year, I had the thought “This is what I want to be doing” and you supported and fostered that excitement.

Thank you, Mom-throughout my academic career, you’ve helped in any way you could and have always been cheering me on. Dad, thank you for your support over the years and pushing me to take the challenging but rewarding path. Nora, thank you for being a role model from the beginning. You’ve helped me in countless ways and have provided an example of what it looks like to be a successful woman in engineering. Karl, thank you for the example you’ve set with your balance between a strong work ethic and enjoyment for the other fun things life has to offer. Thank you Mike and Keri, for being the best voluntary family members I could hope for. Alexa and Anna, thank you for the smiles and laughs. You’ve brightened my days so many times.

Thank you to my friends for your support and the fun times. Jessi, our home in Davis was the best way to start our post-undergrad lives. Your sunny disposition and our times relaxing by watching shows were so helpful. Thank you to Kristyn, Lauren (H) W, Lauren Z, Hilary, Alex, and Rachel.

Fernando, thank you for your support and patience. The bad days are more bearable, and the good days are even better, when I’m with you.

Table of Contents

Abstract ii

Acknowledgements iii

Table of Contents vi

List of tables viii

List of figures ix

Chapter 1: Introduction 1

- 1.1 Motivation 1
- 1.2 Dissertation overview 1
- 1.3 Cerebral hemodynamics 3
  - 1.3.1 Cerebrovascular physiology 3
  - 1.3.2 Cerebral blood flow 4
  - 1.3.3 Cerebral autoregulation 6
- 1.4 Near-infrared spectroscopy 10
  - 1.4.1 Relative measurements 13
  - 1.4.2 Absolute measurements 15
- 1.5 Oscillatory hemodynamics 16
- 1.6 Coherent hemodynamics spectroscopy 17
- 1.7 Time-frequency resolution 22

Chapter 2: Characterization of hemodynamic oscillations in healthy tissue 23

- 2.1 Introduction 23
- 2.2 Methods 26
  - 2.2.1 Human subjects and data acquisition 26
  - 2.2.2 Data analysis 28
- 2.3 Results 30
- 2.4 Discussion 36
- 2.5 Conclusion 41

Chapter 3: Frequency-resolved analysis of coherent oscillations of local cerebral blood volume and systemic mean arterial pressure 42

- 3.1 Introduction 42
- 3.2 Methods 48
  - 3.2.1 Subjects 48
  - 3.2.2 Experimental protocol and data acquisition 48

3.2.3 Time-varying coherence and coherence threshold 53
3.2.4 Time-averaged transfer function analysis.. 56
3.2.5 Model fitting 57
3.3 Results 58
3.3.1 Single probe location 58
3.3.2 Spatial mapping 63
3.3.3 Comparison of thigh cuff oscillation protocols 65
3.4 Discussion 69
3.5 Conclusion.. 76
Chapter 4: Coherent hemodynamics spectroscopy in the neurocritical care unit ..77
4.1 Introduction 77
4.2 Methods.. 77
4.2.1 Data collection 77
4.2.2 Data analysis... 80
4.3 Results 85
4.4 Discussion 93
4.5 Conclusion.. 94
Chapter 5: Future directions...96
5.1 Responses to carbon dioxide 96
5.2 New protocols and spontaneous oscillations 98
5.3 Association of cerebral blood flow and autoregulation with outcomes in the neurocritical care unit 100
5.4 Future outlook 101
Funding acknowledgements..105
Appendix..106
References..113

List of tables

Table 1. Explanation of terms and parameters in hemodynamic model............... 18
Table 2**.** Contributions of volume and flow phasors to O(ω) and D(ω)................ 38
Table 3. Group average and standard error for amplitude and phase between Δ[HbT] and ΔMAP.. 61
Table 4. Expected responses to hypo- and hypercapnia. 97

List of figures

Figure 1.1. Static autoregulation curve. 8
Figure 1.2. Characteristic healthy response of CBF to drop in MAP. 9
Figure 1.3. Example optical probe for assessing prefrontal cortex 11
Figure 1.4. Extinction spectra of oxyhemoglobin and deoxyhemoglobin. 12
Figure 2.1. Experimental setup for study of breast and brain tissue. 27
Figure 2.2. Example of time traces from experiment. 31
Figure 2.3. Group averaged CHS spectra for breast and brain tissue. 32
Figure 2.4. Zoomed in oscillations and phasor diagram 34
Figure 3.1. Flow chart of methods for [HbT] and MAP study 48
Figure 3.2. Spatial mapping probe diagram. 50
Figure 3.3. Example of time traces from experiment. 52
Figure 3.4. Time traces for chirp-like portion of protocol 53
Figure 3.5. Coherence between ΔMAP and Δ[HbT]. 59
Figure 3.6. Binary coherence maps. 59
Figure 3.7. 2D transfer function analysis results 60
Figure 3.8. Transfer functions for 5 representative subjects. 62
Figure 3.9. Parameters for 22 subjects. 63
Figure 3.10. Transfer functions for 8 channels from a subject 64
Figure 3.11. Box plots for subjects with the spatial mapping probe 65
Figure 3.12. Comparison of four protocols/fitting approaches 66
Figure 3.13. Time domain fit of Δ[HbT] 67
Figure 3.14. Comparison of protocols with Bland-Altman plots 68
Figure 3.15. Comparison of transfer functions 69
Figure 4.1. Experimental set up in the neurocritical care unit. 79
Figure 4.2. Time traces from experiment. 79
Figure 4.3 Flow chart of methods 81
Figure 4.4. Coherence maps for NCCU subject. 86
Figure 4.5. Binary coherence for NCCU subject 86
Figure 4.6. 2D transfer function analysis results for Δ[HbO] and Δ [Hb]. 87
Figure 4.7. 2D transfer function analysis results for Δ [HbT] and ΔMAP 88
Figure 4.8 Transfer function and points for ΔMAP and Δ[HbT]. 89
Figure 4.9 Transfer function and points for map and cbv. 90
Figure 4.10. Transfer function and points for Δ[HbO] and Δ[Hb]. 91
Figure 4.11. Time traces of CBF and CPP. 93
Figure 4.12. Static autoregulation curve with NCCU data 94
Figure 5.1. Coherence between ΔABP and Δ[HbT] for Subject 5 to 1.7 Hz. 103
Figure 5.2. Binary coherence between ΔABP and Δ[HbT] for Subject 5. 104
Figure 5.3. Zoomed in binary coherence between ΔABP and Δ[HbT] 105

Chapter 1: Introduction

1.1 Motivation

"Life is not possible without air and water not only because of their chemical ingredients but also, in fact more so, because of the fluidity of air and water [1]."

The appropriate movement of blood within the body is critical to human health. This is especially true for the brain. According to the Centers for Disease Control and Prevention, cerebrovascular disease is the 5th leading cause of death in the United States [2]. There is a need for a tool that can perform non-invasive, portable, and real-time monitoring of cerebral blood flow and blood volume at the hospital bedside to provide physicians with quantitative feedback on the cerebral health status of their patients. Near-infrared spectroscopy (NIRS) in combination with coherent hemodynamics spectroscopy (CHS) has potential to meet these needs. Our goal has been to develop a robust approach for NIRS-CHS that has utility in a clinical setting. Continuous monitoring of cerebral tissue status may enable the study of the mechanisms of a disease or injury, the detection of a disease, recovery monitoring for prevention of secondary injury, or evaluation of the effects of different treatments.

1.2 Dissertation overview

The work in this dissertation aims to characterize the oscillatory hemodynamics in humans that can be measured locally with near-infrared spectroscopy (NIRS) and systemically with continuous arterial blood pressure monitoring. The transfer functions between these measurements are in part dictated by cerebral blood flow (CBF) and cerebral autoregulation (CA). The key contributions of this work are: implementation of coherence thresholding for selecting frequencies for analysis in CHS, development of a transfer function analysis approach for CHS in the time-frequency domain, and incorporation of arterial blood pressure information in a hemodynamic model. The introduction begins with a description of the relevant brain physiology followed by a description of the mechanics of CBF and CA and the techniques used to measure them. Next, we introduce the principles of NIRS. Then, the value of using oscillations of blood flow, blood volume, oxyhemoglobin and/or deoxyhemoglobin to characterize cerebral health is described. Following that, we show how oscillatory oxy- and deoxyhemoglobin, measured with NIRS, can be analyzed with an approach called coherent hemodynamics spectroscopy (CHS) to quantitatively assess CBF and CA. We also provide background information about the trade-off between time and frequency resolution which will be relevant to the data analysis approaches used in this work. In Chapter 2, we present the typical relationships we measure between oxy- and deoxyhemoglobin in brain tissue as well as in breast tissue. We describe how the hemodynamic model of CHS can be used to interpret the differences in the results. In Chapter 3, we characterize the relationship between local cerebral blood volume and systemic arterial blood pressure in a group of healthy subjects. We present a physiologic model to relate the oscillations between the two signals. In Chapter 4, we present initial results from applying our techniques to patients in a neurocritical care unit. The dissertation concludes with a description of the potential future directions for this work. Refer to Table A.1 in the Appendix for a list of acronyms used in this work.

1.3 Cerebral hemodynamics

1.3.1 Cerebrovascular physiology

First, we describe the path of blood as it is transported throughout the brain. Blood flow to the brain is supplied by the right and left common carotid arteries and the right and left vertebral arteries. At the base of the brain, the supplying arteries join together in a ring called the Circle of Willis [3]. The common carotid arteries divide into external carotid arteries and internal carotid arteries. The largest branches of the internal carotid arteries are the left and right middle cerebral arteries which contribute to the blood supply of the frontal, parietal, and temporal lobes of the brain. The large arteries supplying blood to the brain, described up to now, are called the macrovasculature. The macrovasculature divides into progressively smaller branches: the pial arteries, the penetrating arteries, and then the penetrating arterioles [4]. The arterioles can regulate blood flow to the brain via changes in their diameter (see Sections 1.3.2 and 1.3.3). The arterioles connect to networks of capillaries, the sites at which oxygen and other nutrient exchange occur and cellular wastes are removed. After the capillaries, the vessels converge into small veins called venules. Veins are more compliant than arteries and may passively respond to changes in blood volume and blood flow induced by arteriole diameter alterations [5]. The arterioles, capillaries, and venules are called the microvasculature. To drain blood from the brain, the venules join together into larger veins which eventually connect to the dural venous sinuses. In addition to receiving blood, the dural venous sinuses reabsorb cerebral spinal fluid (CSF) [3]. The dural venous sinuses then connect to the internal jugular veins.

The next key aspect of brain physiology is the Monroe- Kellie doctrine which states that within the rigid cranial vault (skull) the total volume of the contents (brain tissue, blood, and CSF) is fixed [6]. Therefore, an increase in volume for any of these intracranial components must be compensated with a decrease in volume of another component in the healthy human brain. An increase in volume beyond what the body can compensate for will result in a rise in intracranial pressure (ICP). The gradient between mean arterial pressure (MAP) and ICP determines the cerebral perfusion pressure (CPP):

$$CPP = MAP - ICP \tag{1.1}$$

From Equation 1.1, we can see that an increase in ICP will reduce CPP if there is not any alteration in MAP. Typical ICP values are around 10 mmHg. Invasive ICP monitoring in acute neurologic injuries such as traumatic brain injury (TBI) and subarachnoid hemorrhage (SAH) is often indicated so that counteractions to reduce ICP can be performed if it is found to increase over a threshold of 20 mmHg. Because ICP can be measured in real-time at the bedside, its measurement enables the computation of CPP as a surrogate for cerebral blood flow (CBF). In Section 1.3.2 , we provide the definition of CBF, which is often the cerebral signal that neurocritical care physicians are most interested in.

1.3.2 Cerebral blood flow

CBF is related to CPP with the following relationship:

$$CBF = \frac{CPP}{CVR} \tag{1.2}$$

where CVR is the cerebrovascular resistance. Blood flow describes the milliliters of blood delivered to 100 grams of tissue within 1 minute. Adequate blood flow to brain tissue is critical for ensuring that the brain receives the oxygen and glucose it needs to meet its high energy demands. In human cerebral tissue, the healthy value for mean blood flow is around 50 $ml_{blood}/100g_{tissue}/min$ [7], with higher values in gray matter and lower values in white matter. Both hypoperfusion and hyperperfusion are dangerous to the brain. Hyperfusion could give rise to increased ICP. When CBF is less than 20 $ml_{blood}/100g_{tissue}/min$, hypoperfusion leads to ischemia. A CBF below 5 $ml_{blood}/100g_{tissue}/min$ leads to cell death [6]. CBF can move outside of a safe range for chronic central nervous system diseases (e.g. Alzheimer's disease, Parkinson's disease, schizophrenia [8]) as well as acute central nervous system diseases. (e.g. TBI, SAH, acute ischemic stroke [8]).

There are several clinical and experimental technologies for measuring CBF which fall into the categories of intravascular measurements, nuclear medicine, x-ray imaging, magnetic resonance imaging (MRI), ultrasound, thermal diffusion, and biomedical optics [8]. Position emission tomography (PET) is in the category of nuclear medicine, and it is the gold standard for in vivo measurement of CBF. It is minimally invasive in that it requires injection or inhalation of a radioactive diffusible contrast agent or tracer. It provides a snapshot of localized CBF with a resolution of 4-6 mm [9]. PET is one of the most expensive imaging modalities, so it initially was preferred as a research tool instead of a clinical tool. However, innovations in its technology, for example more affordable gamma cameras, have begun to make it a more appealing option for clinical use [10]. Methods based on x-ray imaging (Xenon-enhanced computed tomography and perfusion computed tomography) and MRI (dynamic susceptibility MRI and arterial spin labeling MRI) are also capable of providing in vivo localized measurement of CBF. Application of these imaging modalities can be logistically challenging, especially for patients in the neurocritical care unit who would benefit from frequent blood flow measurements. The patients need to be physically transported to the imaging centers, need to be exposed to radiation in the case of x-ray imaging, or may incur large costs in the case of MRI. For these reasons, noninvasive and portable approaches are more viable for scenarios in which frequent CBF measurements are necessary.

Transcranial Doppler ultrasound (TCD) measures cerebral blood flow velocity (CBFV) in units of cm/s in the macrovasculature (middle cerebral arteries, primal anterior cerebral arteries, or posterior cerebral arteries) [11]. It is the current tool of choice when noninvasive bedside measurements of CBF are desired. The ultrasound transducer is placed in a subject-specific ultrasonic window in the temporal region above the zygomatic arch called the transtemporal window for access to the arteries. CBFV recordings are useful for diagnosing patients at risk or who already have cerebral vasospasm, a constriction of a blood vessel [12]. We will discuss some of the limitations of TCD in Section 3.1.

Non-invasive blood flow monitoring techniques in biomedical optics, such as diffuse correlation spectroscopy (DCS) and NIRS, offer sensitivity to the microvasculature rather than the macrovasculature. Both DCS and NIRS have a spatial resolution on the order of 1 cm, and the maximum tissue depth that can be probed is 2-3 cm. NIRS is described in more detail in Section 1.4. For a thorough review of DCS and NIRS techniques for measuring cerebral blood flow, we refer to Fantini et al [8].

1.3.3 Cerebral autoregulation

Cerebral autoregulation (CA) is the mechanism in the brain that maintains constant CBF despite changes in CPP. Often MAP is used as a surrogate for CPP with the assumption that ICP remains constant and low (see Equation 1.1). Brain injury can reduce the effectiveness of CA, making the brain more sensitive to pressure dynamics. Specifically, the brain would be more at risk of hypoperfusion in the case of a decrease in MAP, and more at risk of hyperperfusion in the case of an increase in MAP.

1.3.3.1 Static autoregulation

Static autoregulation is the ability of the brain to maintain a constant absolute CBF despite changes in the absolute value of MAP. Figure 1.1 provides a depiction of the relationship between MAP and CBF during functional static autoregulation. CBF remains at a value of about 50 $ml_{blood}/100g_{tissue}/min$ within a range of MAP between about 50 and 150 mmHg. Referring to Equation 1.1 and Equation 1.2, we can see that this regulation must be due to changes in CVR, assuming ICP is constant and low. CVR is altered by the arterioles which have the ability to dilate, reducing resistance to flow, or constrict, increasing resistance to flow. The controlling mechanisms for the constriction and dilation of arterioles is still an active area of research, with studies indicating contributions from neural, metabolic, and myogenic sources [3]. Outside the bounds of functional autoregulation, Figure 1.1 shows that CBF and MAP become proportional. In individuals with less effective autoregulation, the plateau region of the curve may become narrower or the curve itself may shift to the left or right such that autoregulation only functions at lower than usual or higher than usual MAP, respectively [3].

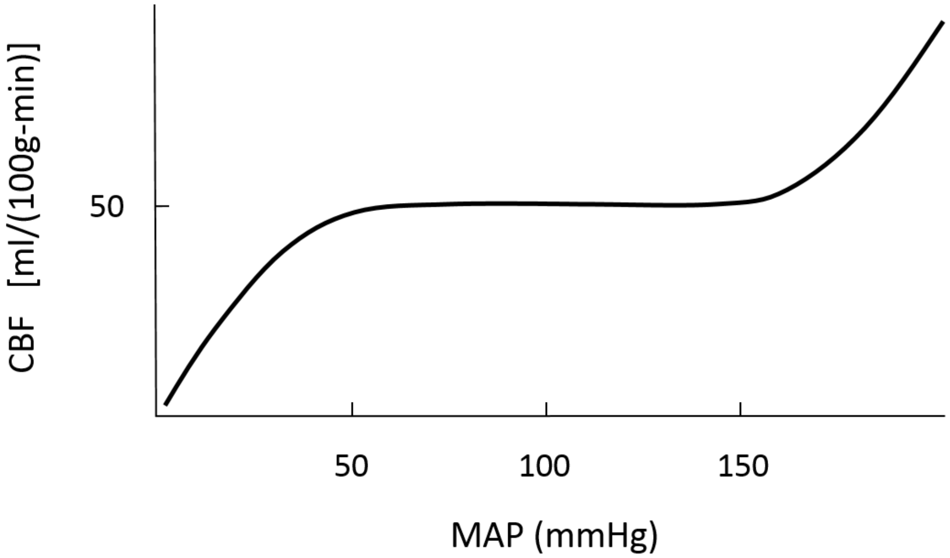

Figure 1.1. Healthy static autoregulation curve.

1.3.3.2 Dynamic autoregulation

Dynamic cerebral autoregulation is the ability of CBF to respond to transient changes in MAP. Rather than absolute values, it requires relative measurements of MAP and CBF with a high sample rate (at least 1 Hz). One of the early studies to quantify dynamic CA was performed by Aaslid et al [13]. CBFV was measured in a middle cerebral artery of healthy humans and real time blood pressure was also synchronously measured. Cuffs were placed around both thighs and inflated above arterial pressure in order to occlude blood flow to the legs. Upon release of the cuffs after a few minutes, hyperemia was induced in which blood flow rushed to the legs and peripheral vascular resistance throughout the body was reduced. Correspondingly, MAP was rapidly reduced. This type of response is illustrated in Figure 1.2 in which MAP decreases by 20% at time= 0 s. This systemic reduction of arterial pressure causes a fast drop in CBF as well. In the case of functional autoregulation, CBF will begin to recover from this drop before MAP, with both signals returning to baseline within 15-20 seconds. The plateau of MAP in Figure 1.2 indicates when CA is independently driving the recovery of CBF. When MAP begins to recover, there is contribution to CBF due to the baroreceptor reflex as well. In the case of absent CA, CBF and MAP would follow the same timing for recovery.

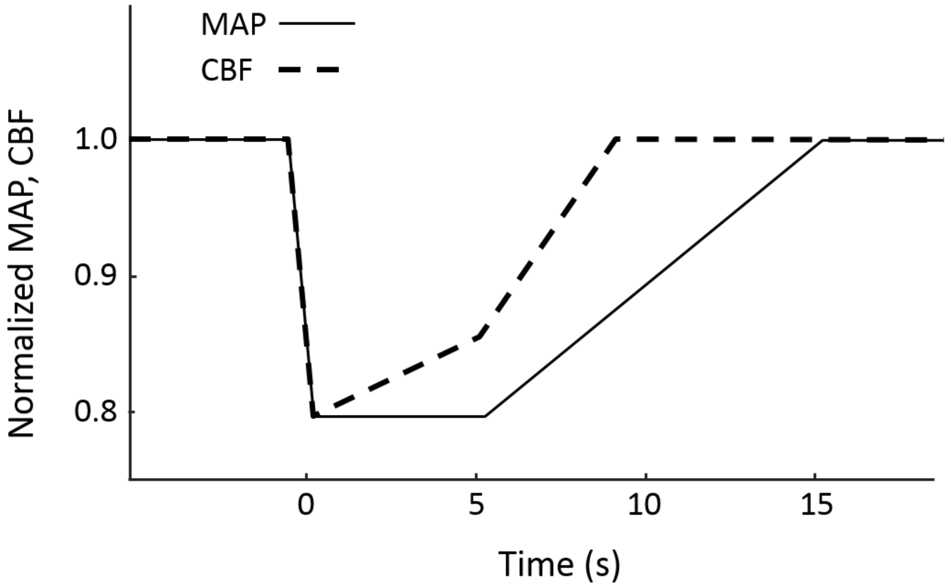

Figure 1.2. Characteristic healthy response of CBF to drop in MAP.

Another popular way to quantify CA is with transfer function analysis (TFA) [14]. When using TFA for the assessment of autoregulation, MAP or arterial blood pressure (ABP) is set as the input to the system and CBF is set as the output to the system. The gain and phase of the transfer function between these two signals may then be related to the efficiency of autoregulation at different frequencies. A low gain indicates an efficient autoregulation, because it indicates attenuation of the effect MAP amplitude changes have on CBF. A positive phase shift of CBF relative to MAP, meaning that CBF oscillations lead MAP oscillations, is also indicative of a functioning autoregulation, because CBF recovers before MAP displacement, while in-phase CBF and MAP indicates damaged autoregulation [15].

1.4 Near-infrared spectroscopy

Near-infrared spectroscopy (NIRS) is an optical method, using wavelengths in the range of 650-1000 nm, for local measurements of the absorption and scattering properties of biological tissue. NIRS is non-invasive, portable, and relatively inexpensive which makes it an appealing tool for clinical applications. Its high sample rate, within the range of 10 to 50 Hz, is suitable for capturing the fast dynamics of heart rate pulsations in tissue. Its spatial resolution is on the order of 1 cm due to the diffuse nature of light in tissue within this range of wavelengths. One of the challenges in using NIRS noninvasively is that measurements are contaminated by contributions of absorption in the extracerebral layer [16]. Two-layer diffusion models, short and long source-detector separations, and other approaches for separating extracerebral contributions are an active area of research in the field.

Figure 1.3 shows an example of a custom NIRS probe placed on the forehead in order to measure optical changes in the tissue of the prefrontal cortex. Light is transmitted through optical fibers and after propagating through tissue, is absorbed by chromophores in the tissue or collected by detectors placed centimeters away.


[redacted]

Figure 1.3. Example optical probe for assessing prefrontal cortex.

The light used in NIRS can penetrate several centimeters deep within tissue due to its low probability of absorption. The reduced scattering coefficient, μ_s', is the probability of scattering per unit path length (considering scattering anisotropy) and is often presented in units of cm^{-1}. Typical values for the scattering coefficient in brain tissue are on the order of 5 cm^{-1} [17]. Differential absorption of light within the tissue at different wavelengths enables computation of concentrations of absorbers. The absorption coefficient, μ_a, is the probability of absorption per unit path length and is often presented in units of cm^{-1}. Typical values for the absorption coefficient in brain tissue are on the order of 0.1 cm^{-1} [17]. The coefficient μ_a depends on the product of the molar concentration of the absorber, in units of M (moles/L), and its molar extinction coefficient, ε, in units of cm^{-1}/M. The absorption coefficient, μ_a, of multiple absorbers, i, is the weighted sum of their concentrations, C_i, and respective extinction coefficients, ε_i: $\mu_a = \sum_i \varepsilon_i C_i$ [18].

Two of the dominant absorbers within the near-infrared window are oxyhemoglobin (HbO) and deoxyhemoglobin (Hb). Hemoglobin is the protein in red blood cells that is responsible for oxygen transport. It is called oxyhemoglobin when oxygen is bound to it, and it is called deoxyhemoglobin upon its release of oxygen molecules. Specifically, the heme group is the component of hemoglobin in which oxygen is bound and released. Each hemoglobin molecule has four heme groups capable of binding one molecule of oxygen. Figure 1.4 shows the distinct wavelength dependent molar extinction coefficients, $\varepsilon(\lambda)$, of oxyhemoglobin (HbO) and deoxyhemoglobin (Hb). The measurements of concentrations of [HbO] and [Hb] in tissue have been used for a variety of applications such as functional brain imaging [19] and breast cancer imaging [20], [21].

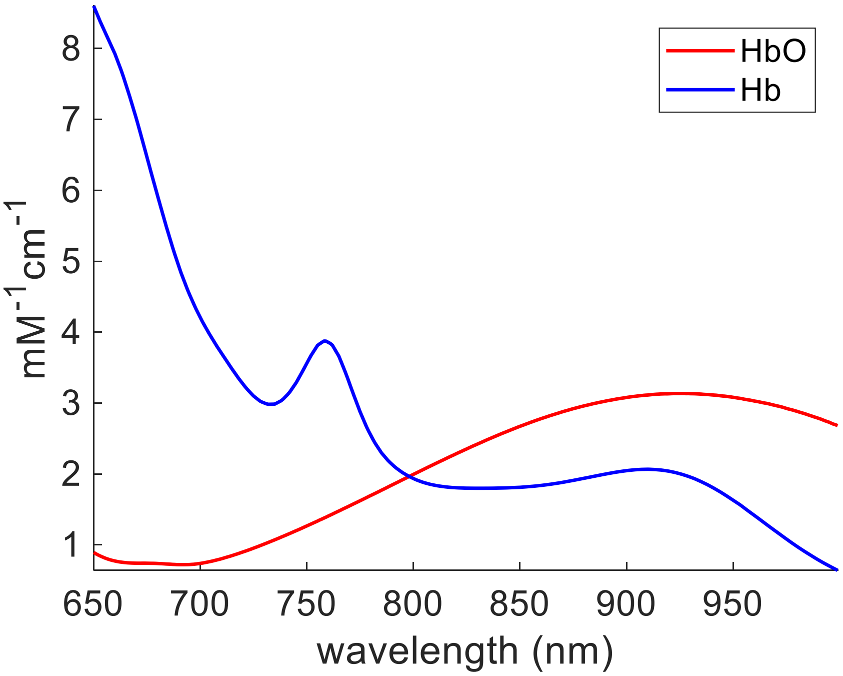

Figure 1.4. Molar extinction spectra, ε, of oxyhemoglobin (HbO) and deoxyhemoglobin (Hb). Generated from [22].

The concentrations of HbO, Hb and total hemoglobin (HbT) depend on the absorption at different wavelengths and the extinction coefficients in the following way:

$$[\mathrm{HbO}] = \frac{\varepsilon_{\mathrm{Hb}}(\lambda_2)\mu_a(\lambda_1) - \varepsilon_{\mathrm{Hb}}(\lambda_1)\mu_a(\lambda_2)}{\varepsilon_{\mathrm{HbO}}(\lambda_1)\varepsilon_{\mathrm{Hb}}(\lambda_2) - \varepsilon_{\mathrm{HbO}}(\lambda_2)\varepsilon_{\mathrm{Hb}}(\lambda_1)} \qquad (1.3)$$

$$[\mathrm{Hb}] = \frac{\varepsilon_{\mathrm{HbO}}(\lambda_1)\mu_a(\lambda_2) - \varepsilon_{\mathrm{HbO}}(\lambda_2)\mu_a(\lambda_1)}{\varepsilon_{\mathrm{HbO}}(\lambda_1)\varepsilon_{\mathrm{Hb}}(\lambda_2) - \varepsilon_{\mathrm{HbO}}(\lambda_2)\varepsilon_{\mathrm{Hb}}(\lambda_1)} \qquad (1.4)$$

$$[\mathrm{HbT}] = [\mathrm{HbO}] + [\mathrm{Hb}]. \qquad (1.5)$$

From the above equations we can see that, with knowledge of the extinction spectra of [HbO] and [Hb] ($\varepsilon_{\mathrm{HbO}}(\lambda)$and $\varepsilon_{\mathrm{Hb}}(\lambda)$,respectively) and with measurement of their absolute absorption coefficients ($\mu_a(\lambda)$) for at least two wavelengths via NIRS, we may solve for the tissue concentrations, [HbO] and [Hb]. Here we have shown how to estimate the concentrations of two chromophores. To estimate the concentrations of N chromophores, μ_a, must be determined at N or more wavelengths.

1.4.1 Relative measurements

Changes in measured light intensity can be used to compute relative changes in the concentrations of HbO and Hb with the modified Beer-Lambert Law [23]. We have used this approach throughout this work due to our interest in oscillations of [HbO] and [Hb]. To begin with, optical density of a material is related to the change in transmitted DC light intensity, I_o, versus detected light intensity, I as follows:

$$\Delta\mathrm{OD} = \log\left(\frac{\mathrm{I_o}}{\mathrm{I}}\right) \approx -\left(\frac{I - I_o}{I_o}\right)$$

The modified Beer-Lambert Law for [HbO] and [Hb] is

$$\Delta \mathrm{OD}(\lambda) = \mathrm{L}(\lambda)\mathrm{DPF}(\lambda)(\varepsilon_{\mathrm{Hb}}(\lambda)\Delta[\mathrm{Hb}] + \varepsilon_{\mathrm{HbO}}(\lambda)\Delta[\mathrm{HbO}])$$

where $\mathrm{L}(\lambda)$ is the geometrical distance between the light source and detector, $\mathrm{DPF}(\lambda)$ is the differential path length factor to account for the mean distance photons travel through the tissue, and $\Delta[\mathrm{HbO}]$ and $\Delta[\mathrm{Hb}]$ are the concentrations of oxyhemoglobin and deoxyhemoglobin relative to baseline (in units of μM), respectively. The equation is based on the first order Taylor series expansion of the optical density where the scattering term is neglected[24]. Typical values for length L are between 2 and 4 cm. The depth that light may penetrate through the tissue is equal to about half the distance between the source and detector pair. The change in absorption, $\Delta\mu_{\mathrm{a}}$, can be estimated by the measured changes in optical density, the known distance between the source and detectors, and by setting the DPF or computing it from absolute measurements of optical properties.

$$\Delta\mu_{\mathrm{a}}(\lambda) = \frac{\Delta \mathrm{OD}(\lambda)}{\mathrm{L}(\lambda)\mathrm{DPF}(\lambda)}$$

The relationship between changes in absorption may then be related to the changes in concentrations of [HbO] and [Hb] and extinction coefficients with a system of equations developed from the modified Beer-Lambert Law.

$$\begin{bmatrix} \dfrac{\Delta \mathrm{OD}(\lambda_1)}{\mathrm{L}(\lambda_1)\mathrm{DPF}(\lambda_1)} \\ \dfrac{\Delta \mathrm{OD}(\lambda_2)}{\mathrm{L}(\lambda_2)\mathrm{DPF}(\lambda_2)} \end{bmatrix} = \begin{bmatrix} \varepsilon_{\mathrm{HbO}}(\lambda_1) & \varepsilon_{\mathrm{Hb}}(\lambda_1) \\ \varepsilon_{\mathrm{HbO}}(\lambda_2) & \varepsilon_{\mathrm{Hb}}(\lambda_2) \end{bmatrix} \begin{bmatrix} \Delta[\mathrm{HbO}] \\ \Delta[\mathrm{Hb}] \end{bmatrix}$$

From here, $\Delta[\mathrm{HbO}]$ and $\Delta[\mathrm{Hb}]$ are computed. The form of the following system of equations is the same as the form of the equations for [HbO] and [Hb] in the previous section (Equation 1.3 and Equation 1.4). The only change is that here we consider changes instead of absolute values.

$$\begin{bmatrix} \Delta[\mathrm{HbO}] \\ \Delta[\mathrm{Hb}] \end{bmatrix} = \begin{bmatrix} \varepsilon_{\mathrm{HbO}}(\lambda_1) & \varepsilon_{\mathrm{Hb}}(\lambda_1) \\ \varepsilon_{\mathrm{HbO}}(\lambda_2) & \varepsilon_{\mathrm{Hb}}(\lambda_2) \end{bmatrix}^{-1} \begin{bmatrix} \dfrac{\Delta\mathrm{OD}(\lambda_1)}{\mathrm{L}(\lambda_1)\mathrm{DPF}(\lambda_1)} \\ \dfrac{\Delta\mathrm{OD}(\lambda_2)}{\mathrm{L}(\lambda_2)\mathrm{DPF}(\lambda_2)} \end{bmatrix}$$

Then, $\Delta[\mathrm{HbT}]$ is computed as the sum of $\Delta[\mathrm{HbO}]$ and $\Delta[\mathrm{Hb}]$. It is proportional to changes in blood volume.

$$\Delta[\mathrm{HbT}] = \Delta[\mathrm{HbO}] + \Delta[\mathrm{Hb}]$$

Its units are, of course, also μM, which specifically means micromoles of hemoglobin per liter of tissue. To convert $\Delta[\mathrm{HbT}]$ to blood volume units of ml blood per 100 grams of tissue, we simply need to divide by the concentration of hemoglobin in blood as well as by the brain tissue density. The concentration changes of oxyhemoglobin, deoxyhemoglobin, and total hemoglobin are due to changes in blood volume, blood flow, and the metabolic rate of oxygen[25]. This point will be discussed more in Section 1.6 .

1.4.2 Absolute measurements

Frequency domain (FD) near-infrared spectroscopy can measure absolute tissue concentrations of [HbO], [Hb], and total hemoglobin ([HbT]) in units of micromolars [17], [26]. The benefit of absolute measurements is that the values can be compared across subjects or within subjects at different time points.

In FD NIRS, light is modulated at a frequency on the order of 110 MHz. After transmission through tissue, the NIRS system measures the DC amplitude (direct current, meaning average value), the AC (alternating current) amplitude, and the phase of light, Φ, relative to the modulated input light. A diffusion-based, semi-infinite homogenous model can be used to compute absolute optical properties from either DC and phase data or AC and phase data for light collected from multiple source-detector distances, ρ [27], [28]. The slope of $\ln(\rho^2 AC)$ with respect to ρ is notated as S_{AC} where AC stands for the AC amplitude. The slope of phase, Φ, with respect to ρ is notated as S_{Φ}.

$$\mu_a(\lambda) = \frac{\omega}{2v}\left(\frac{S_\Phi(\lambda)}{S_{AC}(\lambda)} - \frac{S_{AC}(\lambda)}{S_\Phi(\lambda)}\right)$$

$$\mu_s'(\lambda) = \frac{S_{AC}^2(\lambda) - S_\Phi^2(\lambda)}{3\mu_a(\lambda)} - \mu_a(\lambda)$$

In the above equations, ω is the angular modulation frequency of the source intensity and *v* is the speed of light in tissue. We may then use Equation 1.3, Equation 1.4, and Equation 1.5 to compute [HbO], [Hb], and [HbT].

1.5 Oscillatory hemodynamics

Recently, there has been interest in spontaneous as well as induced oscillations of [HbO] and [Hb], because their amplitudes and relative phases can be related to physiological quantities such as blood volume, blood flow, oxygen consumption, and cerebral autoregulation. Oscillations of [HbO] and [Hb] occur naturally within the human body at the heart rate (~1 Hz), the respiratory rate (~0.25 Hz), and at the frequency of spontaneous low frequency oscillations (~0.1 Hz). Oscillations can also be induced at specific frequencies with various protocols including paced breathing [29], thigh cuff occlusions [30], and squat-stand maneuvers [31].

The phase difference between [HbO] and [Hb] oscillations is relevant to the study of both the diseased and healthy human brain. For example, in a study of unilateral carotid obstruction, patients were instructed to breathe at 6 breathes per minute in order to induce blood pressure (BP) oscillations at a frequency of 0.1 Hz [32]. The systemic BP oscillations induced oscillations in cerebral [HbO] and [Hb] that were measured with NIRS in each hemisphere. It was found that the phase lag between [HbO] and [Hb] was significantly larger in the hemisphere effected by the carotid obstruction in comparison to the healthy hemisphere. The difference between the hemispheres was attributed to differences in autoregulation, with autoregulation being less efficient during obstruction. As another example, in a sleep study of healthy subjects, NIRS measurements from the brain revealed altered phase differences between [HbO] and [Hb] low-frequency (~0.1 Hz) spontaneous oscillations when comparing non-REM to REM sleep states [33], a finding that was interpreted in terms of oscillations in blood flow velocity and blood volume.

1.6 Coherent hemodynamics spectroscopy

In 2013, the technique called coherent hemodynamics spectroscopy (CHS) was introduced and leveraged the physiologic information contained in the relative phase and amplitude relationship between oscillations of [HbO] and [Hb][34]. CHS has a frequency-domain approach and a time-domain approach. In both techniques, a blood pressure stimulus induces cerebral blood volume and blood flow changes whose effects we may observe by measuring [HbO] and [Hb]. The frequency-domain approach utilizes oscillations in arterial blood pressure (ABP) to induce coherent oscillations in [HbO] and [Hb]. The ABP oscillations may be induced with techniques such as paced breathing or cyclic thigh cuff occlusions or they may be spontaneously occurring. The coherent oscillations of [HbO] and [Hb] may be written as phasors. We assume negligible contribution from changes in the metabolic rate of oxygen in the following forms of the equations. We describe the meaning of each term in Table 1 and also list the parameters which are fit for in the equations.

$$\begin{aligned}\mathbf{O}(\omega) = \text{ctHb}\Big[&S^{(a)}\text{CBV}_0^{(a)}\mathbf{cbv}^{(a)}(\omega) + S^{(v)}\text{CBV}_0^{(v)}\mathbf{cbv}^{(v)}(\omega)\Big] + \\ &+\text{ctHb}\left[\frac{\langle S^{(c)}\rangle}{S^{(v)}}\left(\langle S^{(c)}\rangle - S^{(v)}\right)\text{F}^{(c)}\text{CBV}_0^{(c)}\mathcal{H}_{RC-LP}^{(c)}(\omega)\right. \\ &\qquad\qquad \left. + \left(S^{(a)} - S^{(v)}\right)\text{CBV}_0^{(v)}\mathcal{H}_{G-LP}^{(v)}(\omega)\right]\mathbf{cbf}(\omega)\end{aligned} \tag{1.6}$$

$$\begin{aligned}\mathbf{D}(\omega) = \text{ctHb}\Big[&\left(1 - S^{(a)}\right)\text{CBV}_0^{(a)}\mathbf{cbv}^{(a)}(\omega) + \left(1 - S^{(v)}\right)\text{CBV}_0^{(v)}\mathbf{cbv}^{(v)}(\omega)\Big] + \\ &-\text{ctHb}\left[\frac{\langle S^{(c)}\rangle}{S^{(v)}}\left(\langle S^{(c)}\rangle - S^{(v)}\right)\text{F}^{(c)}\text{CBV}_0^{(c)}\mathcal{H}_{RC-LP}^{(c)}(\omega)\right. \\ &\qquad\qquad \left. + \left(S^{(a)} - S^{(v)}\right)\text{CBV}_0^{(v)}\mathcal{H}_{G-LP}^{(v)}(\omega)\right]\mathbf{cbf}(\omega)\end{aligned} \tag{1.7}$$

Table 1. Explanation of terms and parameters in hemodynamic model

Variable	Meaning	Type
$\mathbf{O}(\omega)$	phasor for oscillations of [HbO]	expression
$\mathbf{D}(\omega)$	phasor for oscillations of [Hb]	expression
ctHb	concentration of hemoglobin in blood	constant (set to 2300 μM in healthy person)
$S^{(a)}$	oxygen saturation of hemoglobin in the arterial compartment	constant (set to 0.98 in healthy person)
$S^{(v)}$	oxygen saturation of hemoglobin in the venous compartment	constant computed from model parameters

$\langle S^{(c)} \rangle$	spatial average of oxygen saturation of hemoglobin in the capillary compartment	constant computed from model parameters
$\mathrm{CBV}_0^{(a)}$	cerebral blood volume in the arterial compartment	constant (set to 0.35 in healthy person)
$\mathrm{CBV}_0^{(v)}$	cerebral blood volume in the venous compartment	constant computed from model parameters, baseline absolute [HbT], and ctHb
$\mathrm{CBV}_0^{(c)}$	cerebral blood volume in the capillary compartment	constant computed from model parameters, baseline absolute [HbT], and ctHb
$\mathbf{cbv}^{(a)}(\omega)$	phasor for oscillations of blood volume in the arterial compartment	expression
$\mathbf{cbv}^{(v)}(\omega)$	phasor for oscillations of blood volume in the venous compartment	expression
$\mathrm{F}^{(c)}$	Fåhraeus factor which accounts for reduced hematocrit in the capillaries	constant (set to 0.8)
$\mathcal{H}_{RC-LP}^{(c)}(\omega)$	RC low pass filter in the capillary compartment	computed from model parameters
$\mathcal{H}_{G-LP}^{(v)}(\omega)$	Gaussian low pass filter in the venous compartment	computed from model parameters
$\mathbf{cbf}(\omega)$	phasor for oscillations of blood flow	expression
$t^{(c)}$	transit time of blood in the capillaries	parameter
$t^{(v)}$	transit time of blood in the veins	parameter
f_c	autoregulation efficiency	parameter
k	inverse of the Grubb's exponent	parameter
$\frac{\mathrm{F}^{(c)}\mathrm{CBV}_0^{(c)}}{\mathrm{CBV}_0}$	Contribution of capillaries to blood volume	parameter

The RC low pass filter $\mathcal{H}_{RC-LP}^{(c)}(\omega)$ contains the parameter $t^{(c)}$which describes the transit time of blood in the capillaries. The Gaussian low pass filter $\mathcal{H}_{G-LP}^{(v)}(\omega)$ contains the parameter $t^{(c)}$ in addition to the parameter $t^{(v)}$ which describes the transit time of blood in the veins. The phasor of cerebral blood flow can be modeled as cerebral blood volume passing through a high pass filter $H_{HP}^{(AR)}(\omega)$ and scaled by a factor k to account for the relative amplitude of blood flow changes to blood volume changes:

$$\mathbf{cbf}(\omega) = kH_{HP}^{(AR)}(\omega)\mathbf{cbv}(\omega). \tag{1.8}$$

$H_{HP}^{(AR)}(\omega)$ is an RC high pass filter that has a cut-off frequency of f_c. This high pass filter is intended to model the effects of cerebral autoregulation. The parameter f_c indicates the frequency at which autoregulation is no longer able to dampen blood flow changes induced by ABP. Therefore, a higher cut-off frequency indicates a more efficient autoregulation, because a wider range of frequencies can be attenuated with the autoregulation filter. We note that cerebral blood volume on the right hand side of Equation 1.8 is a surrogate for changes in MAP. In Chapter 3 we characterize the actual relationship between cerebral blood volume and MAP. In Chapter 4 we apply the findings of Chapter 3 to modify this aspect of the hemodynamic model.

The relationship between [HbO] and [Hb] are described by their relative phases and amplitude at each frequency of interest. Multiple frequencies of [HbO] and [Hb] form the CHS spectra that are fit to CHS equations in the frequency-domain. This frequency domain approach will be describes in more detail in Chapter 2. The time-domain approach utilizes a step-like change in ABP (such as described in Section 1.3.3.2) to induce a coherent change in [HbO] and [Hb]. To induce the ABP change, two thigh cuffs are inflated above arterial pressure for two minutes and then rapidly released. The release causes a sharp drop in mean arterial pressure (MAP) by about 20% which recovers within 15-20 seconds. The corresponding changes in [HbO] and [Hb] are fit to the CHS equations in the time-domain

[35]. In both the frequency-domain and time-domain techniques, the parameters resulting from the fit can be used to compute absolute cerebral blood flow, notated as CBF_0 :

$$\mathrm{CBF}_0 = \frac{1}{\rho}\frac{\mathrm{F}^{(c)}\mathrm{CBV}_0^{(c)}}{t^{(c)}} = \frac{1}{\rho}\frac{T_0}{\mathrm{ctHb}}\frac{\frac{\mathrm{F}^{(c)}\mathrm{CBV}_0^{(c)}}{\mathrm{CBV}_0}}{t^{(c)}} \tag{1.9}$$

where CBV_0 is total blood volume, T_0 is baseline [HbT], and ρ is the density of brain tissue. The first realization of the above equation is written in terms of the central volume principle where CBF is the ratio between blood volume to blood transit time. In the second realization of the equation, CBF is written in terms of two of the parameters that are fit for in the hemodynamic model: $\frac{\mathrm{F}^{(c)}\mathrm{CBV}_0^{(c)}}{\mathrm{CBV}_0}$ and $t^{(c)}$. The parameter $\frac{\mathrm{F}^{(c)}\mathrm{CBV}_0^{(c)}}{\mathrm{CBV}_0}$ describes the blood volume contribution of the capillary compartment (as opposed to the arterial or venous compartments). The two ways of writing the equation for CBF are related with the equation T_0=ctHbCBV$_0$.

The first clinical application of CHS was in the hemodialysis unit where it was found that absolute CBF was lower in patients undergoing dialysis than in a healthy control group [36], [37]. The ability of CHS to measure autoregulation efficiency has been validated in an experiment with healthy subjects [35]. Autoregulation was measured during normal breathing and during hyperventilation. It is well established that hyperventilation induces hypocapnia and increases the efficiency of autoregulation in cerebral tissue. An increase in the autoregulation parameter, f_c , was found in 10 out of 11 subjects, supporting that CHS is sensitive to changes in autoregulation efficiency.

1.7 Time-frequency resolution

Coherent hemodynamics spectroscopy requires measures of concentrations of oxyhemoglobin, deoxyhemoglobin, and mean arterial pressure over several frequencies. It is critical to understand the trade-off between time resolution and frequency resolution when designing experiments and performing data analysis. If the sample rate is F_s and the number of samples in the observation time is n, the frequency resolution is:

$$\Delta f = \frac{F_s}{n}. \tag{1.10}$$

From Equation 1.10, we can see then, that there is an inverse relationship between frequency resolution and time resolution. Typically, segments of data in the time domain are multiplied with a window function, such as the Hamming window, to reduce spectral leakage. The use of a window function will make the frequency resolution larger than the resolution specified in Equation 1.10.

Three common non-parametric approaches for transfer function analysis are based on the Hilbert transform, wavelet transform, or short-time Fourier transform. It is important to note that while each of these approaches is implemented differently, they provide equivalent results as long as the parameters used are equivalent [38]. There is sometimes a misconception that Hilbert or wavelet transforms provide continuous time resolution (equivalent to the data's sample spacing $1/F_s$) as well as improve frequency resolution compared to the short-time Fourier transform. This is not true. The time-frequency resolution depends solely on the window size , n, and the window function.

Chapter 2: Characterization of hemodynamic oscillations in healthy tissue

2.1 Introduction

The amplitude and phase of deoxy-hemoglobin concentration ([Hb]), oxy-hemoglobin concentration ([HbO]), and total hemoglobin concentration ([HbT]) oscillations at angular frequency ω can be described with phasor notation: **[Hb]**(ω), **[HbO]**(ω), and **[HbT]**(ω). CHS spectra are given by the frequency dependence of the magnitude and phase of the phasor ratios **[Hb]** (ω)/**[HbO]** (ω) and **[HbO]** (ω)/**[HbT]** (ω). In phasor algebra, this corresponds to the following amplitude ratios and phase differences as a function of frequency: |**[Hb]**|/|**[HbO]**|, |**[HbO]**|/|**[HbT]**|, Arg(**[Hb]**)-Arg(**[HbO]**), and Arg(**[HbO]**)-Arg(**[HbT]**), where “Arg” is the argument of the phasor, i.e. its phase angle with respect to the *x* axis. By means of a hemodynamic model [34], the measured CHS spectra can be related to fundamental physiological parameters like the capillary and venous blood transit times and the cutoff frequency of the cerebral autoregulation process.

CHS can be applied to any tissue, not just the brain. In this study, we have chosen to also study breast tissue, because CHS may yield valuable information for cancer assessment, as a result of the hemodynamic and metabolic perturbations associated with breast cancer. The utility of assessing hemodynamic changes with NIRS in breast tissue has been investigated in the literature. In a study looking at breast hemodynamics, a dual-breast near-infrared tomographic system measured different responses to a Valsalva maneuver in a comparison between the healthy and tumor-bearing breasts on the same subject [39]. The return to baseline of deoxyhemoglobin concentration in the tumor-bearing breast lagged behind the return to baseline in the healthy breast. Carp *et al* have studied the breast hemodynamic response to compression in order to investigate physiological differences of healthy and diseased tissue [40]. Breast hemodynamics during periodic oscillations have also been studied with a protocol in which subjects used a respiratory device to alternate between breathing oxygen and carbogen [41]. Total hemoglobin concentration response was measured with NIRS, and reported results support that the total hemoglobin responses of cancerous breasts were less correlated to the changes in inspired oxygen concentrations than the total hemoglobin responses of healthy breasts. Flexman *et al* have studied the response of breast tissue to a breath holding protocol and found differences between malignant and healthy tissue during breath holding and recovery [42]. The spatial and temporal study of breast hemodynamics may result in a powerful tool for the characterization and detection of abnormalities in the tissue vasculature and metabolism. CHS may therefore be a useful addition to this area of study.

Oscillations in blood volume and blood flow have individual effects on the oscillations of [Hb] and [HbO] that are measured with NIRS. Blood volume oscillations, by themselves, result in synchronous (or in phase) oscillations of [Hb] and [HbO]. Blood flow oscillations, by themselves, result in oscillations of [Hb] and [HbO] that are in opposition of phase (π phase difference). Such individual volume and flow effects are, in general, out of phase with each other even in the case in which the blood volume and blood flow oscillations are synchronous. This result follows from the delayed [Hb] and [HbO] responses to blood flow changes (this delay is caused by the finite blood transit time in the microvasculature), which we modeled by treating the microvasculature as a low-pass filter for the driving blood flow dynamics (input) and the resulting [Hb] and [HbO] dynamics (output) [34]. According to this analysis, the phase difference between the overall, measured, [Hb] and [HbO] oscillations reflects the relative contributions on them from blood volume and blood flow changes. In-phase [Hb] and [HbO] oscillations suggest volume dominated effects, opposition-of-phase [Hb] and [HbO] oscillations suggest flow dominated effects. The relative contributions to [Hb] and [HbO] oscillations from oscillations in blood volume and blood flow (and, when applicable, oxygen consumption) may depend on the frequency of oscillations, and this fact is exploited by CHS for a quantitative study of tissue hemodynamics and oxidative metabolism [34].

Even though blood volume and blood flow changes may be interconnected (for example a change in blood volume in a compartment may reflect an imbalance between flow in and flow out of that compartment), we note that NIRS is not sensitive to blood flow dynamics occurring outside the capillary compartment. One of the assumptions of our model is that blood volume changes occur synchronously in the three compartments (arterial, capillary, venous), and for this reason we use the general term “blood volume change” without any further clarification. On the contrary, blood flow changes in the context of this work refer only to capillary flow changes.

In this study, we have used NIRS to concurrently measure blood-pressure-induced hemoglobin oscillations in the breast and the brain (prefrontal cortex) of healthy volunteers. The measured CHS spectra in the breast and the brain show that [Hb] and [HbO] oscillations are in phase (i.e. synchronous) in the healthy breast and out of phase (i.e. asynchronous) in the healthy brain. We attribute these results to different relative contributions of blood volume and blood flow to the measured oscillations of [Hb] and

[HbO] in the two tissues examined. While we have focused on breast and brain tissue, a similar hemodynamic study in other tissues can yield similar information about the contribution of blood volume and blood flow to hemoglobin concentration oscillations measured with NIRS.

2.2 Methods

2.2.1 Human subjects and data acquisition

Eleven healthy female subjects (age range: 24-32 years old) participated in the study. All subjects were premenopausal, had no history of vascular disorders, and no known risks for breast cancer. The Tufts University Institutional Review Board approved the experimental protocol, and the subjects provided written informed consent prior to the experiment. Figure 2.1 shows the experimental setup. The near-infrared spectroscopy (NIRS) measurements were performed with a frequency-domain commercial NIRS instrument (OxiplexTS, ISS Inc., Champaign, IL). Optical probes connected to the spectrometer delivered light at two wavelengths, 690 and 830 nm, at a source-detector distance of 35 mm. The brain probe was placed against the left side of the subject's forehead, to access tissue in the prefrontal cortex, and secured with a flexible headband. The breast probe was placed ~20 mm above the areola of the left breast and secured with an adhesive medical tape. Continuous arterial blood pressure (ABP) was recorded with a beat-to-beat blood pressure monitoring system (NIBP100D, BIOPAC Systems, Inc., Goleta, CA). Pneumatic thigh cuffs were wrapped around both subject's thighs and connected to an automated cuff inflation system (E-20 Rapid Cuff Inflation System, D.E. Hokanson, Inc., Bellevue, WA). The air pressure in the thigh cuffs was continuously monitored with a digital manometer (Series 626 Pressure Transmitter, Dwyer

Instruments, Inc., Michigan City, IN). Analog outputs of the arterial blood pressure monitor and the thigh cuff pressure monitor were fed to auxiliary inputs of the NIRS instrument for concurrent recordings with the NIRS data.

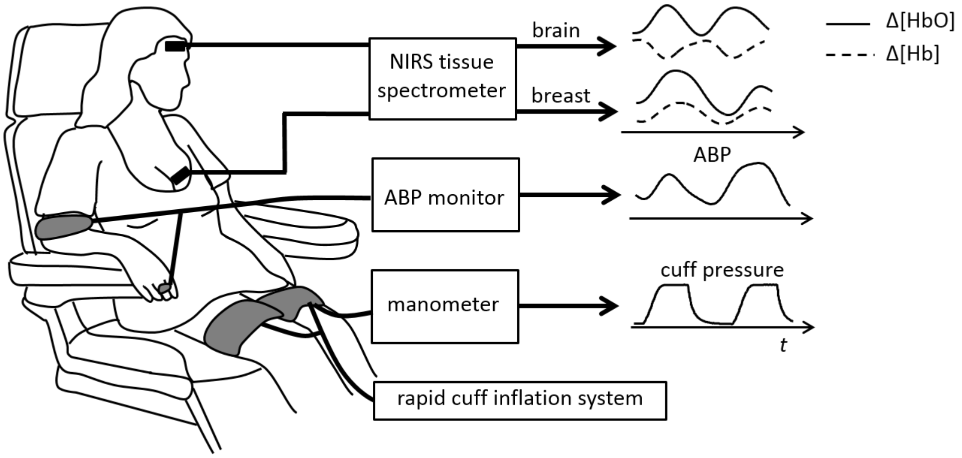

Figure 2.1. Experimental setup. Signals from the near-infrared spectroscopy (NIRS) instrument, arterial blood pressure (ABP) monitor, and thigh cuff manometer were recorded synchronously. Optical data from the spectrometer were used to compute the changes in [HbO] and [Hb] (Δ[HbO] and Δ[Hb]) over time (t).

Baseline measurements, during which the subjects were resting and the thigh cuffs were deflated, were recorded for two minutes for each participant. Then, the thigh cuffs were periodically inflated (to a pressure of ~200 mmHg) and deflated for six periods at five different frequencies, f_i ($f_i = \omega_i/2\pi$): 0.046, 0.056, 0.063, 0.071, and 0.083 Hz. The cyclic inflations of the thigh cuffs induced periodic changes in the arterial blood pressure [30]. The associated changes in [HbO] and [Hb] in the brain and breast were measured with NIRS. Each set of cyclic cuff inflations was followed by 20 s of rest during which baseline conditions were re-established. All signals were sampled synchronously at an acquisition rate of 12.5 Hz.

2.2.2 Data analysis

Data analysis and processing were performed with Matlab (Mathworks Inc., Natick, MA). Optical intensity changes from the brain and the breast were translated to changes in the concentrations of oxy-hemoglobin [ΔHbO(t)], deoxy-hemoglobin [ΔHb(t)], and total hemoglobin [ΔHbT] by using the modified Beer-Lambert law (defined in Section 1.4.1). The signals were analyzed with the following process for each of the five frequencies of thigh cuff oscillations, f_i (i=1,…,5). The time traces were filtered with a linear phase, finite impulse response (FIR), band pass filter based on the Parks-McClellan algorithm [43]. The filter had a width of 0.01 Hz that was centered at f_i. The Hilbert transform was applied to the band pass filtered signals in order to obtain the instantaneous amplitude and phase at that frequency [44]. Experiments on tissue-like phantoms with static optical properties were used to determine the noise floor of the intensity measurements, which were translated into the detection threshold for oscillations in hemoglobin concentrations in tissue. From these phantom experiments, a threshold of 0.015 μM was considered as the noise level for the amplitude of oscillations and applied to the instantaneous amplitudes of deoxy- and oxy-hemoglobin to remove data points with lower amplitudes [36]. The thigh cuff manometer signal was then used to determine the time ranges at which the six periods of induced oscillations of frequency f_i occurred. The magnitudes and phases of $\mathbf{[Hb]}(\omega_i)/\,\mathbf{[HbO]}(\omega_i)$ and $\mathbf{[HbO]}(\omega_i)/\,\mathbf{[HbT]}(\omega_i)$ were computed and averaged within the time ranges of the measurements at each f_i to obtain CHS spectra (namely, |**[Hb]**|/|**[HbO]**|, |**[HbO]**|/|**[HbT]**|**,** Arg(**[Hb]**)-Arg(**[HbO]**), and Arg(**[HbO]**)-Arg(**[HbT]**)).

In the case of brain measurements, the CHS spectra showed typical features previously reported by our group[45] and allowed for the assessment of six hemodynamic parameters by fitting the CHS spectra with a hemodynamic model[34]. The model describes how **[HbO]**, **[Hb]**, and **[HbT]** are related to microcirculation blood volume, blood flow, and metabolic rate of oxygen. The spectra are described by the ratio of Equation 1.7 to Equation 1.6 We plug in Equation 1.8 to model the cerebral blood flow phasor.

$$\frac{[\mathbf{Hb}](\omega)}{[\mathbf{HbO}](\omega)} = \frac{\left(1-S^{(a)}\right)\frac{\mathrm{CBV}_0^{(a)}\mathbf{cbv}^{(a)}(\omega)}{\mathrm{CBV}_0^{(v)}\mathbf{cbv}^{(v)}(\omega)} + \left(1-S^{(v)}\right) - \left[\frac{\langle S^{(c)}\rangle}{S^{(v)}}\left(\langle S^{(c)}\rangle - S^{(v)}\right)\frac{\mathrm{F}^{(c)}\mathrm{CBV}_0^{(c)}}{\mathrm{CBV}_0^{(v)}}\mathcal{H}_{\text{RC-LP}}^{(c)}(\omega) + \left(S^{(a)}-S^{(v)}\right)\mathcal{H}_{\text{G-LP}}^{(v)}(\omega)\right] k\frac{\mathrm{CBV}_0^{(v)}}{\mathrm{CBV}_0}\mathcal{H}_{RC-HP}^{(\mathrm{AR})}(\omega)\left[\frac{\mathrm{CBV}_0^{(a)}\mathbf{cbv}^{(a)}(\omega)}{\mathrm{CBV}_0^{(v)}\mathbf{cbv}^{(v)}(\omega)} + 1\right]}{S^{(a)}\frac{\mathrm{CBV}_0^{(a)}\mathbf{cbv}^{(a)}(\omega)}{\mathrm{CBV}_0^{(v)}\mathbf{cbv}^{(v)}(\omega)} + S^{(v)} + \left[\frac{\langle S^{(c)}\rangle}{S^{(v)}}\left(\langle S^{(c)}\rangle - S^{(v)}\right)\frac{\mathrm{F}^{(c)}\mathrm{CBV}_0^{(c)}}{\mathrm{CBV}_0^{(v)}}\mathcal{H}_{\text{RC-LP}}^{(c)}(\omega) + \left(S^{(a)}-S^{(v)}\right)\mathcal{H}_{\text{G-LP}}^{(v)}(\omega)\right] k\frac{\mathrm{CBV}_0^{(v)}}{\mathrm{CBV}_0}\mathcal{H}_{RC-HP}^{(\mathrm{AR})}(\omega)\left[\frac{\mathrm{CBV}_0^{(a)}\mathbf{cbv}^{(a)}(\omega)}{\mathrm{CBV}_0^{(v)}\mathbf{cbv}^{(v)}(\omega)} + 1\right]} \tag{2.1}$$

$$\frac{[\mathbf{HbO}](\omega)}{[\mathbf{HbT}](\omega)} = \frac{S^{(a)}\frac{CBV_0^{(a)}\mathbf{cbv}^{(a)}(\omega)}{CBV_0^{(v)}\mathbf{cbv}^{(v)}(\omega)} + S^{(v)} + \left[\frac{\langle S^{(c)}\rangle}{S^{(v)}}\left(\langle S^{(c)}\rangle - S^{(v)}\right)\frac{\mathrm{F}^{(c)}CBV_0^{(c)}}{CBV_0^{(v)}}\mathcal{H}_{RC\text{-}LP}^{(c)}(\omega) + \left(S^{(a)}-S^{(v)}\right)\mathcal{H}_{G\text{-}LP}^{(v)}(\omega)\right] k\frac{CBV_0^{(v)}}{CBV_0}\mathcal{H}_{RC-HP}^{(AR)}(\omega)\left[\frac{CBV_0^{(a)}\mathbf{cbv}^{(a)}(\omega)}{CBV_0^{(v)}\mathbf{cbv}^{(v)}(\omega)} + 1\right]}{\frac{CBV_0^{(a)}\mathbf{cbv}^{(a)}(\omega)}{CBV_0^{(v)}\mathbf{cbv}^{(v)}(\omega)} + 1} \tag{2.2}$$

We used a nonlinear fitting procedure in Matlab (function “lsqcurvefit”) with a trust region reflective algorithm to fit our measurements with the model. The six hemodynamic parameters fitted for in our analysis are the capillary blood transit time $\left(t^{(c)}\right)$, the venous blood transit time $\left(t^{(v)}\right)$, the ratio of capillary-to-venous baseline blood volumes corrected for the small-to-large vessel hematocrit ratio $\left(\frac{\mathrm{F}^{(c)}\mathrm{CBV}_0^{(c)}}{\mathrm{CBV}_0^{(v)}}\right)$, the ratio of amplitudes of arterial-to-venous blood volume oscillations $\left(\frac{\Delta\mathrm{CBV}^{(a)}}{\Delta\mathrm{CBV}^{(v)}}\right)$, the autoregulation cutoff frequency $\left(f_c^{(\mathrm{AR})}\right)$, and the product of the inverse of the Grubb's exponent (k) times the ratio of venous-to-total baseline blood volumes $\left(\frac{k\mathrm{CBV}_0^{(v)}}{\mathrm{CBV}_0}\right)$. The search regions for the fitting parameters are defined by ranges found in the literature [46]. The analytical expressions, derived from the hemodynamic model, and the simplifying assumptions relating these six hemodynamic parameters and the CHS spectra are described in detail in Kainerstorfer *et al* [47].

In the case of breast measurements, because the phasors **[Hb]** (ω_i), **[HbO]** (ω_i), and **[HbT]** (ω_i) were found to be in phase with each other at all measured frequencies, the amplitude ratio |**[HbO]** (ω_i)|/| **[HbT]** (ω_i)| provides a measure of the oxygen saturation of hemoglobin in the volume-oscillating vascular compartments [34], which we indicate here with S_V. This measure of hemoglobin saturation is a weighted average of the saturations of the volume oscillating compartments, where each vascular compartment is weighted according to its relative contributions to the overall blood volume oscillations:

$$S_\mathrm{V} = \frac{\mathrm{CBV}_0^{(a)}|\mathbf{cbv}^{(a)}(\omega)|S^{(a)}+\mathrm{F}^{(c)}\mathrm{CBV}_0^{(c)}|\mathbf{cbv}^{(c)}(\omega)|\langle S^{(c)}\rangle+\mathrm{CBV}_0^{(v)}|\mathbf{cbv}^{(v)}(\omega)|S^{(v)}}{\mathrm{CBV}_0|\mathbf{cbv}(\omega)|} \quad (2.3)$$

2.3 Results

Figure 2.2 shows band-pass filtered time traces of changes in ABP, HbO, and Hb, in the brain and breast of Subject No. 8. By inspection of Figure 2.2, one can clearly see the oscillations in systemic arterial blood pressure and local concentrations of oxy- and deoxy-hemoglobin that are elicited by the cyclic thigh cuff occlusions (identified by the vertical grey bars in Figure 2.2).

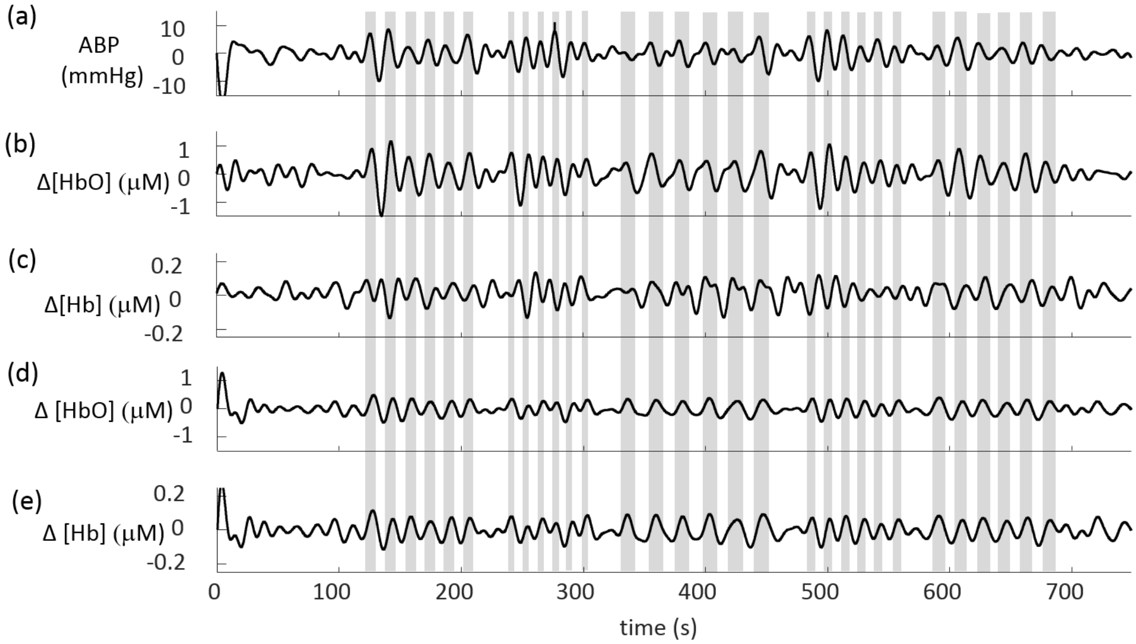

Figure 2.2. Time traces for Subject No. 8. The shaded regions indicate the times at which the cuffs were inflated to a pressure of 200 mmHg. The cuffs were timed such that each frequency has 6 periods for analysis. The order of frequencies in the figure is: 0.063, 0.083, 0.046, 0.071, 0.056 Hz. (a) Changes in mean arterial blood pressure; (b) Changes in oxy-hemoglobin concentration measured in brain tissue; (c) Changes in deoxy-hemoglobin concentration measured in brain tissue; (d) Changes in oxy-hemoglobin concentration measured in breast tissue; (e) Changes in deoxy-hemoglobin concentration measured in breast tissue. All the temporal traces shown in this figure were band-pass filtered (0.01-0.11 Hz, width: 0.1 Hz), whereas data analysis at each frequency was performed by applying a narrower band-pass filter (width: 0.01 Hz) centered at the frequency of interest.

The group averages of CHS spectra were computed for the eleven subjects. A variance threshold was used to select the induced frequencies in each subject that successfully maintained a consistent phase difference: The standard deviation of Arg(**[Hb]**)-Arg(**[HbO]**) and the standard deviation of Arg(**[HbO]**)-Arg(**[HbT]**) both needed to be less than 45 degrees. The number of subjects for whom the measured data passed the threshold was as follows for brain data at each frequency: 0.046 Hz, *n*=10; 0.056 Hz, *n*=11; 0.063 Hz, *n*=10; 0.071 Hz, *n*=10; 0.083 Hz, *n*=11. For breast data, the corresponding numbers of subjects were as follows: 0.046 Hz, *n*= 11; 0.056 Hz, *n*=11; 0.063 Hz, *n*=11; 0.071 Hz, *n*=11; 0.083 Hz, *n*=10. On almost all of the subjects and all of the frequencies, we could measure reliable and coherent hemodynamics on both brain and breast tissue. For the cases that passed the threshold requirement, the mean phase differences and amplitudes ratios (representing the CHS spectra) were computed and are shown in Figure 2.3. To compute the mean values and standard deviations of Arg(**[Hb]**)-Arg(**[HbO]**) and Arg(**[HbO]**)-Arg(**[HbT]**), we used standard methods in circular statistics [48]. For |**[Hb]**|/|**[HbO]**| and |**[HbO]**|/|**[HbT]**|, we computed the group means, and the errors bars in Figure 2.3 represent the standard error of the mean.

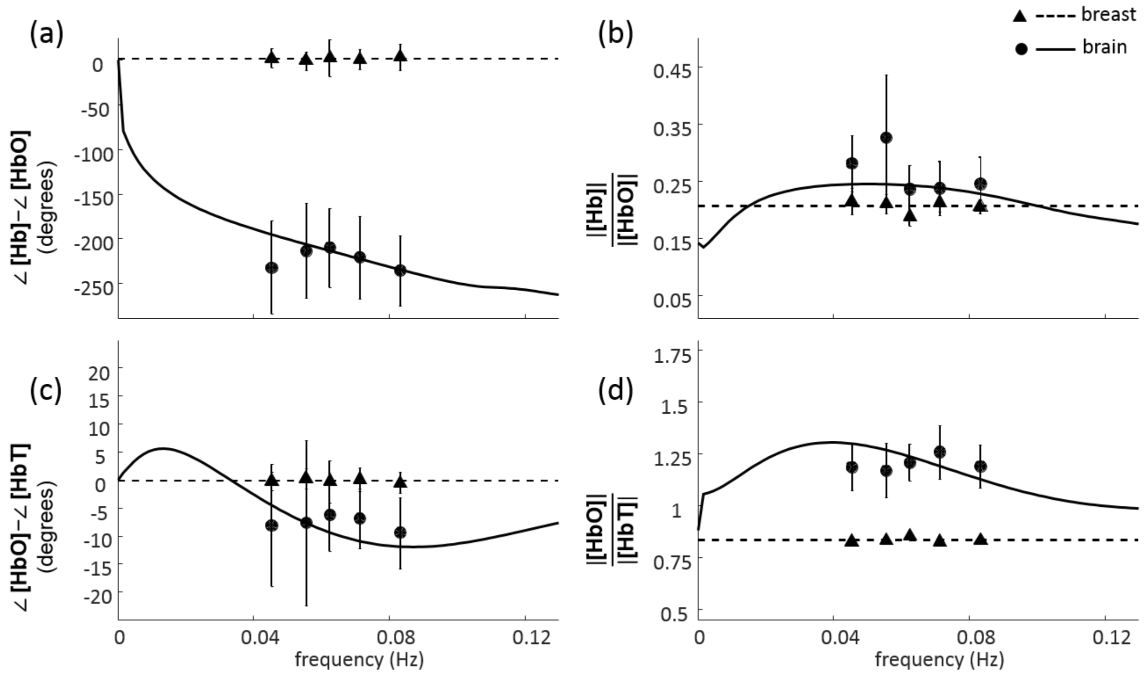

Figure 2.3. Group averaged CHS spectra. Measured on the brain (circles) and breast (triangles) of eleven human subjects at five frequencies of induced hemodynamic oscillations. The lines through the brain spectra (solid lines) are the best fits of the data with the hemodynamic model. The horizontal lines through the breast spectra (dashed lines) are at the average values over the five frequencies. (a) Phase difference Arg(**[Hb]**)-Arg(**[HbO]**); (b) Amplitude ratio |**[Hb]**|/|**[HbO]**|; (c) Phase difference Arg(**[HbO]**)-Arg(**[HbT]**); (d) Amplitude ratio |**[HbO]**|/|**[HbT]**|.

For the brain spectra, the best fits with the hemodynamic model are also plotted (solid lines in Figure 2.3). The brain CHS spectra show quantitative features similar to those found in previous measurements in healthy subjects [45] . Over the frequency range measured here (0.046-0.083 Hz), the phase spectrum for Arg(**[Hb]**)-Arg(**[HbO]**) shows a negative slope of ~0.8°/mHz, whereas the amplitude spectra have values of ~0.25 for |**[Hb]**|/|**[HbO]**| and ~1.2 for |**[HbO]**|/|**[HbT]**| (we observe that |**[HbO]**|/|**[HbT]**| is a phasor amplitude ratio, so that its value greater than 1 is not incompatible with the phasor relationship **[HbT]** = **[HbO]** + **[Hb]**). The oscillations of [Hb] lag the oscillations of [HbO] by 210-235°, whereas the oscillations of [HbO] lag the oscillations of [HbT] by 5-10°.

The CHS spectra measured in the breast did not show a frequency dependence for any of the subjects, and a horizontal straight line at the value of the mean for each spectrum is shown in Figure 2.3 (dashed lines). The mean of Arg(**[Hb]**)-Arg(**[HbO]**) is $2^o \pm 14^o$ and the mean of Arg(**[HbO]**)-Arg(**[HbT]**) is $0^o \pm 2^o$, both of which indicate a non-significant difference from zero, so that the oscillations of [HbO], [Hb], and [HbT] in the breast can be described to be in phase. The mean value of |**[Hb]**|/|**[HbO]**| is 0.21 ± 0.01, whereas the mean value of |**[HbO]**|/|**[HbT]**| is 0.83 ± 0.01 (in this case of in-phase **[Hb]**, **[HbO]**, and **[HbT]** phasors, the ratio |**[HbO]**|/|**[HbT]**| must be ≤ 1).

The phase difference between the oscillations of deoxy-hemoglobin and oxy-hemoglobin concentrations [Arg(**[Hb]**)-Arg(**[HbO]**)] was the feature of greatest interest for this study, because it provides dynamic information about the relative contributions of volume and flow changes in the probed tissue. As an illustrative example of the phase difference of [Hb] and [HbO] oscillations, Figure 2.4(a) shows the times traces of [Hb] and [HbO] changes (Δ[Hb] and Δ[HbO]), and Figure 2.4b) shows the corresponding phasor diagrams of **[Hb]** and **[HbO]**. Figure 2.4 refers to subject No. 1 and a frequency of cyclic cuff inflation of 0.056 Hz (the time periods of cuff inflation are shaded in Figure 2.4(a)). The time traces in Figure 2.4(a) show the out-of-phase behavior of deoxy- and oxy- hemoglobin oscillations in brain tissue (top panels of Figure 2.4) and the in-phase behavior of the oscillations in breast tissue (bottom panels of Figure 2.4). In this example, Arg(**[Hb]**)-Arg(**[HbO]**) is -185°±2° in the brain and 4°±1° in the breast. In Figure 2.4b, **[HbO]** is the phase reference (set at 0°) and the phasor amplitudes are drawn to scale with respect to each other.

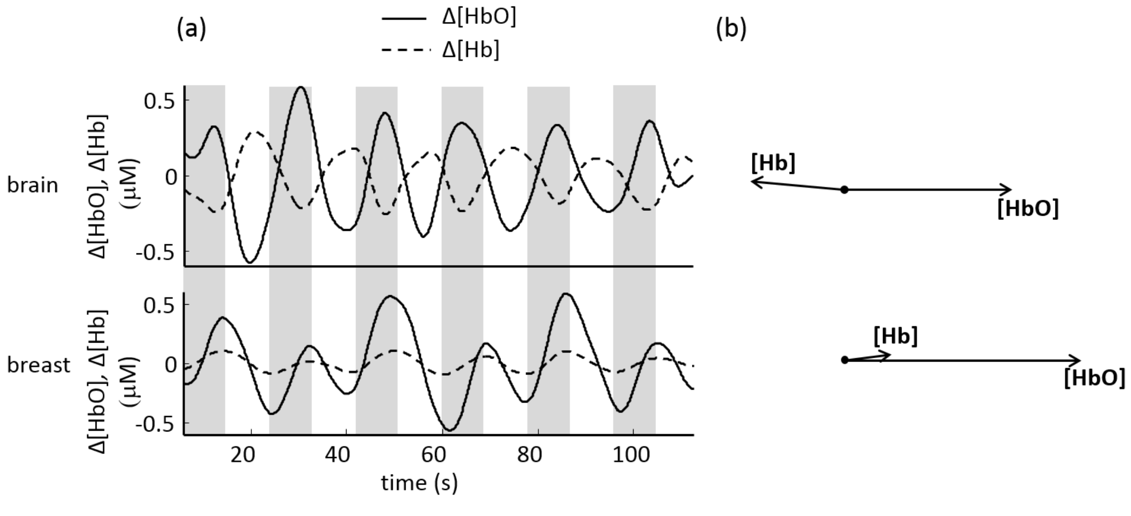

Figure 2.4. Time traces of changes in oxy- and deoxy-hemoglobin concentrations (Δ[HbO] and Δ[Hb], respectively) measured during the cyclic cuff occlusion protocol at 0.056 Hz for subject No. 1. The periods of time when the thigh cuffs were inflated are shaded. The top panel illustrates the out-of-phase behavior of [HbO] and [Hb] oscillations in the healthy brain. The bottom panel reports breast data and illustrates the in-phase behavior of [HbO] and [Hb] oscillations in the healthy breast. (b) Phasor diagrams corresponding to the oscillations reported in panel (a). The phasor diagram in the top panel shows the out-of-phase **[HbO]** and **[Hb]** phasors in the healthy brain, whereas the one in the bottom panel shows the approximately in-phase **[HbO]** and **[Hb]** phasors in the healthy breast

The fits to the brain CHS spectra with the hemodynamic model (solid lines in Figure 2.3) yielded the set of six hemodynamic parameters defined in Section 2.2.2 . The mean values of these parameters (± the standard error of the mean) over the eleven subjects were as follows: $t^{(c)}$= 0.9 ± 0.2 s, $t^{(v)}$ = 5.4 ± 1.1 s, $\frac{\mathrm{F}^{(c)}\mathrm{CBV}_0^{(c)}}{\mathrm{CBV}_0^{(v)}}$ = 1.3± 0.3, $\frac{\Delta\mathrm{CBV}^{(a)}}{\Delta\mathrm{CBV}^{(v)}}$ = 5.2 ± 1.7, $f_c^{(\mathrm{AR})}$ = 0.03 ± 0.02 Hz, $\frac{k\mathrm{CBV}_0^{(v)}}{\mathrm{CBV}_0}$ = 0.8 ± 0.2. Most parameters are in good agreement with values previously reported for the prefrontal cortex of eleven healthy human subjects during a paced breathing protocol [47]. Specifically, the previously reported values of the six parameters were 0.9 ± 0.2 s, 1.3 ± 0.3 s, 1.1 ± 0.3, 2.9 ± 0.9, 0.035 ± 0.002 Hz, and 0.6 ± 0.1, respectively [47]. While some of the parameters deviate from our previous results, the reproducibility of $t^{(c)}$ and $f_c^{(\mathrm{AR})}$confirms the robustness of quantitative CHS measurements of cerebral blood flow (which is inversely related to $t^{(c)}$) and cerebral autoregulation (whose effectiveness scales with $f_c^{(\mathrm{AR})}$).

The case of breast CHS spectra is qualitatively different. Because Arg(**[HbO]**)-Arg(**[HbT]**) and Arg(**[Hb]**)-Arg(**[HbO]**) are essentially zero, we can conclude that blood volume oscillations are the dominant source of hemoglobin concentration oscillations.

Therefore, oxy-, deoxy-, and total hemoglobin concentrations all oscillate in phase. Under these conditions, |**[HbO]**|/|**[HbT]**| specifies the average hemoglobin saturation of the volume oscillating vascular compartments, S_V, for which we found a value of 83% ± 1% (see Figure 2.3(d)). We hypothesize that the highly compliant venous compartment provides the greatest contributions to these volume oscillations driven by blood pressure perturbations. This is similar to the case of spiroximetry, which was proposed to measure venous saturation from the blood volume oscillations associated with respiration (which also modulates arterial blood pressure). In studies where spiroximetry was applied to skeletal muscles, the average venous saturation was found within the range 70-80% [45], [49]. In a NIRS study using venous occlusion to measure venous saturation in the human forearm, $S^{(v)}$ ranged from 50-80% [50]. The value found by us for S_V in the breast is somewhat greater than reported values of venous saturation in skeletal muscle. This result may be due to a different balance of blood flow and oxygen consumption in breast tissue compared to skeletal muscle or to greater contributions from the arterial compartment to S_V.

2.4 Discussion

The model described in [25], [34] indicates that a pure blood flow oscillation induces a phase shift of π between [Hb] and [HbO], whereas a pure blood volume oscillation induces synchronous oscillations of [Hb] and [HbO]. Equation 2.1 and Equation 2.2, introduced in Section 2.2.2 , are the analytical equations in the hemodynamic model that we used in order to solve for the six unknown parameters. By solving for **[Hb]** (ω)/**[HbO]** (ω) and **[HbO]**(ω)/**[HbT]**(ω) instead of solving separately for the phasors **[Hb]** (ω), **[HbO]** (ω), and **[HbT]**(ω), we can cancel out unknown or frequency-dependent scaling factors for the amplitudes and phases of oscillations. However, to best explain the in-phase vs. out-of-phase contributions from blood volume and blood flow oscillations, the equations for **[Hb]**(ω) and **[HbO]**(ω) are shown here as a sum of contributions from blood volume (subscript V), blood flow (subscript F) and oxygen consumption (subscript O):

$$\mathbf{[HbO]}(\omega) = \mathbf{[HbO]}_{\mathrm{V}}(\omega) + \mathbf{[HbO]}_{\mathrm{F}}(\omega) + \mathbf{[HbO]}_{O}(\omega) \tag{2.4}$$

$$\mathbf{[Hb]}(\omega) = \mathbf{[Hb]}_{\mathrm{V}}(\omega) + \mathbf{[Hb]}_{\mathrm{F}}(\omega) + \mathbf{[Hb]}_{0}(\omega) \tag{2.5}$$

Table 2 contains the terms and signs associated with each of the contributions [25], [34]. In the results reported here, we have assumed that there was no modulation of the cerebral metabolic rate (CMRO$_2$) or tissue oxygen consumption during the experiments. Table 2 (first and second row) shows that an oscillation in any component (arterial, capillary, or venous) of the blood volume generates in-phase oscillations **[HbO]**$_{\mathrm{V}}$(ω) and **[Hb]**$_{\mathrm{V}}$(ω). Table 2 also shows that a given blood flow phasor **cbf**(ω) (i.e. blood flow oscillations) generates phase-lagged oscillations **[HbO]**$_{\mathrm{F}}$(ω) (because of the negative phase of the complex factor in square brackets in the third row of Table 2 (for details, see [34]) and oscillations **[Hb]**$_{\mathrm{F}}$(ω) that are in opposition of phase with **[HbO]**$_{\mathrm{F}}$(ω) (because of the opposite sign of the terms in the third and fourth row of Table 2). More precisely, even if blood volume and blood flow oscillations are in phase, **[HbO]**$_{\mathrm{F}}$(ω) and **[Hb]**$_{\mathrm{F}}$(ω) are lagging **[HbO]**$_{\mathrm{V}}$(ω) and **[Hb]**$_{\mathrm{V}}$(ω). Note also that **[HbO]**$_{\mathrm{F}}$(ω) and **[Hb]**$_{\mathrm{F}}$(ω) are frequency dependent, reflecting the nature of the low pass filters associated with the capillary and venous compartments. A combination of both blood flow and blood volume oscillations induces frequency-dependent oscillations **[HbO]** (ω) and **[Hb]** (ω) which feature a relative phase that depends on the relative contributions of flow and volume oscillations, the blood transit time in the microvasculature, and the presence of any phenomena (such as autoregulation mechanisms) that link flow and volume changes.

Table 2**.** Contributions to **[HbO]** (ω) and **[Hb]** (ω) from oscillations in blood volume (subscript V) or blood flow (subscript F) at frequency ω. The oscillations in blood volume and blood flow are represented by the phasors **cbv**(ω) and **cbf**(ω), respectively. The table also shows the effect of oscillations in the metabolic rate of oxygen (phasor $\mathbf{cmro_2}$(ω)) that are neglected in this work. ctHb is the concentration of hemoglobin in blood. Other symbols are defined in the text.

Term	Expression
$\mathbf{[HbO]}_{\mathrm{V}}(\omega)$	$+\mathrm{ctHb}\left[S^{(a)}\mathrm{CBV}_0^{(a)}\mathbf{cbv}^{(a)}(\omega)+\langle S^{(c)}\rangle \mathrm{F}^{(c)}\mathrm{CBV}_0^{(c)}\mathbf{cbv}^{(c)}(\omega)+S^{(v)}\mathrm{CBV}_0^{(v)}\mathbf{cbv}^{(v)}(\omega)\right]$
$\mathbf{[Hb]}_{\mathrm{V}}(\omega)$	$+\mathrm{ctHb}\left[\left(1-S^{(a)}\right)\mathrm{CBV}_0^{(a)}\mathbf{cbv}^{(a)}(\omega)+\left(1-\langle S^{(c)}\rangle\right)\mathrm{F}^{(c)}\mathrm{CBV}_0^{(c)}\mathbf{cbv}^{(c)}(\omega)+\left(1-S^{(v)}\right)\mathrm{CBV}_0^{(v)}\mathbf{cbv}^{(v)}(\omega)\right]$
$\mathbf{[HbO]}_{\mathrm{F}}(\omega)$	$+\mathrm{ctHb}\left[\frac{\langle S^{(c)}\rangle}{S^{(v)}}\left(\langle S^{(c)}\rangle-S^{(v)}\right)\mathrm{F}^{(c)}\mathrm{CBV}_0^{(c)}\mathcal{H}_{\text{RC-LP}}^{(c)}(\omega)+\left(S^{(a)}-S^{(v)}\mathrm{CBV}_0^{(v)}\mathcal{H}_{\text{G-LP}}^{(v)}(\omega)\right)\right][\mathbf{cbf}(\omega)$ $-\mathbf{cmro_2}(\omega)]$
$\mathbf{[Hb]}_{\mathrm{F}}(\omega)$	$-\mathrm{ctHb}\left[\frac{\langle S^{(c)}\rangle}{S^{(v)}}\left(\langle S^{(c)}\rangle-S^{(v)}\right)\mathrm{F}^{(c)}\mathrm{CBV}_0^{(c)}\mathcal{H}_{\text{RC-LP}}^{(c)}(\omega)+\left(S^{(a)}-S^{(v)}\mathrm{CBV}_0^{(v)}\mathcal{H}_{\text{G-LP}}^{(v)}(\omega)\right)\right][\mathbf{cbf}(\omega)$ $-\mathbf{cmro_2}(\omega)]$

Figure 2.3(a) and Figure 2.4 show that deoxy- and oxy-hemoglobin oscillations are in phase in breast tissue and out of phase in the brain. This is an indication that the hemodynamics measured with NIRS are dominated by blood volume dynamics in healthy breast tissue, whereas they result from both blood volume and blood flow dynamics in brain tissue. We hypothesize that this contrasting behavior is due, at least in part, to a difference in the elastic properties of breast and brain tissue; in particular, the presence of the rigid skull limits the vascular expansion in brain tissue that, instead, is not constrained

in breast tissue. Therefore, one may expect that the contributions of blood volume and blood flow to [Hb] and [HbO] are different in breast and brain tissue.

We observe that while the relative phase of [Hb] and [HbO] oscillations is related to the level of flow autoregulation, one may not associate a lack of phase shift between [Hb] and [HbO] oscillations with a lack of autoregulation. In fact, even in the absence of autoregulation, when blood flow oscillations passively follow mean arterial pressure oscillations so that cerebral blood flow and MAP (and, to a first approximation, cerebral blood volume) are in phase with each other, [Hb] and [HbO] oscillations are still, in general, out of phase with each other. This is because, as described in Section 2.1 and shown in Table 2, $[\mathbf{HbO}]_V(\omega)$ is in phase with $\mathbf{cbv}(\omega)$ whereas $[\mathbf{HbO}]_F(\omega)$ lags $\mathbf{cbf}$ (ω) as a result of the finite blood transit time in the microvasculature.

The phase relationship between [Hb] and [HbO] oscillations in breast tissue may be affected by the presence of breast cancer. Breast tumors have a larger elastic modulus than healthy breast tissue [51], and they are also known to have an abnormal vasculature [52]. For both of these reasons, [Hb] and [HbO] oscillations in breast tumors may no longer be dominated by blood volume effects, as in healthy breast tissue, since the stiffer tissue and abnormal blood vessels may result in a less compliant tumor vasculature. Based on the model and results described here, [Hb] and [HbO] oscillations would become increasingly out of phase with each other as the contribution of blood volume oscillations decreases.

The in-phase oscillations of deoxy- and oxy-hemoglobin in the healthy breast tissue permitted us to compute the oxygen saturation of hemoglobin in the volume-oscillating compartments, $S_{\mathrm{V}} = |[\mathbf{HbO}]_{\mathrm{V}}|/|[\mathbf{HbT}]|$, simply as the ratio $|[\mathbf{HbO}]|/|[\mathbf{HbT}]|$. To measure the saturation of the volume oscillating compartments in the brain, one must take into account the blood flow contributions to the measured hemoglobin concentration. Kainerstorfer *et al*. have described in detail how to account for contributions from blood flow in order to measure S_{V} in a general case where deoxy- and oxy-hemoglobin oscillations are not in phase with each other [53].

This work underlines the value of quantitative measurements of hemodynamic oscillations, be they induced by controlled perturbations in the arterial blood pressure (as done here) or be they spontaneously occurring. However, in order to interpret such quantitative measurements of oscillatory hemodynamics, it is important to understand the dynamic relationship between the measured quantities (deoxy- and oxy-hemoglobin concentrations in the case of NIRS) and the underlying physiological processes. In particular, this work highlights the qualitatively distinct behavior of different tissues (brain and breast) in response to the same systemic perturbation in arterial blood pressure.

For non-invasive optical studies of the human brain, it is important to consider the fact that, in addition to brain tissue, extracerebral tissue (scalp, skull, etc.) also contributes to the measured optical signals. In relation to the study reported here, this means that extracerebral hemodynamics may act as a confounding factor for the cerebral hemodynamics that we intend to investigate and compare to breast tissue hemodynamics. However, while potentially confounding contributions from extracerebral hemodynamics may affect our measurements of the relative phase shift of [HbO] and [Hb] oscillations, they would not affect the main finding of this work that cerebral [HbO] and [Hb] oscillations are out of phase, whereas [HbO] and [Hb] oscillations in the healthy breast are in phase. Nevertheless, in an effort to quantify the effect of extracerebral hemodynamics on our dynamic NIRS measurements, we are currently exploring the application of a two-layer diffusion model to discriminate superficial and deep-tissue hemodynamics [37].

2.5 Conclusion

This study has shown that blood-pressure-induced hemodynamic oscillations behave qualitatively differently in the healthy breast and in the healthy brain. Specifically, the different phase delays between [Hb] and [HbO] oscillations observed in the breast (~0° in the range 0.04-0.08 Hz) and the brain (~-200° at 0.06 Hz) may be attributed to different relative contributions of blood flow and blood volume oscillations to the measured oxy- and deoxy-hemoglobin concentrations. The situation may be different in pathologic conditions, which may affect the vascular compliance, the microvascular architecture, normal physiological mechanisms, and the elastic properties of tissue. In this case, a quantitative assessment of hemodynamic oscillations, possibly as a function of frequency as done in CHS, may offer diagnostically relevant information for pathologic conditions. The broad implications of this work are that CHS may be sensitive to perturbations to the integrity of the vasculature and hemodynamics in the brain (i.e. subarachnoid hemorrhage, traumatic brain injury, stroke, etc.) and in the breast (i.e. breast cancer). A thorough characterization of hemodynamic oscillations in tissue and their accurate interpretation can have a significant impact in the study of microvascular circulation and the assessment of its integrity.

Chapter 3: Frequency-resolved analysis of coherent oscillations of local cerebral blood volume and systemic mean arterial pressure

3.1 Introduction

Oscillations of systemic mean arterial pressure (MAP) induce localized responses in the body's microvasculature, including oscillations in the cerebral blood volume. The dynamics between the two physiologic signals may reflect effects from cerebral blood flow (CBF) and transit time though the microvasculature as well as effects from the vessel mechanical properties. Cerebral autoregulation (CA), the mechanism that maintains stable CBF despite changes in cerebral perfusion pressure (CPP), plays a large role in how CBF responds to oscillations of MAP. There has been an increasing interest in using indices of CA to guide therapy at the hospital bedside [54]. A characterization of cerebral blood volume changes in relation to MAP changes may improve the understanding of how they manifest effects of CA. The effects of CA [14] and the transit time of blood [34] on the phase dynamics of oxyhemoglobin and deoxyhemoglobin are frequency dependent (i.e. they depend on the frequency of the pressure wave), so we have focused on a frequency-resolved characterization of cerebral blood volume (proportional to the sum of oxyhemoglobin and deoxyhemoglobin) vs systemic mean arterial pressure.

Cerebrovascular pressure reactivity has been used as a metric to quantify the relationship between cerebral blood volume and arterial blood pressure. This metric describes the general efficiency of cerebral vessels in performing volume changes in response to MAP changes. The pressure reactivity index (PRx) quantifies the reactivity by correlating slow-wave oscillations (<0.05 Hz) of intracranial pressure (ICP; measured invasively) and MAP over time with a moving window. ICP is used as a surrogate for cerebral blood volume. A high positive correlation coefficient between the two signals indicates pressure passive vasculature while a negative correlation coefficient indicates vessel reactivity. Higher, or more positive, PRx has been associated with worse outcomes in head-injured patients [55]. A near-infrared spectroscopy (NIRS) based hemoglobin volume index (HVx) has been proposed as a non-invasive alternative to the PRx [56]–[58]. Rather than using ICP, this index correlates total cerebral hemoglobin concentration ([HbT]) with MAP. [HbT] is proportional to local blood volume.

Cerebrovascular pressure reactivity is indicative of the ability of vessels to appropriately alter diameter in response to MAP changes. Cerebral autoregulation (CA) is the underlying mechanism that controls CBF via changes in arteriole resistance – hyperperfusion is reduced with arteriole constriction while hypoperfusion is increased with arteriole dilation [59], [60]. Lee at al note that in most physiological instances, the limits of pressure reactivity are wider than the limits of autoregulation, meaning that the range of blood pressures over which blood volume is responsive to blood pressure changes is wider than the range of blood pressures over which blood flow is constant [56]. In patients with traumatic brain injury, the correlation between cerebral pressure reactivity and CA has been moderate but highly significant [61]. NIRS has been used in several studies to quantify static [62] autoregulation or autoregulation at very low frequencies (between 0.003 to 0.05 Hz) by comparing ABP to a cerebral tissue oxygenation index with a similar approach as the one used to compute PRx or HVx [63]–[67].

A different way to assess CA is to induce oscillations [32] or transient changes [13] in CPP via changes in systemic mean arterial pressure (MAP). CBF is continuously and synchronously recorded with MAP so that their dynamic relationship may be used as a metric of CA [8]. Out-of-phase CBF and MAP time traces indicates that CBF is successfully counteracting MAP changes, while in-phase CBF and MAP indicates that CBF is passively following MAP. A passive relationship between CBF and MAP puts the brain at risk for injury from both increases and decreases in MAP.

Currently, the most commonly used method for measuring CBF in the assessment of dynamic CA is transcranial Doppler ultrasound (TCD) which monitors CBFV in the macrovasculature [14]. Autoregulation assessment in the macrovasculature is valuable for cerebral health assessment. However, it is a regional measure that may not be sensitive to focal deficits of autoregulation. For this reason, there has been interest in the assessment of localized autoregulation in the cerebral microvasculature. In addition to being continuous, a blood flow measurement technique for the microvasculature should be quantitative, non-invasive, and portable to enable accurate assessment of the timing of hemodynamic changes at the hospital bedside. Biomedical optics has two candidates that meet these requirements: coherent hemodynamics spectroscopy (CHS) and diffuse correlation spectroscopy (DCS) [8]. CHS employs NIRS for measurement of oxyhemoglobin and deoxyhemoglobin concentrations in cerebral tissue. A hemodynamic model relates coherent oscillations of the hemoglobins at different frequencies to compute physiologic parameters such as the transit time of blood in the capillaries and the transit time of blood in the venules [34]. With the computed parameters, the model may be used to compute relative blood flow changes, absolute CBF, and the efficiency of autoregulation [47]. The ability of CHS to quantify changes in CA has been validated with a study in which subjects performed normal breathing followed by hyperventilation to induce hypocapnia [35]. Ten out of eleven subjects in the study were found to respond to hypocapnia with the expected enhancement of autoregulation. The other biomedical modality, DCS, transmits near-infrared light to the cerebral microvasculature and then a photodetector and autocorrelator track the decay of autocorrelation between photons that have been scattered by moving red blood cells. A model fits for the decay rates over time to produce a time trace of relative changes in cerebral blood flow. DCS has also been used to assess the CA in healthy adults and was validated against TCD [68].

Compliance of the microvasculature is the key mechanical property contributing to the response of blood vessels to systemic MAP changes. Vessel compliance is the ratio between changes in blood volume, V, to changes in blood pressure, P, in a vessel segment: $\frac{\Delta V}{\Delta P}$. The arterial and venous compartments have different compliances, and research efforts have mostly focused on characterizing arterial compliance. Carrera et al extracted cerebral arterial blood volume from cerebral blood flow velocity (CBFV) measurements by transcranial Doppler to find that arterial compliance significantly decreased during hypocapnia relative to during normocapnia in healthy subjects [69]. Arterial compliance has also been studied with NIRS. A high density configuration of NIRS sources and detectors has been used to measure arterial compliance over the whole head by analyzing features of the optical signals at the frequency of the heart pulsation [70], [71]. It was found that arterial compliance was associated with factors such as cardiorespiratory fitness and age.

We see then that compliance as well as CBF may contribute to the dynamic relationship between cerebral blood volume and MAP. There has been a large focus on quantifying the frequency-dependent relationship between CBF and MAP. There has been less focus on the study of the frequency-dependent relationship between cerebral blood volume and MAP. Tzeng and Ainslie make a case that the relationship between arterial pressure with other physiologic signals at 0 Hz or close to 0 Hz does not indicate the interplay of these signals at higher frequencies [72]. In our present study, we have analyzed the relationship between local cerebral blood volume and systemic mean arterial pressure with a frequency-resolved approach. Transfer function analysis (TFA) is a popular approach for assessing the frequency dependence of autoregulation which is typically active below the frequency range of 0.3 Hz [14], [73]. In another group, it has also been applied to study cerebrovascular pressure reactivity in patients with acute traumatic brain injury. The phase shift between ABP and ICP was computed with the wavelet transform. It was found that ABP and ICP were in phase at higher frequencies (around 1 Hz), and at some point in the lower frequency range would become out of phase. A negative PRx indicates a pressure-active vascular bed in which ABP and intracranial pressure (ICP) change in opposite directions to maintain a stable CPP. For patients with a negative PRx (intact cerebrovascular reactivity), the phase shift occurred in the range of 0.07-0.14 Hz, while the signals were phase-shifted between 0.006-0.07 Hz in patients with a larger PRx [74]. In our study, we have applied the TFA approach to the study of cerebral blood volume vs MAP using total hemoglobin concentration, measured with NIRS, and continuous MAP. The frequency dependent relationship between cerebral hemoglobin concentrations and systemic MAP has previously been presented in one study with 3 subjects [75]. They analyzed spontaneously occurring oscillations. It was found that oxyhemoglobin concentration and arterial blood pressure (ABP) were generally in phase at frequencies close to 0, followed by an increasing lag of oxyhemoglobin relative to ABP which plateaued between 30-60 degrees during 0.1 Hz spontaneous oscillations. In another study, focusing on 0.1 Hz oscillations induced by paced breathing, the phase between ABP and total hemoglobin was 22.6 degrees on average for 37 healthy subjects with ABP leading [32]. In our study, we have measured 22 healthy subjects to characterize the relationship between MAP and total hemoglobin ([HbT]) across multiple frequencies in the range of 0.04 to 0.2 Hz. We used pneumatic thigh cuffs to induce controlled MAP oscillations to drive cerebral blood volume oscillations. We also implemented a time-varying approach for coherence analysis with a sliding short time Fourier transform. This enabled us to detect not only coherence between signals during thigh cuff oscillations but also spontaneously coherent oscillations, thus creating transfer functions with several points for characterization. With coherent hemodynamics spectroscopy, we have a model to compute cerebral blood flow from changes in oxyhemoglobin and deoxyhemoglobin concentration changes measured with NIRS as well as the efficiency of autoregulation. Total hemoglobin, the sum of oxy- and deoxyhemoglobin, is also measured with NIRS and is proportional to cerebral blood volume, as mentioned earlier. We therefore have the opportunity to determine the interplay of blood flow and blood volume under the effects of autoregulation.

3.2 Methods

3.2.1 Subjects

Twenty two healthy subjects (15 females; 7 males; age range: 21-51 years old) participated in the study. The Tufts University Institutional Review Board approved the experimental protocol, and the subjects provided written informed consent prior to the experiment. The data for nine of the female subjects has been previously analyzed for a comparison of the phase and amplitude between oxyhemoglobin and deoxyhemoglobin concentration oscillations in brain tissue [76].

3.2.2 Experimental protocol and data acquisition

Figure 3.1 is a flow chart to illustrate the framework for data collection and analysis. Each of the blocks will be described in detail in the following subsections of *Methods*.

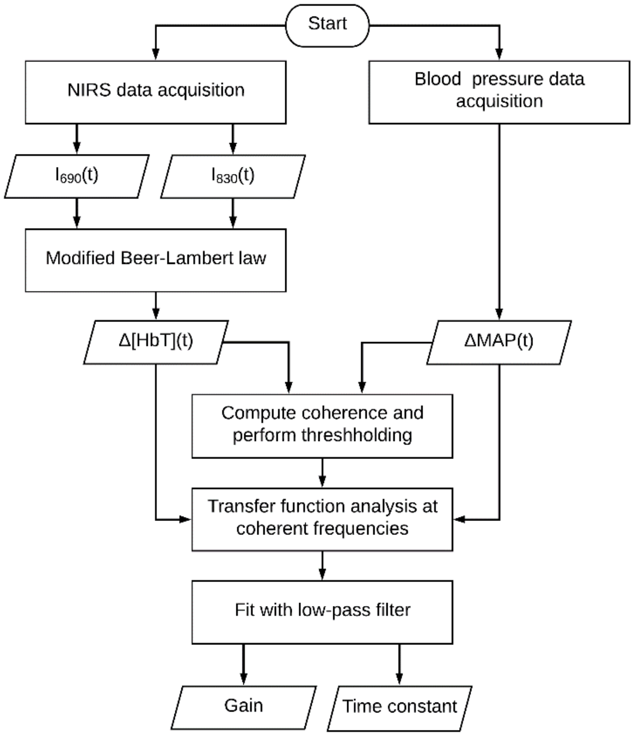

Figure 3.1. Flow chart of data collection and analysis. $I_{690}(t)$ and $I_{830}(t)$ are the light intensities detected at 690 nm and 830 nm, respectively. Δ[HbT](t) is the relative change in total hemoglobin concentration. ΔMAP(t) is the change in mean arterial pressure relative to the baseline absolute value of mean arterial pressure.

In each experiment, the subject sat in a chair with their feet on the floor or sat on a bed with their back at a ~30 degree angle and their legs parallel to the floor. A near-infrared spectroscopy probe was placed against the forehead (8 subjects: spatial mapping probe with eight source-detector channels; 14 subjects: single source-detector channel). For full details of the particular set up for each subject, see Appendix A2. A diagram of the channel locations for the spatial mapping probe is shown in Figure 3.2. The probe was custom made from a 3D printed, flexible plastic frame with holes for source and detector optical fibers. The frame was surrounded with black silicone. The probe was connected to a frequency-domain commercial NIRS instrument (10 subjects: OxiplexTS, ISS Inc., Champaign, Illinois; 12 subjects: Imagent, ISS Inc. Champaign, Illinois). Light with wavelengths of 690 nm and 830 nm was transmitted to the prefrontal cortex. For each pair of sources, the light intensity ($I_{690}(t)$ and $I_{830}(t)$) after exiting the tissue was recorded with a detector at a distance of 3.5 cm away. The Modified-Beer Lambert law was used to compute relative changes in oxyhemoglobin (Δ[HbO_2]), deoxyhemoglobin (Δ[Hb]), and total hemoglobin (Δ[HbT]) in units of microMolar (μM). The relative differential path length and baseline optical properties for 690 nm light to 830 nm light were determined either by a multi-distance approach (for single probe) [27] or a self-calibrating approach (for the spatial-mapping probe) [77]. Extinction coefficients for oxyhemoglobin and deoxyhemoglobin were selected from [22]. To induce MAP oscillations, pneumatic cuffs were placed around both thighs and were connected to a cuff inflation system (E-20 Rapid Cuff Inflation System, D.E. Hokanson, Inc., Bellevue, Washington). A microcontroller was connected to the regulator of the inflation system via a ¼ inch stereo phone plug in order to set customized rates of inflation and deflation (Arduino Uno R3). Maximum inflation of the cuffs was at least 180 mmHg in order to induce arterial occlusion. The air pressure in the thigh cuffs was continuously monitored with a digital manometer (Series 626 Pressure Transmitter, Dwyer Instruments, Inc., Michigan City, Indiana). Continuous arterial blood pressure (ABP) was recorded with a beat-to-beat blood pressure monitoring system (NIBP100D, BIOPAC Systems, Inc., Goleta, California). A pulse oximeter measured heart rate (OXY100E, BIOPAC systems, Inc, Goleta, California or Nellcor PM-1000, Nellcor Inc., Hayward, CA). All signals were recorded synchronously with a sample rate of at least 6.25 Hz.

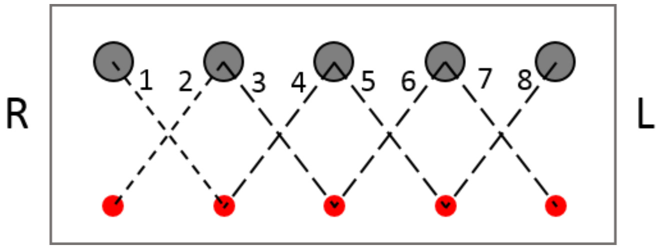

Figure 3.2. Spatial mapping probe diagram. Detectors are indicated with the large gray circles. Pairs of co-localized 690 nm and 830 nm light sources are indicated with the red circles. The “R” and “L” indicate the parts of the probe that were against the right and left sides of the forehead, respectively. The dashed lines connect the source-detector pairs that were used in the analysis. The source-detector distance is 3.5 cm for each pair. The channels are labeled 1-8 next to the dashed lines.

Experiment duration was 20-60 minutes. In each experiment, the thigh cuffs inflated at frequencies ranging from 0.04 Hz to 0.20 Hz in order to induce MAP oscillations that would drive coherent changes in cerebral hemodynamics. The first protocol included separately induced oscillations with a baseline period in between each epoch of oscillations. Figure 3.5 shows an example of this type of protocol for the second half of the experiment. The boxes represent a time duration of 90 seconds followed by 90 second breaks. The second protocol was a “chirp” like protocol, meaning that the frequency of oscillations linearly increased over time without baseline periods in between each frequency. Each frequency lasted for a duration of 6 periods. An example of this type of protocol is shown in Figure 3.5 for the first half of the experiment. Each type of protocol consisted of the same frequencies-the difference was in the timing in duration of the frequencies. See Appendix A2 for induced frequencies for each subject. The variation in experimental protocols is acceptable for our study, because the requirements to apply our analysis methods are only time traces of ΔMAP and Δ[HbT]. Coherence between ΔMAP and Δ[HbT] was computed across the frequency range of interest, as described in more detail in the next section. Coherence thresholding enabled us to select both induced and spontaneously coherent frequencies for use in the transfer function analysis.

Figure 3.3 shows an example of the time traces collected for each experiment in order to convey how cuff pressure changes induced both systemic changes in MAP as well as local Δ[HbT]. The traces in Figure 3.3 are from the data set of subject 5 (channel 8) during the segment of the experiment where 0.09 Hz oscillations were induced. The top panel shows the thigh cuff signal measured with the manometer. Gray rectangles indicate the start of inflation and start of deflation for each pulse of the thigh cuffs. The middle panel shows heart rate in units of beats per minute (bpm). The bottom panel shows the time traces for MAP (black line) and Δ[HbT] (gray line). We also provide example time traces for the chirp-like portion of the protocol for Subject 5 in Figure 3.4.

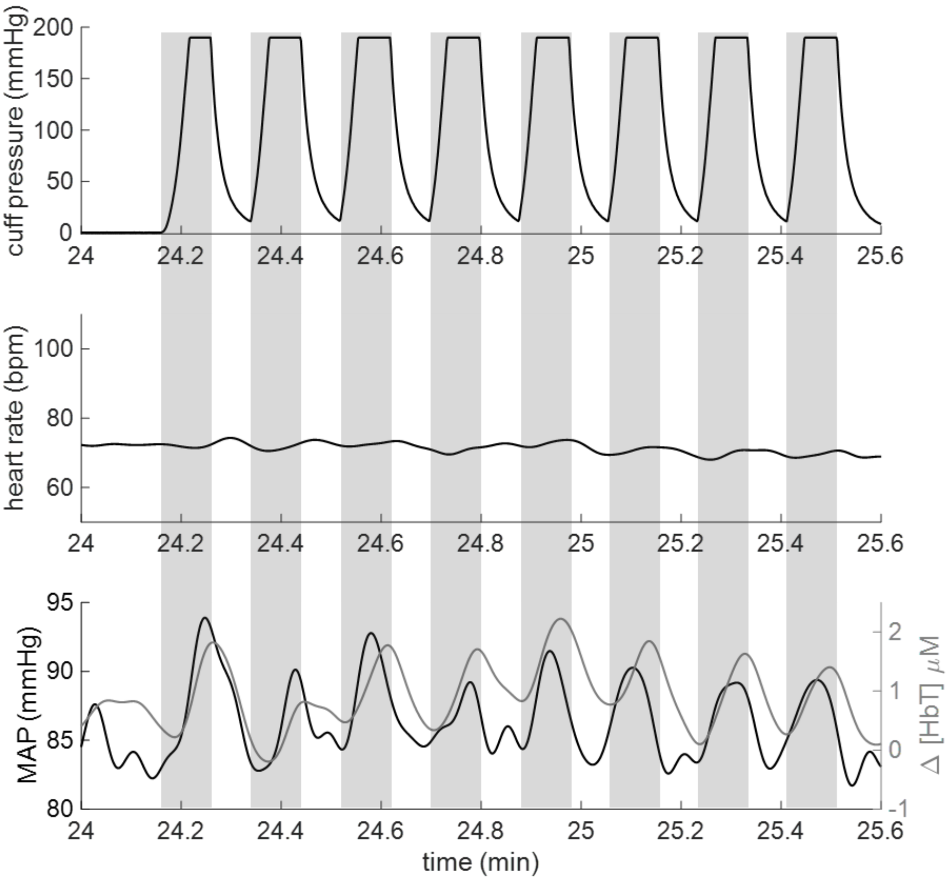

Figure 3.3. Example time traces of induced oscillations from Subject 5. The frequency is 0.09 Hz. Gray rectangles indicate the start of inflation to the start of deflation for each pulse of the thigh cuffs. Top panel: Thigh cuff pressure measured with the manometer. Thigh cuffs were inflated for 11 seconds and deflated for 11 seconds to induce oscillations around 0.09 Hz. Middle panel: Heart rate measured with the pulse oximeter in units of beats per minute (bpm). Bottom panel: MAP (black line) and total hemoglobin changes (Δ[HbT], gray line). Signals in the middle panel and bottom panel have been low-pass filtered with a cut-off frequency of 0.25 Hz to eliminate noise and heart rate pulsations for better visualization of oscillations in the low frequency range.

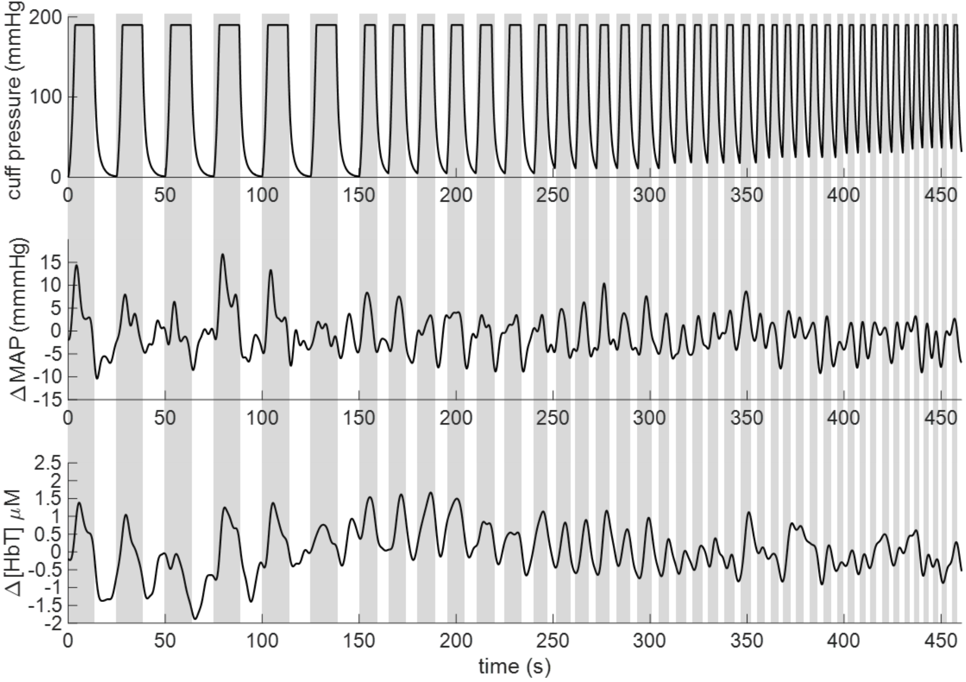

Figure 3.4. Time traces for chirp-like portion of protocol for subject 5. Top panel: Thigh cuff pressure signal. Middle panel: ∆MAP. Bottom panel: ∆[HbT]. Time-axis is shown relative to 0 seconds to assist with interpretation of cuff inflation and deflation times. Gray bars also indicate the inflation times of the cuffs throughout all three panels.

3.2.3 Time-varying coherence and coherence threshold

The mean of MAP during baseline was subtracted from the signal in order to obtain relative changes of MAP in units of mmHg, notated as ∆MAP. In order to perform transfer function analysis (TFA) between ∆MAP and ∆[HbT] to characterize the relationship between the two signals, the coherence was computed to determine if the signals were sufficiently linearly coupled. Signals are coherent at a particular frequency when their relative amplitudes and phases are stable at this frequency. Because each frequency was induced sequentially, the two signals were non-stationary- the signals may have been coherent at a frequency during segments of the experiment but not necessarily for the entire experiment. Standard spectral approaches may miss detection of a coherent frequency if it is not present during the entire signal. Therefore, the coherence between ΔMAP and Δ[HbT] was computed with a time-varying approach based on the short time Fourier transform. The mean squared coherence as a function of frequency *f* and time *t*, $MSC_{\Delta MAP,\Delta[HbT]}(f,t)$, is as follows:

$$MSC_{\Delta MAP,\Delta[HbT]}(f,t) = \frac{\left|P_{\Delta MAP,\Delta[HbT]}(f,t)\right|^2}{P_{\Delta MAP,\Delta MAP}(f,t)P_{\Delta[HbT],\Delta[HbT]}(f,t)} \tag{3.1}$$

where $P_{\Delta MAP,\Delta[HbT]}(f,t)$ is the cross power spectral density between ΔMAP and Δ[HbT], $P_{\Delta MAP \Delta MAP}(f,t)$ is the power spectral density of ΔMAP and $P_{\Delta[HbT]\Delta[HbT]}(f,t)$ is the power spectral density of Δ[HbT]. Perfect linear coupling has a coherence of 1 and absent linear coupling has a coherence of 0. We selected to perform the spectral analysis with the short time Fourier transform (STFT) based on Welch's overlapped averaged periodogram method [78]. Our frequency range of interest was between 0 to 0.20 Hz. The performance of the STFT and wavelet approaches are similar, although the wavelet approach has a more straight forward implementation of a frequency-varying time resolution [38]. For our relatively narrow frequency range of interest, we decided to use the STFT approach because frequency-varying time resolution was not needed. The STFT was performed with a time resolution of 180 seconds and a frequency resolution of 0.0133 Hz. Each 180 second segment of data was divided into two windows with 50% overlap which were each multiplied by a Hamming window to reduce spectral leakage. The Matlab function "mscohere" performed the coherence computation. The window for analysis was shifted by 4 seconds in order to create a pseudo-continuous time trace of coherence for each frequency. The output of this procedure was an image of coherence, with time along the x-axis and frequency along the y-axis.

To compute a coherence threshold, we used the approach described by Sassaroli et al 2018 [79]. Two sequences of random numbers were generated to simulate time traces of $I_{690}(t)$ and $I_{830}(t)$ with zero mean. The modified Beer Lambert law computed the concentration of Δ[HbT]. Another sequence of random numbers was generated to simulate ΔMAP. Our approach for coherence analysis was applied to these independent sets of random numbers 1000 times to generate the null statistics for coherence. We found that coherence between ΔMAP and Δ[HbT] was significant at the 5% level if it was greater than 0.79, so we selected this value as our threshold. We applied this threshold to the image of coherence.

Following thresholding of the coherence image, we determined the connected components in the binary image (function "bwconncomp") which considers adjacent pixels as part of the same group. We computed the area of each separate group of connected pixels which we call clusters. We expected coherence between the two signals to be maintained for at least several seconds, indicating that single pixels or small clusters of pixels passing the threshold were likely to be noise. A second set of data for generating the null statistics for coherent cluster size was created with another run of 1000 random independent time traces of ΔMAP and Δ[HbT]. Upon thresholding with the selected value of 0.79, the size of each coherence region within the image was recorded. We computed that regions greater than 13 pixels had a 5% chance of being designated as coherent when they were not coherent. In the analysis of the experimental data, coherence was computed between ΔMAP and Δ[HbT]. We created a binary image with

1’s indicating pixels that passed the coherence threshold. Then the size of coherent clusters was computed and pixels in clusters whose size was less than 25 pixels were set to 0 in the binary image. We heuristically found that the threshold of 25 pixels, with a significance level of 0.2%, provided estimates of transfer functions with less variability than a threshold of 13 pixels without eliminating too many clusters. After the size thresholding, some single pixels protruded at the edges of clusters that we also considered as noise. A morphological filter was applied to the binary coherence image to eliminate protruding pixels.

3.2.4 Time-averaged transfer function analysis

The transfer function between ΔMAP and Δ[HbT] was computed with the same time resolution, frequency resolution, and windowing approach as the coherence computation. The Matlab function “tfestimate” was used for this portion of the analysis. The transfer function over frequency and time is written as follows:

$$H_{\Delta MAP,\Delta[HbT]}(f,t) = \frac{P_{\Delta MAP,\Delta[HbT]}(f,t)}{P_{\Delta MAP\Delta MAP}(f,t)} \tag{3.2}$$

where the magnitude of the transfer function is the relative change in micromolars of total hemoglobin to mmHg of mean arterial pressure. The phase of the transfer function is the $\text{phase}_{\Delta[\text{HbT}]-\Delta\text{MAP}}$. MAP oscillations lead [HbT] oscillations which means that the $\text{phase}_{\Delta[\text{HbT}]-\Delta\text{MAP}}$ is mathematically negative.

The time-frequency transfer function, at pixels that passed the thresholding procedure, was averaged across time with the assumption that each coherent pixel in time is a sample of the same transfer function. The result describes the relationship between

ΔMAP and Δ[HbT] as a function of frequency as shown in Equation 3.3 where ⟨ ⟩ indicates an average across time.

$$H_{\Delta MAP,\Delta[HbT]}(f) = \frac{\langle P_{\Delta MAP,\Delta[HbT]}(f,t)\rangle}{\langle P_{\Delta MAP,\Delta MAP}(f,t)\rangle} \quad (3.3)$$

3.2.5 Model fitting

Following the computation of the transfer functions, we summarized their features by fitting to the low-pass filter model of Equation 3.4 with two parameters: gain, *K*, and time constant, τ.

$$\Delta[HbT](f) = H_{\Delta MAP,\Delta[HbT]}(f)\Delta MAP(f) \cong \frac{K}{1+j2\pi f\tau}\Delta MAP(f) \quad (3.4)$$

The two parameter low-pass filter model was found by the Akaike information criterion [80] to be a suitable trade-off between model complexity and quality of fit to the data sets. We used a prediction error minimization algorithm in Matlab to determine the optimal parameters to describe the transfer function (function “pem”). The range for *K* was set between 0 and 2 µM/mmHg, and the range for τ was set between 0 and 6 seconds. The fit to each data point in the spectra was weighted by its average coherence over time such that errors associated with points with higher coherence contributed more to the loss function being minimized. The quality of fit was quantified with the normalized root mean square error between the measured data and the data estimated from the fit of the model, ranging from negative infinity for a bad fit to 100% for a perfect fit.

3.3 Results

3.3.1 Single probe location

For the analysis across all subjects, we selected the source-detector channel corresponding to the position on the left or right side of the forehead above the orbital rim. For all subjects who wore the spatial mapping probe, the left channel was arbitrarily selected for a consistent comparison across these subjects. Figure 3.5 shows the results of the time-frequency coherence computation for subject 5. The experiment duration was 40 minutes and the timing and frequencies of the induced thigh cuff oscillations are marked with red boxes in Figure 3.5. The center of each box indicates the central frequency and time. The top and bottom edges of the box indicate the frequency resolution, and the left and right edges of the box indicates the time resolution. The first section of red boxes indicates the portion of the experiment where we induced chirp-like oscillations for 6 pulses over 7 frequencies. The second section of red boxes shows where oscillations were performed with the thigh cuffs for 90 seconds each, followed by 90 second breaks, over 7 frequencies. Figure 3.5 shows the coherence values and indicates that the thigh cuffs successfully enhanced coherence between the two signals. It is also visible in the figure that the signals were spontaneously coherent with each other for portions of the experiment in which the thigh cuffs were not oscillating. Figure 3.5 was generated with a time window sliding by one sample at a time for visualization purposes. Figure 3.6 shows the times and frequencies at which the coherence between the two signals passed the coherence (left panel) and size (right panel) thresholds where yellow indicates the pixels that have passed the thresholds. In this case, the results are shown for the actual time window we used in the analysis which slid by 4 seconds at a time.

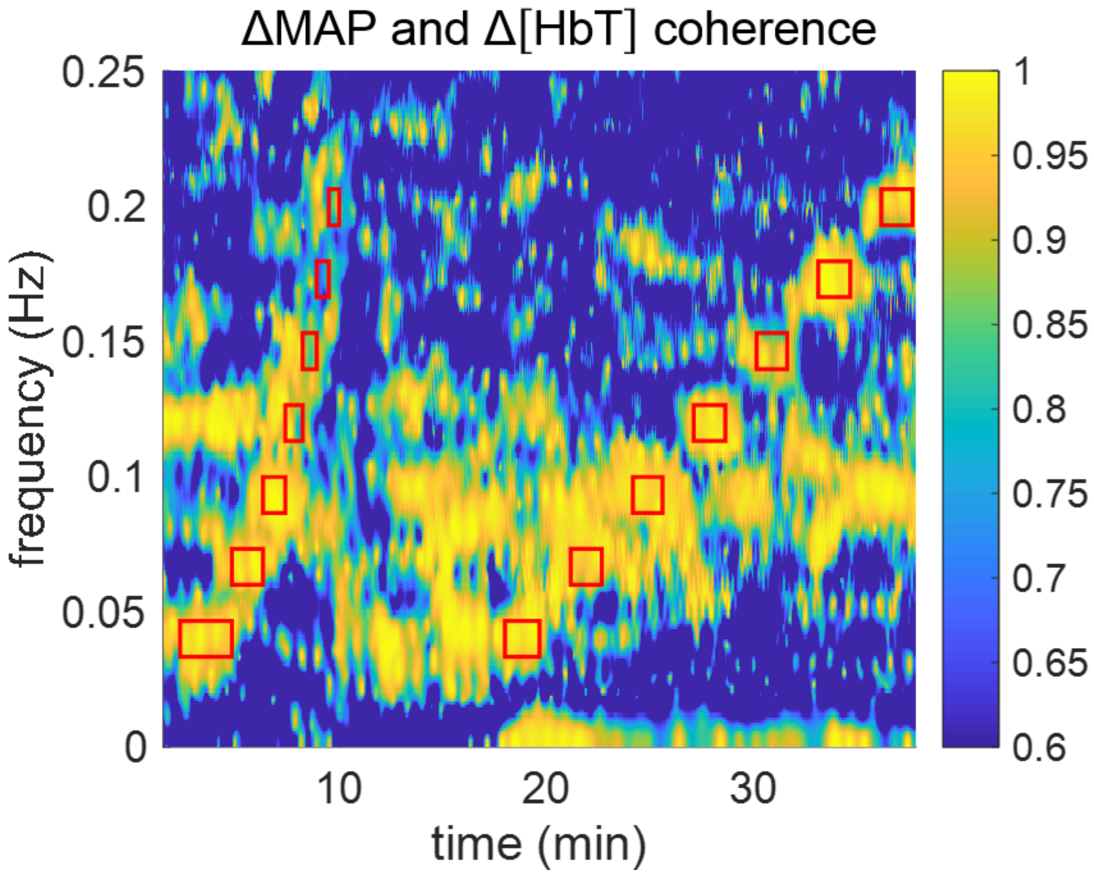

Figure 3.5. Coherence between ΔMAP and Δ[HbT] for subject 5. Red boxes indicate timing and frequency of oscillations induced with the pneumatic thigh cuffs. The group of boxes on the left are associated with the chirp-like protocol and the group of boxes on the right are associated with oscillations of equal duration and spacing across time.

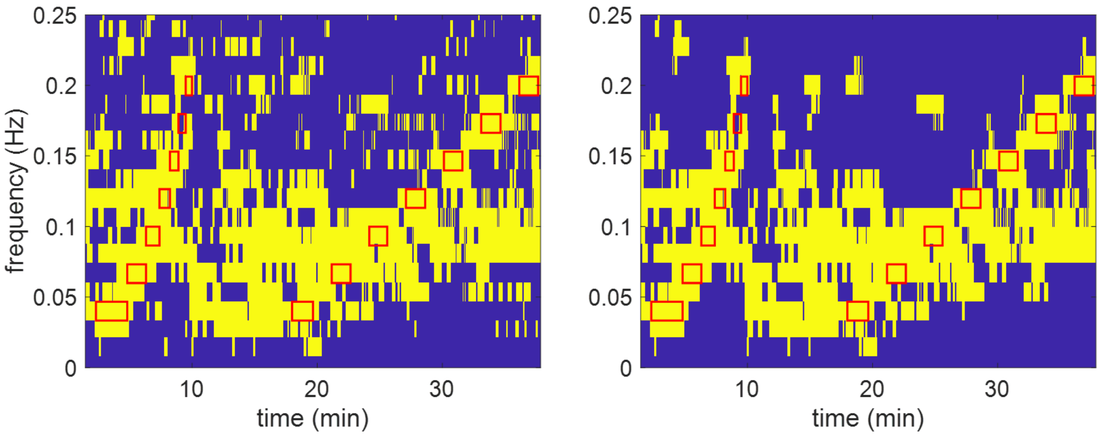

Figure 3.6. Binary coherence between ΔMAP and Δ[HbT] over time and frequency where yellow is coherent and blue is not coherent for subject 5. Red boxes indicate timing and frequency of oscillations induced with the pneumatic thigh cuffs. Left panel: Binary image of pixels that passed the coherence threshold. Right panel: Binary image of pixels that passed the coherence threshold and then the cluster size threshold followed by clean up of protuding pixels.

Figure 3.7 shows the results of the transfer function analysis for the data of subject 5, channel 8. The left panel of Figure 3.7 shows the amplitude ratio between ΔMAP and Δ[HbT] at the coherent frequencies. The right panel shows the phase difference between ΔMAP and Δ[HbT] at the coherent frequencies. In these figures, the blue color indicates frequencies that did not pass the coherence thresholding.

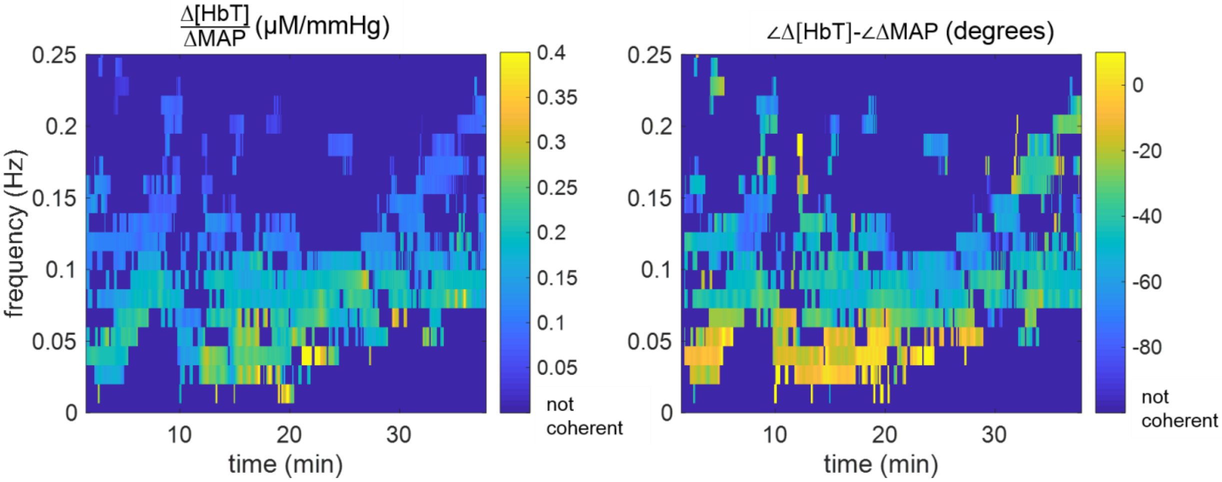

Figure 3.7. Transfer function analysis results for subject 5. Left panel: Amplitude ratio, between ΔMAP and Δ[HbT], $\left|H_{\Delta MAP,\Delta[HbT]}(f,t)\right|$, at the coherent pixels indicated by the right panel of Figure 3.6. Right panel: Phase difference between ΔMAP and Δ[HbT] at the coherent pixels, $\angle H_{\Delta MAP,\Delta[HbT]}(f,t)$. Regions of the images which are dark blue did not pass the coherence thresholding.

Following the computation of $H_{\Delta MAP,\Delta[HbT]}(f,t)$, the data was averaged across time, including both the chirp and oscillation protocols, to produce the spectra $H_{\Delta MAP,\Delta[HbT]}(f)$. The average values and the standard error of the mean are shown as the blue circles with error bars in Figure 3.8 for Subject 5. We also include results in Figure 3.8 for four additional representative subjects. A summary of the average relative amplitude and phase between ΔMAP and Δ[HbT] for all twenty two subjects is shown in Table 3.

Table 3. Frequencies, number of subjects n whose spectra included the frequency, group average and standard error for amplitude ratio between Δ[HbT] and ΔMAP, group average and standard error for phase difference between ∠[HbT] and ∠MAP.

Frequency (Hz)	n	$\frac{\Delta[\mathrm{HbT}]}{\Delta\mathrm{MAP}}$ μM/mmHg	∠Δ[HbT]-∠ΔMAP (degrees)
0.040	17	0.11 ± 0.01	-21 ± 4
0.053	21	0.10 ± 0.01	-25 ± 3
0.067	22	0.09 ± 0.01	-33 ± 3
0.080	22	0.08 ± 0.01	-41 ± 3
0.093	22	0.08 ± 0.01	-42 ± 3
0.106	21	0.07 ± 0.01	-48 ± 4
0.120	19	0.06 ± 0.01	-54 ± 4
0.133	20	0.06 ± 0.01	-58 ± 5
0.146	18	0.07 ± 0.01	-55 ± 5
0.160	18	0.06 ± 0.01	-60 ± 5
0.173	16	0.05 ± 0.01	-64 ± 6
0.186	17	0.05 ± 0.01	-54 ± 6

Fitting to the low-pass filter model of Equation 3.4 was performed to obtain parameter values of K= 0.22 ± 0.02 μM/mmHg and τ= 1.60 ± 0.17 seconds for Subject 5. The quality of the fit was 67%. The lines determined by the fitted parameters for the subjects in Figure 3.8 are also shown in that figure.

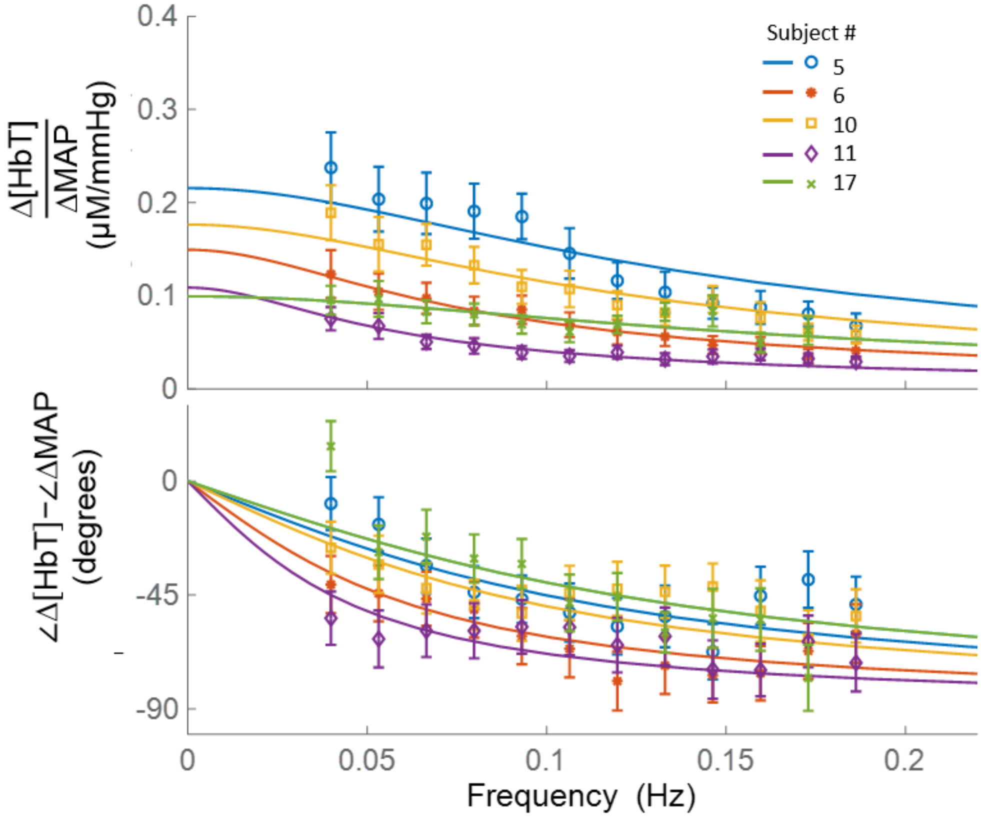

Figure 3.8. The fitted transfer functions between Δ[HbT] and ΔMAP and points for 5 representative subjects. Symbols are the average values and error bars are the standard error of the mean. The line is the best fit computed for the low-pass filter model.

Figure 3.9 provides a summary of the parameters and quality of fits for the 22 subjects. The top panel shows that the gain of the transfer function ranged from 0.03 to 0.24 μM/mmHg. The average is 0.12 ± 0.05 μM/mmHg. The middle panel shows that the time constant of the transfer function ranged from 0.47 to 4.15 seconds. The average is 1.7± 0.96 seconds. The bottom panel shows that the quality of fit ranged from 39% to 87%. The average is 61± 13%.

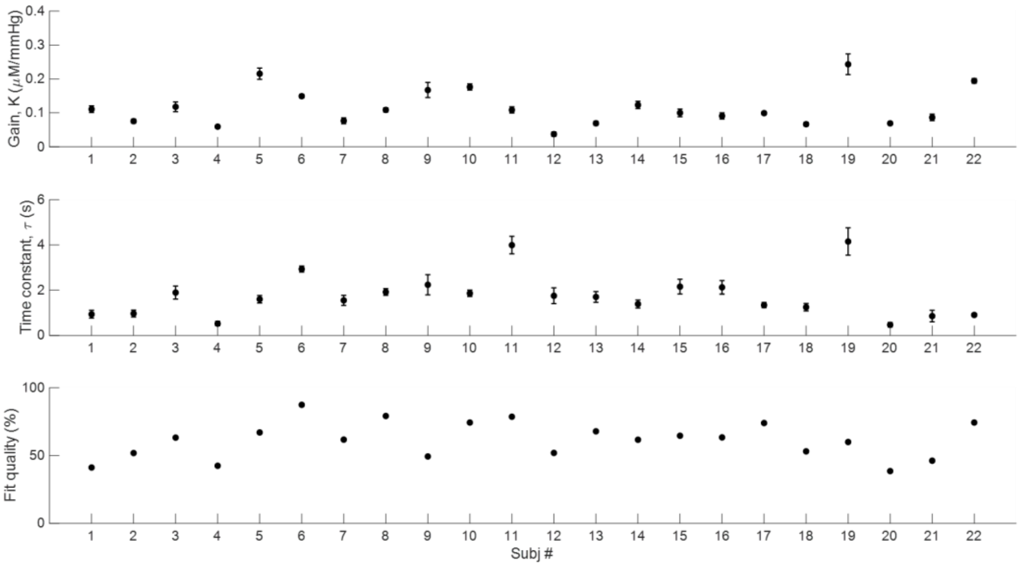

Figure 3.9. Parameters for 22 subjects. Top panel: Gain, K. Middle panel: Time constant, τ. Bottom panel: Fit percent.

3.3.2 Spatial Mapping

Eight of the subjects wore a spatial mapping probe that covered eight locations across the prefrontal cortex. The transfer function between ΔMAP and Δ[HbT] was calculated for each of the channels and a fit to the low-pass model was performed. Figure 3.10 shows the averages and errors for the spectra of all 8 channels computed from the data of subject 5, and the lines are defined by the best fit parameters.

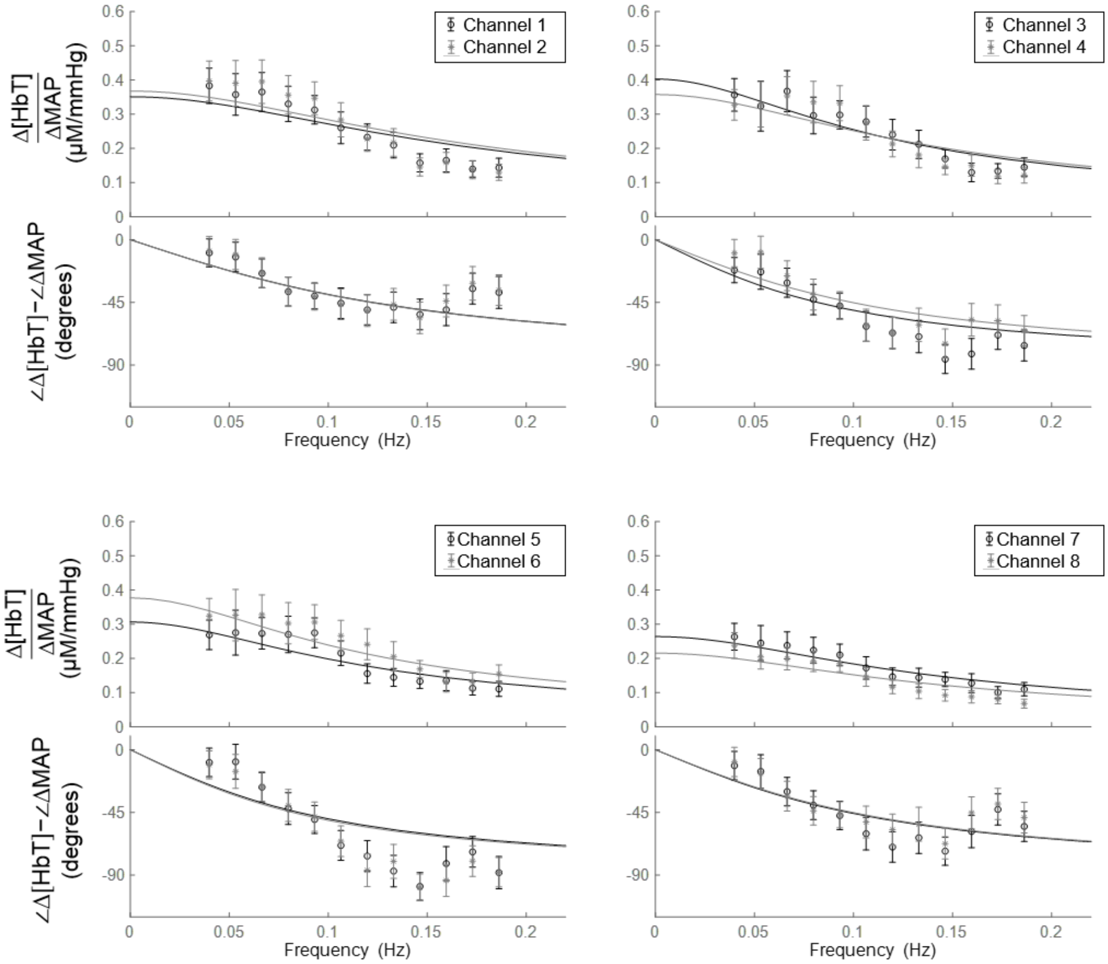

Figure 3.10. The spectra and best fit lines computed for all channels measured with subject 5. We overlay two spectra in each panel for easier visualization.

Figure 3.11 summarizes the parameter values with box plots for the 8 channels in all 8 subjects. The central line in each rectangle is the median parameter value across the 8 channels. The bottom edge is the 25th percentile and the top edge is the 75th percentile. The whiskers extend to the most extreme data points that are within ±2.7 standard deviations of the mean value. Points beyond the whiskers are considered outliers and are marked with an “x”.

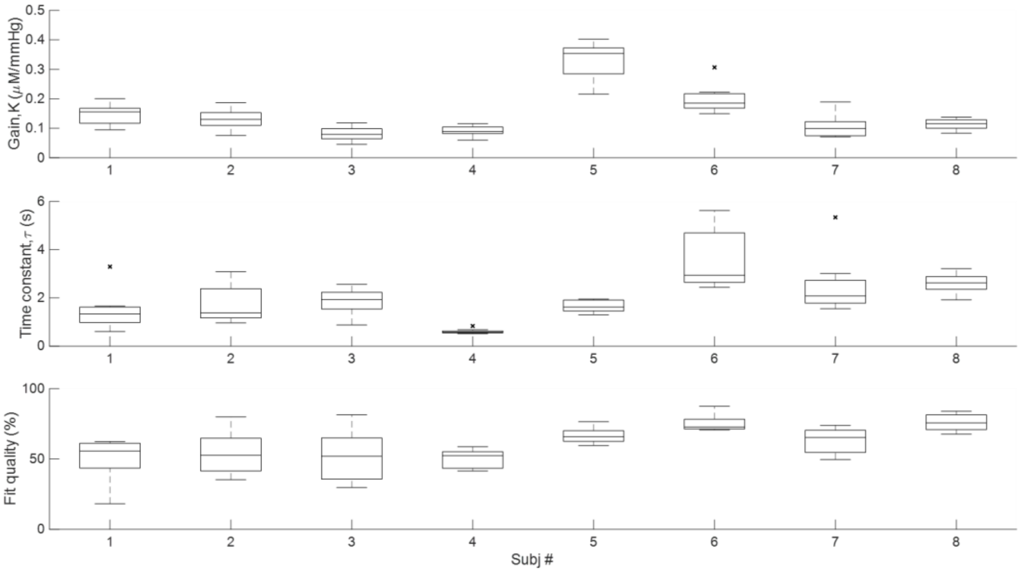

Figure 3.11. Box plots for the 8 subjects with the spatial mapping probe where each box represents the spread of parameters across the 8 channels in the probe. Top panel: Gain, K. Middle panel: Time constant, τ. Bottom panel: Fit quality.

3.3.3 Comparison of thigh cuff oscillation protocols

As shown in Appendix A2, for 10 subjects, the experiment consisted of two kinds of protocols. In Figure 3.12, we show the parameters if we use our frequency domain (FD) data analysis approach for the full experimental data set, only the segment of spaced oscillations, or only the segment of the chirp. The bottom panel shows the time length of data used for computing each set of parameters.

We also performed fitting between ΔMAP and Δ[HbT] in the time domain (TD). Each signal was segmented to the chirp portion of the experiment. For example, the signal in the middle panel of Figure 3.4 (ΔMAP) was the input and the signal in the bottom panel of Figure 3.4 (Δ[HbT]) was the output for the model. The time domain traces were fit with the same low-pass model structure, using again the predication error minimization algorithm which sought to minimize the difference between the measured output and the predicted output of the model. The benefit of this approach is that the amplitude and phase of the transfer function do not have to be estimated prior to fitting with the model, because the time traces are fit directly. The assumption with this approach is that the segments of Δ[HbT] and ΔMAP are coherent with each other across the entire time window of several minutes. An example of the resulting agreement between the measured Δ[HbT] and computed Δ[HbT] time traces, based on applying the estimated model to ΔMAP is shown in Figure 3.13.

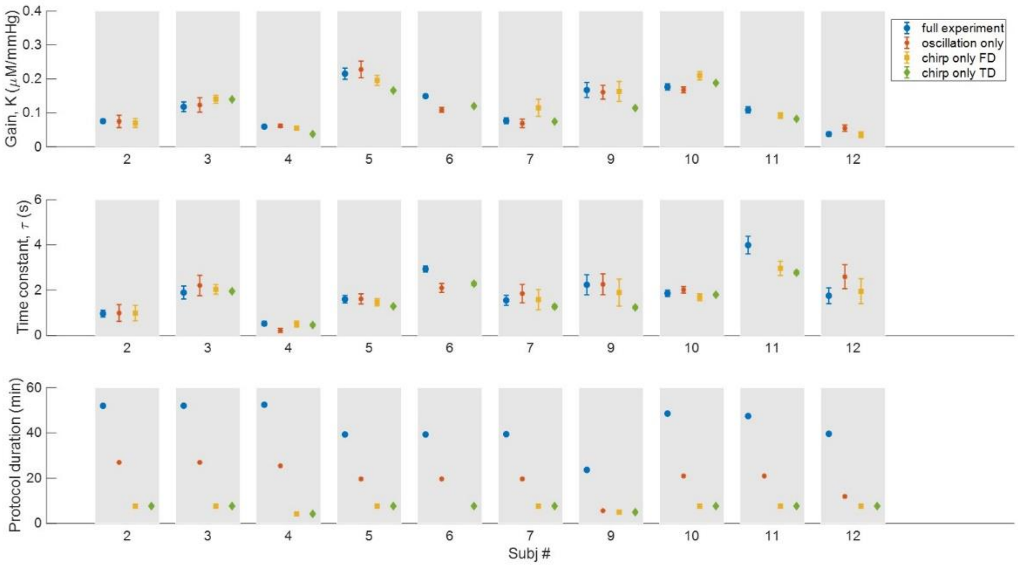

Figure 3.12. Parameters and duration of four protocols/fitting approaches for 10 subjects that had both sets of data. Points have been excluded for which the quality of the model fit was less than 10%.

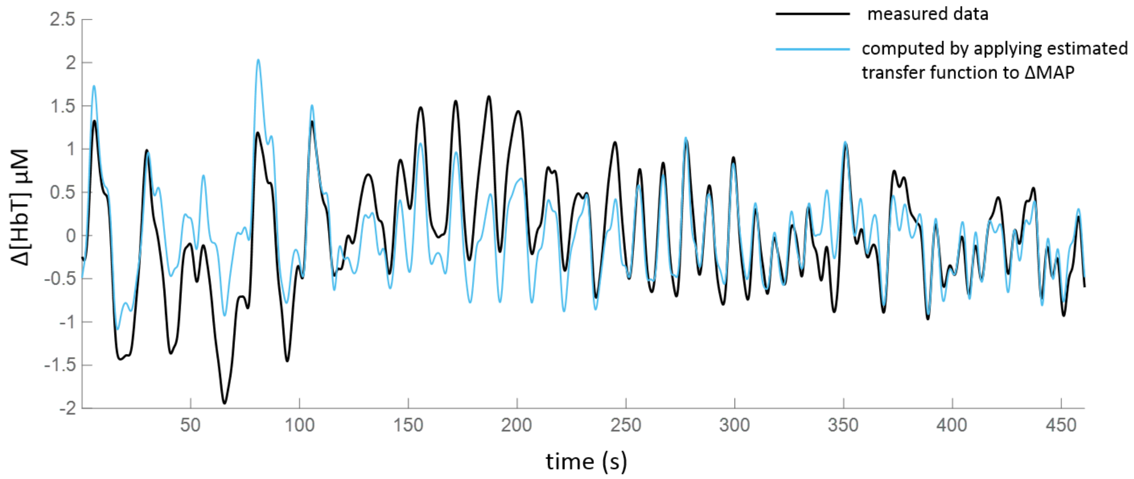

Figure 3.13. Measured Δ[HbT] (black line) and computed Δ[HbT] (light blue line). Computed Δ[HbT] was determined by applying the estimated model for the relationship between Δ[MAP] and Δ[HbT]. These results are for subject 5.

We created correlation plots and Bland-Altman plots [81] to assess the correlation and agreement between the parameters computed from each protocol, respectively. The results for a comparison between the oscillation approach (red asterisks in Figure 3.12) and chirp frequency domain approach (yellow squares in Figure 3.12) are shown in Figure 3.14. For the gain parameter, *K*, the correlation coefficient is 0.82. The coefficient of variation (standard deviation of differences divided by mean) was 20%. The average difference is 0.01 µM/mmHg and it is not statistically different from 0. For the time constant parameter, τ, the correlation coefficient is 0.97. The average different is -0.21 s and it is not statistically different from 0. The coefficient of variation is 27%.

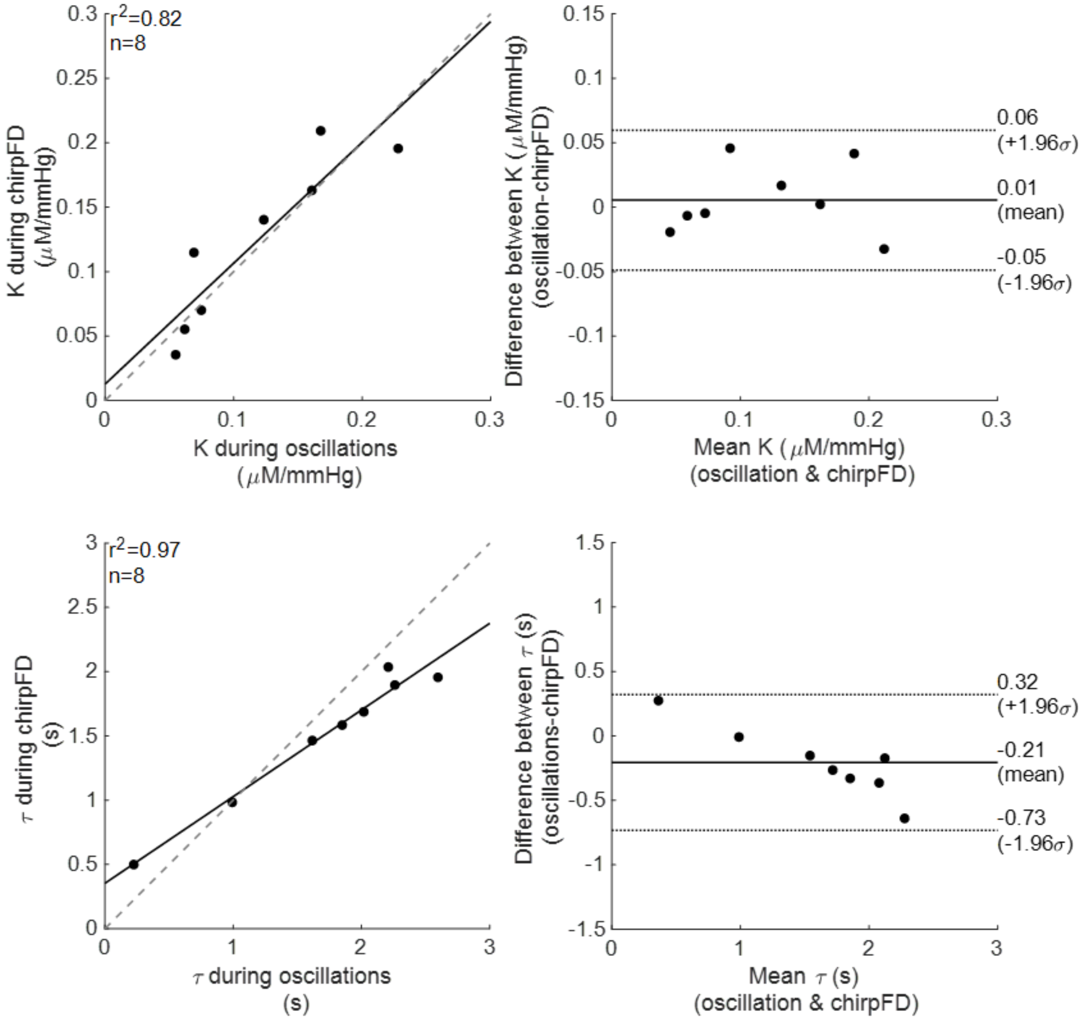

Figure 3.14. Linear plots (left) and Bland-Altman plots (right) to visualize the correlation and agreement between the oscillation protocol and chirp protocol, both analyzed with the frequency domain approach. Dashed lines on the left indicate a slope 1 and solid lines indicate the actual linear fit to the data points (black circles). Dashed lines on the right indicate the 95% confidence interval for agreement. The solid lines indicate the average difference between the parameters while the points indicate the difference between each pair of parameters.

A comparison of the estimated transfer functions from the FD approach of analyzing the full time traces and the TD approach for analyzing the segmented chirp-like time traces is shown in Figure 3.15. The shaded regions indicate the confidence bounds for three standard deviations. Amplitude estimated from the FD analysis is slightly larger than from the TD analysis. The phase difference estimated from each approach are close to overlapping. We refer to the blue circles and green diamonds of Figure 3.12 for the quantitative comparison of the parameters obtained from each of these approaches.

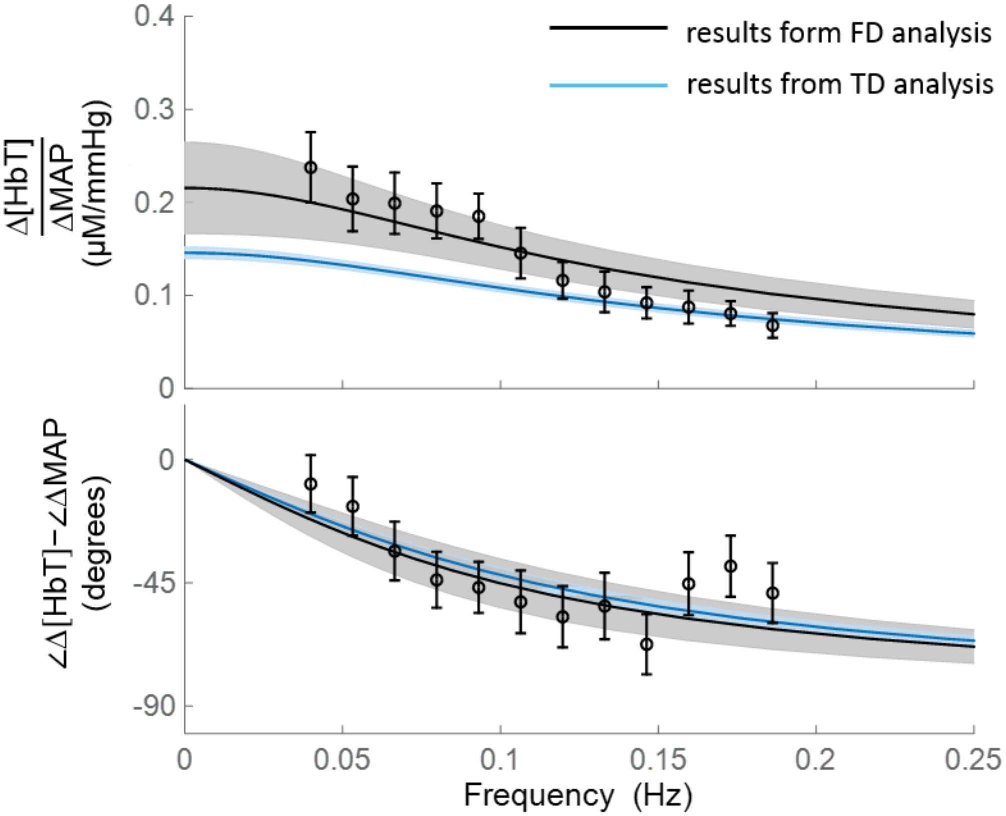

Figure 3.15. Transfer function (black line) estimated from the frequency domain (FD) approach of analyzing the full length of the data and the points that were estimated from the short time Fourier transform (STFT) approach for subject 5. Also, transfer function (light blue line) estimated from the time domain (TD) approach applied only to the segmented chirp-like section of the experiment protocol.

3.4 Discussion

We have applied an STFT approach for coherence, amplitude, and phase analysis between non-stationary MAP and cerebral total hemoglobin concentration. Previously, we have used the Hilbert transform approach for a similar analysis [33], [36]. The benefit of the STFT approach is that we do not need to perform band pass filtering at specific frequencies, which is a time consuming process. Instead, we may consider the entire duration of the experiment and use coherence thresholding to detect not only induced cerebral oscillations but also oscillations that are spontaneous. Analysis of coherence and phase in the time-frequency domain has been used in several studies for analyzing systemic and localized signals of the vasculature [82]–[86]. A review by Addison focuses on NIRS based studies of autoregulation that have used the wavelet approach for time-frequency analysis [87].

Often, a coherence threshold is arbitrarily selected as 0.5. Sassaroli et al has discussed more robust methods for selecting a coherence threshold for CHS studies which are based on surrogate data [79]. Furthermore, incorporating additional information about the expected structure of the measured signals in the time-frequency domain enables opportunities for noise removal [88], [89]. For example, the sliding window and cluster size threshold further reduced noise from the coherence images.

Our results indicate that total hemoglobin concentration in the cerebral microvasculature lags changes in systemic arterial blood pressure at frequencies between 0.04 Hz and 0.20 Hz. The time constant of the fitted low pass transfer function, considering the entire experiment duration, across all 22 subjects was 1.75 ± 0.9 s. We may translate the computed phase delays to time delays. For example, at the frequency 0.106 Hz, the phase difference between $\angle[\mathrm{HbT}]$ and $\angle\mathrm{MAP}$ is -48°. This is translated to a time delay of -1.26 s $\left(\frac{-48^{\circ}}{360^{\circ}\times 0.106\ \mathrm{Hz}}\right)$. The propagation time of arterial pressure waves from the macrovasculature to the microvasculature is on the order of tens to hundreds of microseconds [90], [91], indicating that its contribution to our computed time delay is negligible. The time constant we observe may instead be due to the transit time of blood through the microvasculature. The arteriovenous transit time (AVTT) from a branch of the MCA to a draining vein in the cortical region has been computed in mice using videomicroscopy and different tracers [92]. AVTT values ranges from 0.35 to 1.18 seconds which is within the same order of magnitude as the time delay we observed. In the model of coherent hemodynamics spectroscopy (CHS), we set a range of capillary transit times between 0.4 to 1.4 seconds based on the expected saturation of blood when it reaches the venous compartment [47]. The venous transit time may be on the order of 8 seconds depending on the tissue volume that NIRS probes. In a study of healthy humans, CBFV changes in the straight sinus vein and middle cerebral artery were concurrently recorded in response to a large and rapid decrease in systemic arterial blood pressure [93]. The interval of time before autoregulatory action of the artery was 0.95 seconds and the time was 2.6 for the vein. The difference between these timings is 1.65 seconds possibly indicating the delay for effects of autoregulation to travel to the venous compartment. Our results, showing a time delay between volume and MAP on the order of seconds, give us reason to believe that the oscillations of [HbT] we observe in the low frequency range are due to delayed effects of CBF flow oscillations after they have propagated to the venous compartment.

The estimated gain parameter (0.12 ± 0.05 μM/mmHg) is dependent on the relative contributions of the arterial and venous compartments to our blood volume measurements. The contribution of each compartment during hemodynamic changes is an area of active research [94]–[96]. The arterioles modulate their diameter to regulate blood flow while venules are thought to passively change in volume. However, the arterial compartment contributes less to overall blood volume (~30 % [97]) and venules are much more compliant [98] which means their contributions to overall volume changes may still be significant as they dilate in response to autoregulation controlled changes. In fact, the gain parameter may be a combination of the response of CBF amplitude changes to MAP amplitude changes as well as the response of [HbT] changes in the venous compartment to CBF changes. A dominant contribution of the venous compartment due to its high compliance would be consistent with our hypothesis that the time delay we have observed is due to the venous compartment which, relative to the arterial compartment, is delayed in its response to hemodynamic changes.

Another parameter that may affect the phase delay is the time constant for CA. CA can be modeled as a high pass filter, because it attenuates slow changes in CBF but passes through fast changes in CBF such as those at the frequency of the heart rate. A higher cutoff frequency for the filter indicates a more efficient autoregulation, because it can attenuate CBF over a wider range of frequencies. Kainerstorfer et al [35] translated the results of Aaslid et al [13] to compute an RC high-pass cutoff frequency for CA between 0.03 to 0.06 Hz, dependent upon arterial CO_2 concentration. Fraser et al found similar values for the cutoff frequency of autoregulation with a range between 0.025 to 0.036 Hz [99]. By translating the cutoff frequency with the equation $f_c = \frac{1}{2\pi\tau}$ and selecting a typical value for f_c of 0.03 Hz, we find that the time constant is ~5 seconds. This time constant would directly affect the phase delay between CBF and MAP. The contribution of the time constant to the phase delay between CBV and MAP would depend on the interplay between CBF and CBV.

We compare the relative phase difference we found to results from other studies. Our results agree with those of [32], [75] described in the introduction in which MAP was found to lead [HbO]. In a different study, it was found that oscillations in [HbO] occurred before those in MAP at the frequencies with highest wavelet coherence [100]. These results are in opposition to ours, and we note the large variability of the estimated phase in [100] as a possible reason for the discrepancy. Payne et al presented model simulations of the transfer functions between [HbO] vs ABP and [Hb] vs ABP [101]. The model consisted of the arterial, capillary, and venous compartments, in which the arterial and venous comparts behaved like balloon models, and it also incorporated equations for oxygen transport based on the concentrations of oxyhemoglobin and deoxyhemoglobin. Their model indicated that the ratio of arterial to venous blood volume has a strong influence on phase dynamics. The frequency domain transfer function of [HbO] and ABP, which they simulated with nominal parameters, exhibits the low pass filter relationship that we have found with our experimental data. Payne et al compared their results to those of Reinhard et al [32] , who presented the phase delays at 0.1 Hz, because experimental data for phase delays at multiple frequencies was not available at that time. Payne found an agreement with Reinhard's results. Quick et al has also studied the frequency-dependent relationship between volume, derived from CBF, and pressure, and similarly found a low-pass relationship [102], [103].

While we have focused on a low frequency range, our results have interesting implications for oscillations at the frequency of the heart rate. If we consider that the relative amplitude and phase between cerebral blood volume and MAP are mostly unaffected by effects of CA and blood transit time, their relative amplitude is indicative of arterial vessel compliance, because this is the compartment where arterial blood pressure strongly oscillates. Baker et al studied arterial vessel compliance in the microvasculature with DCS [104]. We translate the compliance values they found to the units we are interested in and found that arterial compliance ranges between 0.0048 to 0.0182 µM/mmHg considering one standard deviation. We computed the amplitude ratio of cerebral blood volume to MAP at the heart rate (data not shown) and found a value of 0.01 ± 0.02 µM/mmHg. The results we found not only depend on the compliance of the vessels but also on the blood vessel density, the local tissue stiffness, relative contributions of large and small vessels as well as anatomical features. We found a range for the phase between [HbT] and ABP at the heart rate between -30 to 30^o (data not shown). Deviations from the expected 0^o phase difference could be explained by small time-delayed contributions of blood flow oscillations in the venous compartment.

We have offered explanations for the relationship we found for ΔMAP and Δ[HbT] in terms of transit time in the microvasculature, cerebral autoregulation, and compartmental compliances. The frequency range under analysis may have an impact on the relative importance of each of these factors. For example, in a study by Zhang et al, the contribution of steady-state resistance and vascular compliance vs active dynamic autoregulation were found to depend on the frequency range of interest [105]. Several other factors may also contribute to transfer functions between these two signals: the concentration of arterial blood gases such as carbon dioxide [106]–[108]; cerebral spinal fluid and global compartment compliance [5], [109]; the effects of the arterial compartment on the venous compartment [98]; properties of absolute arterial pressure (baseline value, direction of change, rate of change) [110]; baroreceptor sensitivity [5]. In addition, factors such as disorders of the carotids or other large arteries [111], [112], low global cerebral oxygen metabolism [113], and altered arterial compliance [114] may affect the transfer functions between ΔMAP and Δ[HbT].

The spatial variability characterized in the 8 subjects in this study can serve as a control for future studies analyzing the spatial volume and pressure relationship in brain injured patients. A NIRS spatial mapping approach has already shown utility in observing hemispheric difference in patients with unilateral carotid disease [115]. In that study, the phase between oxyhemoglobin and ABP was computed for oscillations at 0.1 Hz. They used a cutoff phase of -50°, where a phase less than -50° between oxyhemoglobin and ABP was considered unhealthy while a phase greater than this cutoff was considered healthy. The phase differences they found between oxyhemoglobin and ABP should be similar to what we found between total hemoglobin and MAP because oxyhemoglobin is the dominant contributor to total hemoglobin. The group average phase difference between Δ[HbT] and ΔMAP in our study was -48° ±4°. This average phase difference is within the healthy range considered by [115] although close to the cutoff. We note that our study considered oscillations induced by thigh cuffs as well as spontaneous oscillations while [115] used paced breathing oscillations.

We used a source-detector distance of 3.5 cm for our measurements, because it is well-established that this distance has sensitivity to the top of the cerebral cortex. However, the nature of NIRS means that these measurements were also sensitive to the extracerebral layer. A two layer model that separates oscillatory contributions to optical signals from the cerebral and extracerebral layer has potential for us to improve our sensitivity to only the cerebral layer [116].

The addition of the microcontroller to the air regulator has created opportunities for unique pneumatic cuff protocols. Figure 3.12, bottom panel, shows that the chirp-like protocol for the thigh cuffs can cover the same number of frequencies in less time than the spaced oscillation approach we have used in the past. Of particular interest was a comparison between the spaced oscillations and the chirp-like signals shown in Figure 3.14. Both parameters have a high correlation coefficient and do not have a difference statistically different from 0. However, the comparison contains a small number of points. Differences may arise between the standard oscillatory protocol and the chirp, because less oscillations were in each frequency for the chirp, meaning less time for the body to reach a steady state. Our initial results indicate a strong potential for faster experimental protocols.

3.5 Conclusion

We have characterized the frequency-dependent relationship between the cerebral concentration of total hemoglobin and MAP. The relationship can be modeled as a low-pass filter whose shape is possibly dictated by contributions from the effects of microvascular transit time, cerebral autoregulation dynamics, and compliances of the arterial and venous compartments. NIRS-CHS offers potential monitoring applications with its capability to measure both localized cerebral blood volume and blood flow. The interaction of volume and flow may be used as a localized characterization of cerebral vascular health.

Chapter 4: Coherent hemodynamics spectroscopy in the neurocritical care unit

4.1 Introduction

In this chapter, we illustrate the full pipeline of NIRS-CHS- from creating spectra of [HbO] vs [Hb] and [HbT] vs MAP to computing absolute cerebral blood flow. We use data from a feasibility study in a neurocritical care unit (NCCU) . As described in Chapter 1, both autoregulation and cerebral blood flow can be affected by cerebral injury and by a number of brain pathologies.

The underlying principle of coherent hemodynamics spectroscopy (CHS) is that [HbO] and [Hb] are coherent with a physiologic driving force such as MAP. MAP can induce oscillations of cerebral blood volume and cerebral blood flow and is used for characterizing cerebral autoregulation. Previously cerebral blood volume has been used as a surrogate for MAP in the hemodynamic model. The model equations are modified in this chapter to include MAP directly.

4.2 Methods

4.2.1 Data collection

For a summary of all subjects in the study, see Table A3 in the Appendix. We describe our methods and results for a 67 year old male patient with intraventricular hemorrhage. During measurement, he was not under sedation. His heart rate was 1.34±0.10 Hz and his average mean arterial pressure (MAP) was 100 mmHg . His spontaneous respiratory rate was 0.41±0.05 Hz. His score on the Glasgow coma scale (GCS) was 13 during measurements and was 15 upon release from the NCCU. A diagram of the experimental setup is shown in Figure 4.1. A frequency-domain NIRS system (OxiplexTS, ISS Inc., Champaign, IL) was connected to an optical probe with source-detector distances of 2.0, 2.5, 3.0, and 3.5 cm. The optical probe was placed on the right side of the forehead and held in place with a black athletic headband. A beat-to-beat finger plethysmography system (NIBP100D, BIOPAC Systems, Inc., Goleta, CA) was used to continuously and noninvasively measure the arterial blood pressure. Two pneumatic cuffs were wrapped around the patient’s thighs and periodically inflated to a super-systolic pressure of 150 mmHg to induce controlled changes to the patient’s arterial blood pressure (E-20 Rapid Cuff Inflation System, D.E. Hokanson, Inc., Bellevue, WA). The patient’s systolic blood pressure at the time of measurement was about 100 mmHg, so that a maximum thigh cuff pressure of 150 mmHg was effective for inducing arterial occlusions in the lower limbs. A manometer (Series 626 Pressure Transmitter, Dwyer Instruments, Inc., Michigan City, IN) was connected to one of the thigh cuff chambers in order to record the timing of inflation and deflation of the thigh cuffs. The experimental protocol was as follows: 5 minutes of baseline measurement, 5 cyclic inflation/deflation of the thigh cuffs at 5 different frequencies (0.046, 0.056, 0.063, 0.071, 0.083 Hz) for 2 minutes each, 3 repetitions of 2 minutes of sustained thigh cuff inflations followed by rapid releases, and 5 minutes of recovery measurement. Changes in [HbO], [Hb], and [HbT] were measured in response to the arterial blood pressure perturbations induced by the thigh cuffs using the modified Beer-Lambert law for the 3.5 cm source-detector channel. Time traces of the data for the experiment are shown in Figure 4.2. The baseline (average values during the first minute of experiment) absolute values of oxyhemoglobin, deoxyhemoglobin, and total hemoglobin (determined with the multi-distance approach [27]) were 21 μM, 11 μM, and 32 μM, respectively.

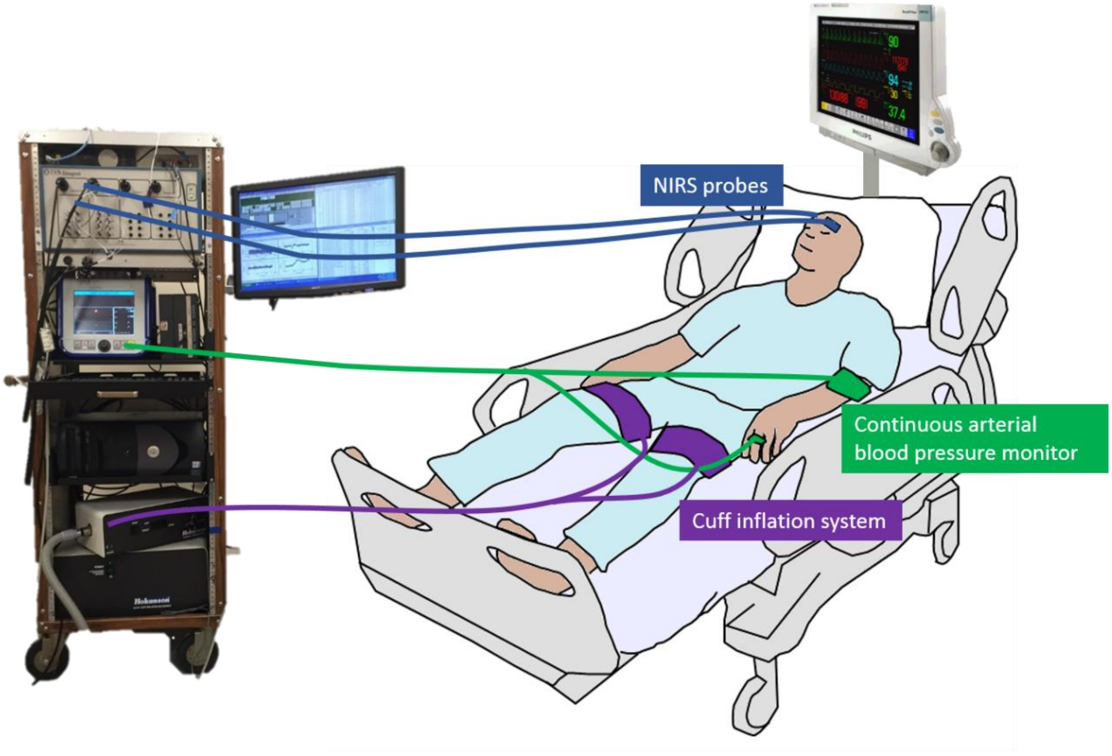

Figure 4.1. Experimental set up in the neurocritical care unit.

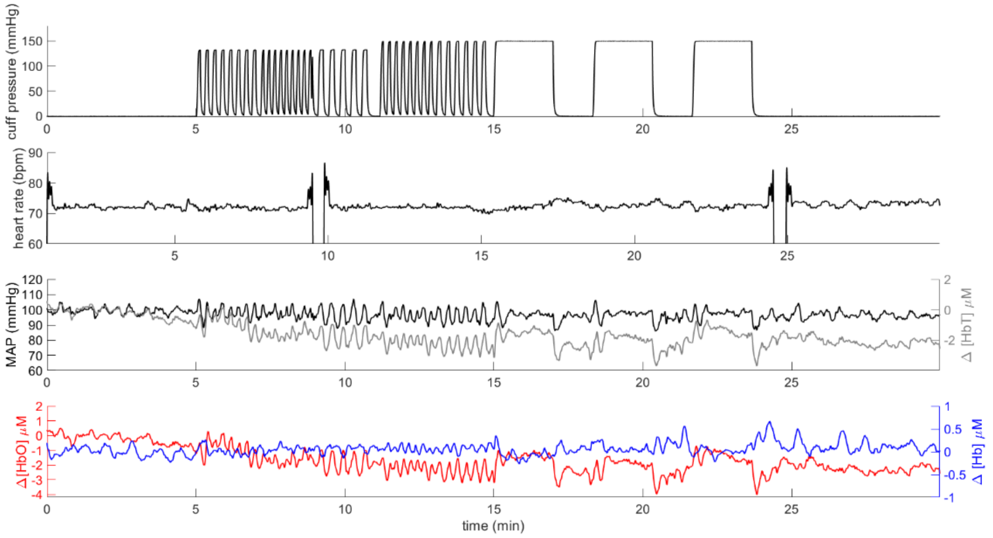

Figure 4.2.Time traces of data collected during experiment. Panel 1: cuff signal from manometer. Panel 2: Heart rate (with some motion artifacts). Panel 3: MAP (black line) and Δ[HbT] (gray line). Panel 4: Δ[HbO] (red line) and Δ[Hb] (blue line).

4.2.2 Data analysis

Following data collection, transfer function analysis was performed between Δ[HbT] and MAP with the techniques described in Sections 3.2.3 and 3.2.4 . The flow chart for this approach is shown on the right branch of Figure 4.3 which indicates how this portion of the analysis (first shown in Figure 3.1) interfaces with our analysis of Δ[HbO] and Δ [Hb]. Time-frequency transfer function analysis was then performed between Δ[HbO] and Δ [Hb] (left branch of Figure 4.3). The time averaged transfer function analysis of Equation 3.3 was applied to the transfer function between Δ[HbO] and Δ[Hb] for the times and frequencies that passed the coherence threshold for Δ[HbT] and MAP. An alternative way to do this would be to separately perform coherence thresholding between Δ[HbO] and MAP and between Δ[Hb] and MAP. Following this, the union between these two groups would designate the pixels to use for the time-averaged transfer function computation. The effects of not using this approach are that the error bars for the transfer function between Δ[HbO] and Δ [Hb] may be larger. However, the fitting procedure is weighted according to the inverse of the error on each point. Therefore, points with relatively large error will have less of an effect on the results of the fit.

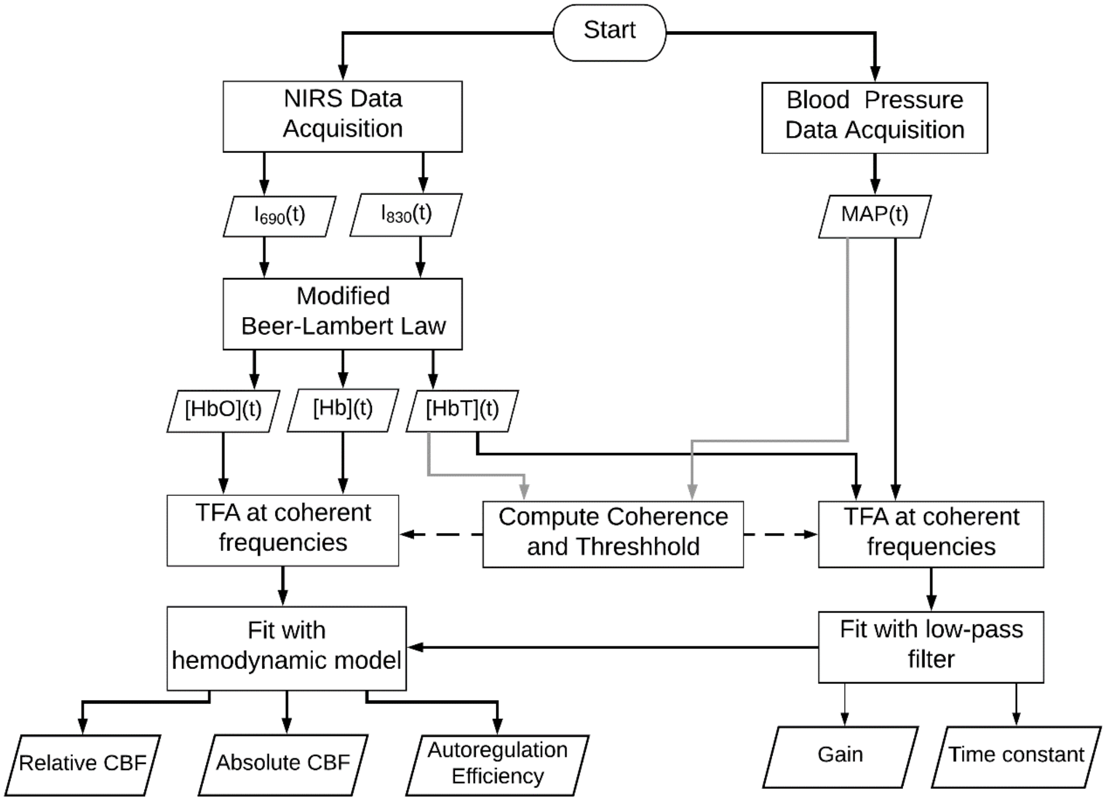

Figure 4.3 Flow chart of data collection and analysis for computing cerebral blood flow and autoregulation.

Following the estimation of the transfer function between Δ[HbO] and Δ [Hb], we fit the transfer function to the hemodynamic model. The equations for the hemodynamic model are modified to include the contribution of MAP to the dynamics of Δ[HbO] and Δ [Hb]. Before showing the model equations, we define the percent changes of cerebral blood volume as

$$\mathrm{cbv} = \Delta[\mathrm{HbT}]/T_0 \tag{4.1}$$

and the percent changes of MAP as

$$\mathrm{map} = (\mathrm{MAP} - \mathrm{MAP}_0)/\mathrm{MAP}_0 \tag{4.2}$$

where T_0 is baseline [HbT] and is MAP_0 is baseline MAP.

The frequency domain description of Δ[HbO] and Δ [Hb], now including mean arterial pressure, are as follows:

$$
\begin{aligned}
\mathbf{O}(\omega) = \mathrm{ctHb}\Big[S^{(a)}\mathrm{CBV}_0^{(a)}a + S^{(v)}\mathrm{CBV}_0^{(v)}v\Big]C_{V/P}(\omega)\mathbf{map}(\omega) + \\
+\mathrm{ctHb}\Bigg[\frac{\langle S^{(c)}\rangle}{S^{(v)}}\big(\langle S^{(c)}\rangle - S^{(v)}\big)\mathrm{F}^{(c)}\mathrm{CBV}_0^{(c)}\mathcal{H}_{RC-LP}^{(c)}(\omega) \\
+ \big(S^{(a)} - S^{(v)}\big)\mathrm{CBV}_0^{(v)}\mathcal{H}_{G-LP}^{(v)}(\omega)\Bigg]k_{F/P}H_{HP}^{(AR)}(\omega)\mathbf{map}(\omega)
\end{aligned}
\tag{4.3}
$$

and

$$
\begin{aligned}
\mathbf{D}(\omega) = \mathrm{ctHb}\Big[\big(1 - S^{(a)}\big)\mathrm{CBV}_0^{(a)}a + \big(1 - S^{(v)}\big)\mathrm{CBV}_0^{(v)}v\Big]C_{V/P}(\omega)\mathbf{map}(\omega) + \\
-\mathrm{ctHb}\Bigg[\frac{\langle S^{(c)}\rangle}{S^{(v)}}\big(\langle S^{(c)}\rangle - S^{(v)}\big)\mathrm{F}^{(c)}\mathrm{CBV}_0^{(c)}\mathcal{H}_{RC-LP}^{(c)}(\omega) \\
+ \big(S^{(a)} - S^{(v)}\big)\mathrm{CBV}_0^{(v)}\mathcal{H}_{G-LP}^{(v)}(\omega)\Bigg]k_{F/P}H_{HP}^{(AR)}(\omega)\mathbf{map}(\omega)
\end{aligned}
\tag{4.4}
$$

where $\mathbf{map}(\omega)$ is the phasor for percent changes in MAP and $C_{V/P}$ is the transfer function between the cerebral blood volume phasor, $\mathbf{cbv}(\omega)$, and $\mathbf{map}(\omega)$. Specifically,

$$
C_{V/P}(\omega) = \frac{\mathbf{cbv}(\omega)}{\mathbf{map}(\omega)} \tag{4.5}
$$

where $\mathbf{cbv}(\omega)$ is the phasor for percent changes in cerebral blood volume. We may model this with the approach of Equation 3.4 by using percent changes of cerebral blood volume and MAP rather than absolute changes of Δ [HbT] and Δ MAP. The term *a* accounts for differences in the amplitudes of volume oscillations in the arterial and venous compartments, respectively. In this work, we assume the amplitudes are equivalent to each other. Percent changes in cerebral blood flow (cbf) are modeled with the RC high-pass filter applied to map, $H_{HP}^{(AR)}$, and the factor $k_{F/P}$ which describes the amplitude changes of flow relative to the amplitude changes of map.

$$\mathbf{cbf}(\omega) = k_{F/P} H_{HP}^{(AR)}(\omega)\mathbf{map}(\omega) \tag{4.6}$$

Then, dividing Equation 4.4 by Equation 4.3 we obtain:

$$\frac{\mathbf{D}(\omega)}{\mathbf{O}(\omega)} = \frac{\left[\frac{\left(1-S^{(a)}\right)\frac{\mathrm{CBV}_0^{(a)}}{\mathrm{CBV}_0}+\left(1-S^{(v)}\right)\frac{\mathrm{CBV}_0^{(v)}}{\mathrm{CBV}_0}}{\frac{\mathrm{CBV}_0^{(a)}}{\mathrm{CBV}_0}+\frac{\mathrm{CBV}_0^{(v)}}{\mathrm{CBV}_0}}\right] C_{\frac{V}{P}}(\omega) - \left[\frac{\langle S^{(c)}\rangle}{S^{(v)}}\left(\langle S^{(c)}\rangle - S^{(v)}\right)\frac{\mathrm{F}^{(c)}\mathrm{CBV}_0^{(c)}}{\mathrm{CBV}_0}\mathcal{H}_{RC-LP}^{(c)}(\omega) + \left(S^{(a)}-S^{(v)}\right)\frac{\mathrm{CBV}_0^{(v)}}{\mathrm{CBV}_0}\mathcal{H}_{G-LP}^{(v)}(\omega)\right] k_{\frac{F}{P}} H_{HP}^{(AR)}(\omega)}{\left[\frac{S^{(a)}\frac{\mathrm{CBV}_0^{(a)}}{\mathrm{CBV}_0}+S^{(v)}\frac{\mathrm{CBV}_0^{(v)}}{\mathrm{CBV}_0}}{\frac{\mathrm{CBV}_0^{(a)}}{\mathrm{CBV}_0}+\frac{\mathrm{CBV}_0^{(v)}}{\mathrm{CBV}_0}}\right] C_{\frac{V}{P}}(\omega) + \left[\frac{\langle S^{(c)}\rangle}{S^{(v)}}\left(\langle S^{(c)}\rangle - S^{(v)}\right)\frac{\mathrm{F}^{(c)}\mathrm{CBV}_0^{(c)}}{\mathrm{CBV}_0}\mathcal{H}_{RC-LP}^{(c)}(\omega) + \left(S^{(a)}-S^{(v)}\right)\frac{\mathrm{CBV}_0^{(v)}}{\mathrm{CBV}_0}\mathcal{H}_{G-LP}^{(v)}(\omega)\right] k_{\frac{F}{P}} H_{HP}^{(AR)}(\omega)} \tag{4.7}$$

The fitting parameters are $t^{(c)}$, $t^{(v)}$, $\frac{\mathrm{CBV}_0^{(c)}}{\mathrm{CBV}_0}$, $f_c^{(\mathrm{AR})}$, and $k_{F/P}$. The lower and upper bounds for the fitting procedure were: 0.3 and 2 s for $t^{(c)}$, 0.3 and 10 s for $t^{(v)}$, 0.1 and 0.9 for $\frac{\mathrm{CBV}_0^{(c)}}{\mathrm{CBV}_0}$, 0.001 and 1 Hz for $f_c^{(\mathrm{AR})}$, and 0 and 1 for $k_{F/P}$. $C_{V/P}(\omega)$ was set as a low pass filter with gain K and time constant τ computed from the fit to the transfer function between cbv and map. The computed amplitude ratio and phase of $\mathbf{O}(\omega)$ and $\mathbf{D}(\omega)$ were fit to the model using the “fmincon” function in Matlab by using a local solver from multiple start points over the range of parameter values. The minimization algorithm was the sum of squared differences between the model and the measurements normalized by the error on each of the measurements. To compute the error on each parameter, we performed bootstrapping [117]. First, the residuals were computed as the difference between the spectra computed with the model (by the fitted parameters) and the spectra we had computed with the measured data. The spectrum obtained by the model fitting procedure was assumed to be a good representation of the data. The residuals were randomly sampled with replacement and added to the spectra. Fitting was repeated to obtain a new set of parameters. This process was repeated 50 times to obtain a distribution of parameter values.

Once the parameters were computed, they were used to compute relative changes in cerebral blood flow:

$$\mathbf{cbf}(\omega) = \frac{\dfrac{\mathbf{O}(\omega) - \mathbf{D}(\omega)}{T_0} - \left(2S^{(a)} - 1\right)\dfrac{\mathrm{CBV}_0^{(a)}}{\mathrm{CBV}_0}\mathbf{cbv}^{(a)}(\omega) - \left(2S^{(v)} - 1\right)\dfrac{\mathrm{CBV}_0^{(v)}}{\mathrm{CBV}_0}\mathbf{cbv}^{(v)}(\omega)}{2\left[\dfrac{\langle S^{(c)}\rangle}{S^{(v)}}(\langle S^{(c)}\rangle - S^{(v)})\mathrm{F}^{(c)}\dfrac{\mathrm{CBV}_0^{(c)}}{\mathrm{CBV}_0}\mathcal{H}_{\text{RC-LP}}^{(c)}(\omega) + (S^{(a)} - S^{(v)})\dfrac{CBV_0^{(v)}}{CBV_0}\mathcal{H}_{\text{G-LP}}^{(v)}(\omega)\right]} \tag{4.8}$$

Equation 4.8 is derived by rearranging Equation 1.6 and Equation 1.7 [47]. The division of these two terms in the frequency domain is equivalent to performing a deconvolution in the time domain. A challenge with the implementation of this approach is that if the denominator is very small for any frequencies, noise in the numerator with be amplified at those frequencies. We have applied Tikhonov regularization to the equation which works as follows. For the frequency domain equation,

$$X(f) = \frac{N(f)}{D(f)}$$

division by a very small number can be avoided by modifying the denominator. The constant value λ is added to *D(f)* so that at frequencies where *D(f)* is small, it is not close enough to zero to greatly amplify noise in *N(f)*. The *N(f)* and *D(f)* are also each multiplied by the complex conjugate of *D(f)* so that we work with the absolute values of *D(f)*.

$$X(f) = \frac{D^*(f)N(f)'}{D^*(f)D(f) + \lambda}$$

We selected to add $\lambda = 0.05$ to the denominator of Equation 4.8 which was heuristically selected, because it reduced noise in $\mathbf{cbf}(\omega)$ without significantly modifying its shape. Following this, the time trace cbf(t) is obtained by applying the inverse Fourier transform to $\mathbf{cbf}(\omega)$. Absolute CBF is obtained by scaling these resulting by absolute CBF_0, which was computed via Equation 1.9.

$$\mathrm{CBF}(t) = \mathrm{CBF}_0(1 + \mathrm{cbf}(t)) \tag{4.9}$$

4.3 Results

The time-frequency coherence maps, computed with a sliding short time Fourier transform are shown in Figure 4.4. The timing of each induced frequency is indicated with the left and right edges of the red boxes. The center of each red box indicates the induced frequency while the upper and lower edges mark the frequency resolution. We observe an enhanced coherence in all four panels of Figure 4.4. Figure 4.4d contains the coherence map that was used for coherence thresholding. The results of the coherence thresholding are shown in Figure 4.5(a). After applying size thresholding for groups of pixels, the binary coherence map is Figure 4.5(b).

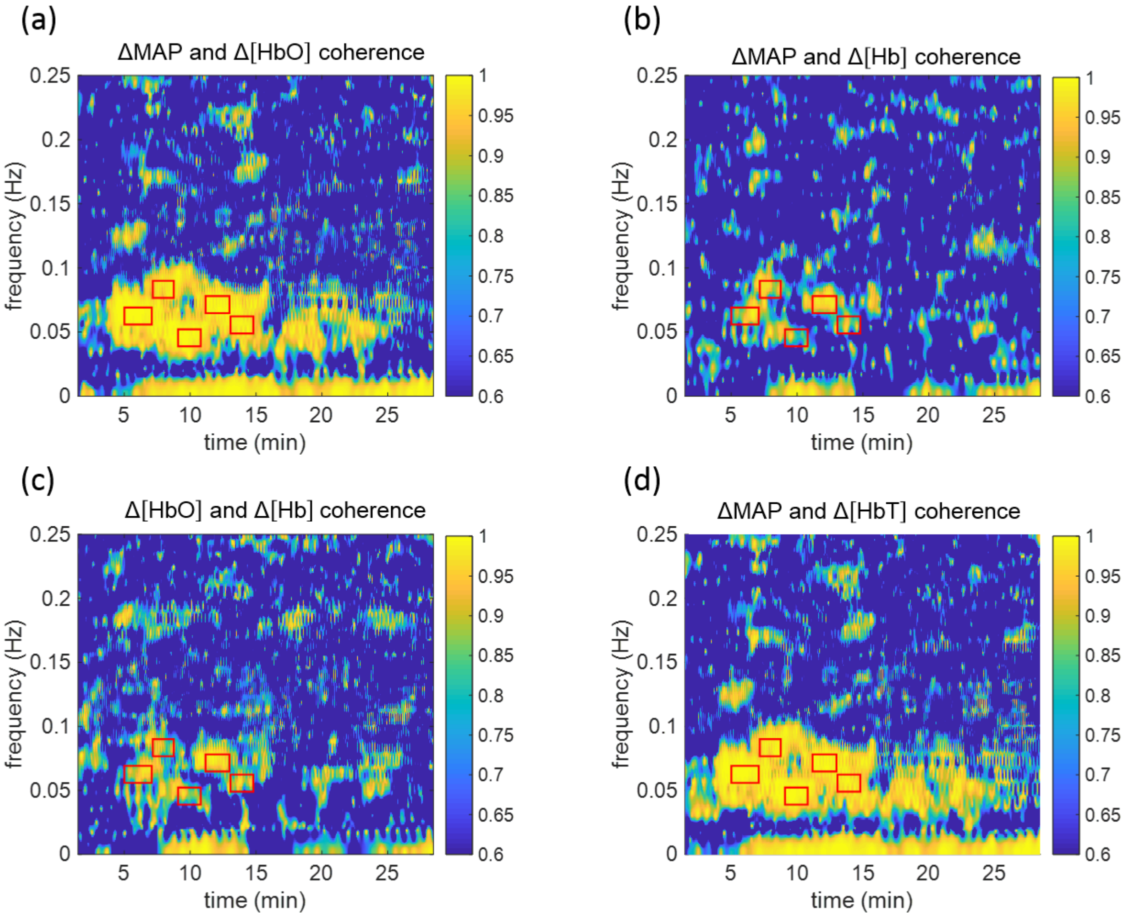

Figure 4.4. Coherence maps. (a) ΔMAP and Δ[HbO] coherence. (b) ΔMAP and Δ[Hb] coherence. (c) Δ[HbO] and Δ[Hb] coherence. (d) ΔMAP and Δ[HbT] coherence.

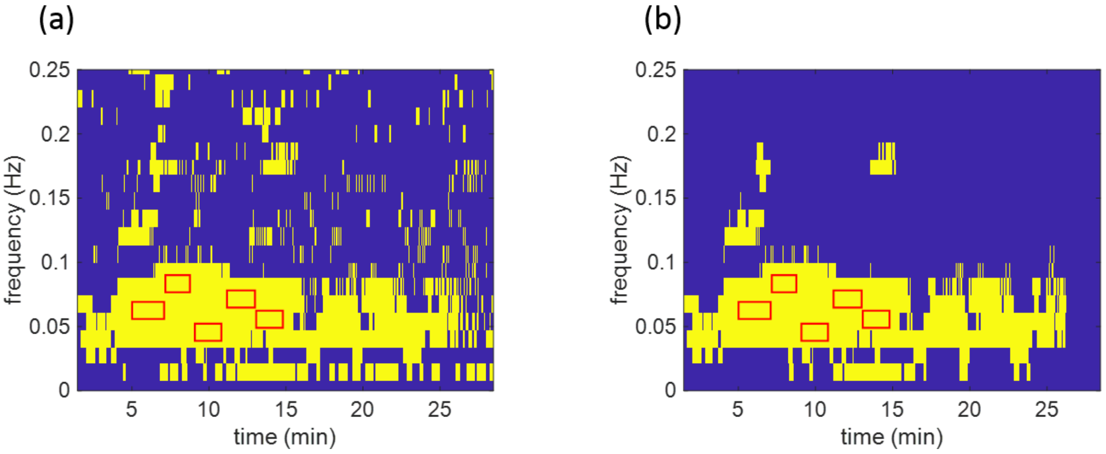

Figure 4.5. Binary coherence between ΔMAP and Δ[HbT] over time and frequency where yellow is coherent and blue is not coherent. Red boxes indicate timing and frequency of oscillations induced with the pneumatic thigh cuffs. Left panel: Binary image of pixels that passed the coherence threshold. Right panel: Binary image of pixels

that passed the coherence threshold and then the cluster size threshold followed by clean up of protuding pixels.

The time-frequency transfer function between Δ[HbO] and Δ[Hb] is shown in Figure 4.6. The pixels that did not pass the coherence threshold are colored dark blue for both panels.

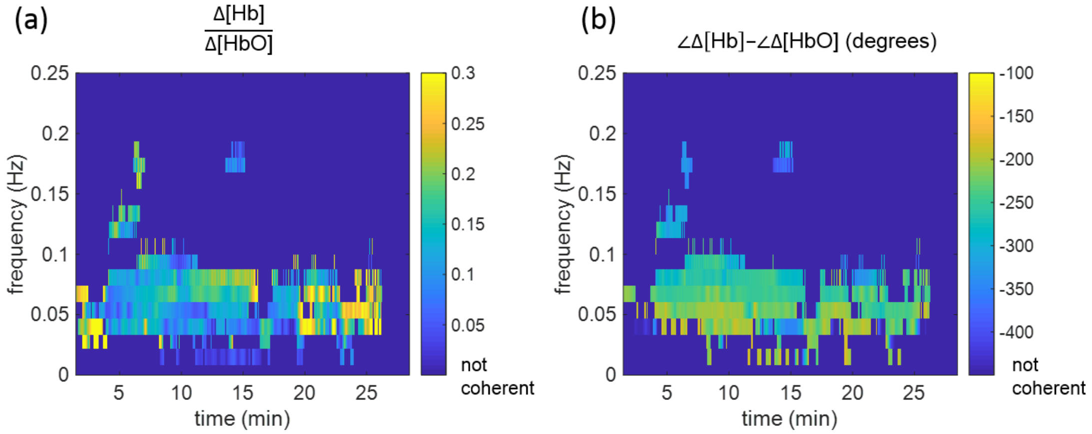

Figure 4.6. Transfer function analysis between Δ[HbO] and Δ[Hb].(a) Amplitude ratio, between Δ[HbO] and Δ[Hb], at the coherent pixels indicated by Figure 4.5b. (b) Phase difference between Δ[HbO], and Δ[Hb] at the coherent pixels. Regions of the images which are dark blue did not pass the coherence thresholding.

The time-frequency transfer function between Δ[HbT] and ΔMAP is shown in Figure 4.7. The pixels that did not pass the coherence threshold are colored dark blue for both panels.

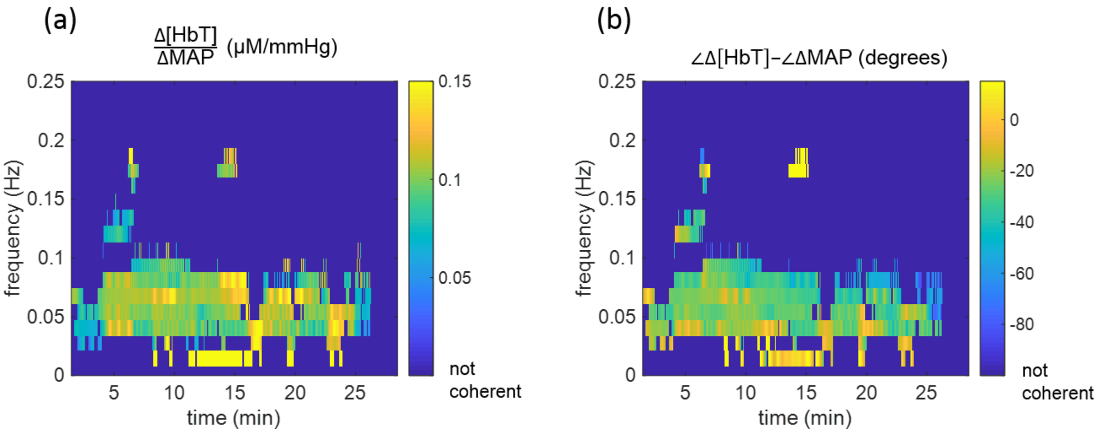

Figure 4.7. Transfer function analysis between Δ[HbT] and ΔMAP. (a) Amplitude ratio, between Δ[HbT] and ΔMAP, at the coherent pixels indicated by Figure 4.5b. (b) Phase difference between Δ[HbT] and ΔMAP at the coherent pixels. Regions of the images which are dark blue did not pass the coherence thresholding.

Figure 4.8 shows the estimated amplitude and phase for the transfer function between Δ[HbT] and ΔMAP with the black circles and error bars. The parameters found from fitting to the spectra with the low pass filter of Equation 3.4 were K = 0.11 ± 0.02 μM/mmHg and τ = 1.34 ± 0.22 s. These results are within the range of values we found for the healthy subjects in Chapter 3. The low-pass filter defined by these parameters if plotted in Figure 4.8 as a solid black line.

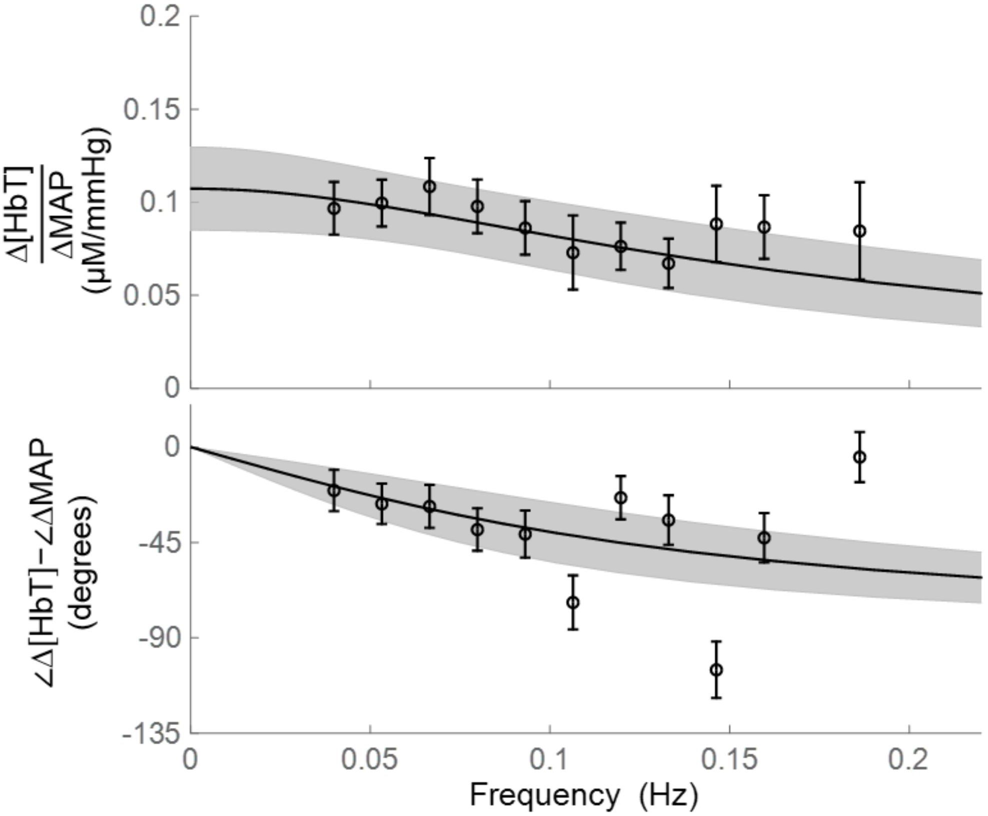

Figure 4.8 The fitted transfer function and points for ΔMAP and Δ[HbT]. Symbols are the average values and error bars are the standard error of the mean. The line is the best fit computed for the low-pass filter model. The gray shaded region indicates the confidence bounds for 3 standard deviations.

The spectra for cbv and map are shown in Figure 4.9. The spectra, of course, have the same shape as the spectra in Figure 4.8, however the amplitudes of MAP and [HbT] have been shifted and scaled by their respective baseline values. The fit of Equation 3.4 to these spectra resulted in the parameters K = 0.34 ± 0.02 and $\tau = 1.34 \pm 0.22$ s. The low-pass filter defined by these parameters if plotted in Figure 4.9 as a solid black line.

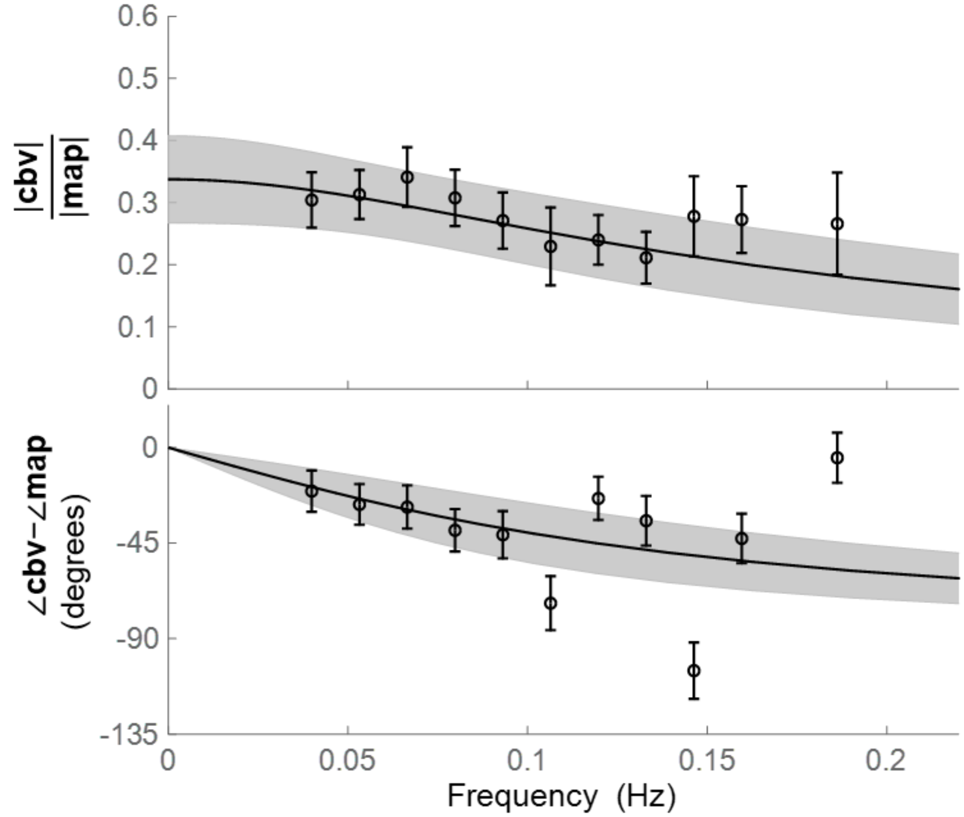

Figure 4.9 The fitted transfer function and points for map and cbv. Symbols are the average values and error bars are the standard error of the mean. The line is the best fit computed for the low-pass filter model. The gray shaded region indicates the confidence bounds for 3 standard deviations.

The points computed from the transfer function estimation for Δ[HbO] and Δ[Hb] are shown as black circles in Figure 4.10.The fitting to the hemodynamic model produced the following parameters: $t^{(c)}$=0.30 ± 0.67 s, $t^{(v)}$= 5.21 ± 0.75 s, $\frac{\mathrm{CBV}_0^{(c)}}{\mathrm{CBV}_0}$= 0.26 ± 0.07, $f_c^{(\mathrm{AR})}$= 0.0014 ± 0.0008 Hz, $k_{F/P}$= 0.19 ± 0.05. The parameters were used to compute an absolute baseline CBF of 56 ml/100g/min. The spectra corresponding to the computed parameters are plotted as black lines in Figure 4.10. The gray lines in Figure

4.10 are the fits obtained from bootstrapping the residuals and provide an indicate for the variability of lines that could describe the points given the size of their errors.

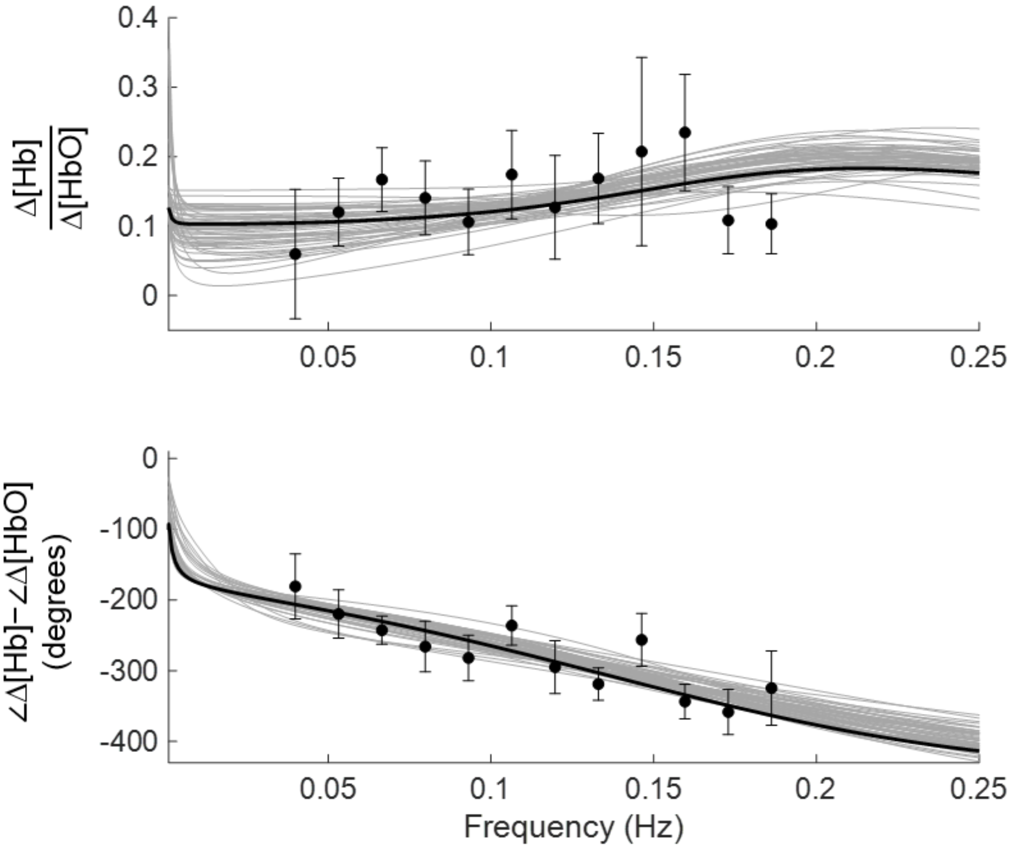

Figure 4.10. The fitted transfer function and points for Δ[HbO] and Δ[Hb]. Symbols are the average values and error bars are the standard error of the mean. The black line is the best fit computed for hemodynamic model. The gray lines indicate all the possible fits obtained from the bootstrapping procedure.

In Figure 4.11, absolute CBF, computed with Equation 4.8 and Equation 4.9, is plotted in the top panel. The bottom panel of Figure 4.11 shows the cerebral perfusion pressure (CPP) which was calculated as the difference between the MAP measured by us and intracranial pressure (ICP) measured invasively with the hospital instrumentation. ICP was close to 0 such that MAP and CPP are similar to each other.

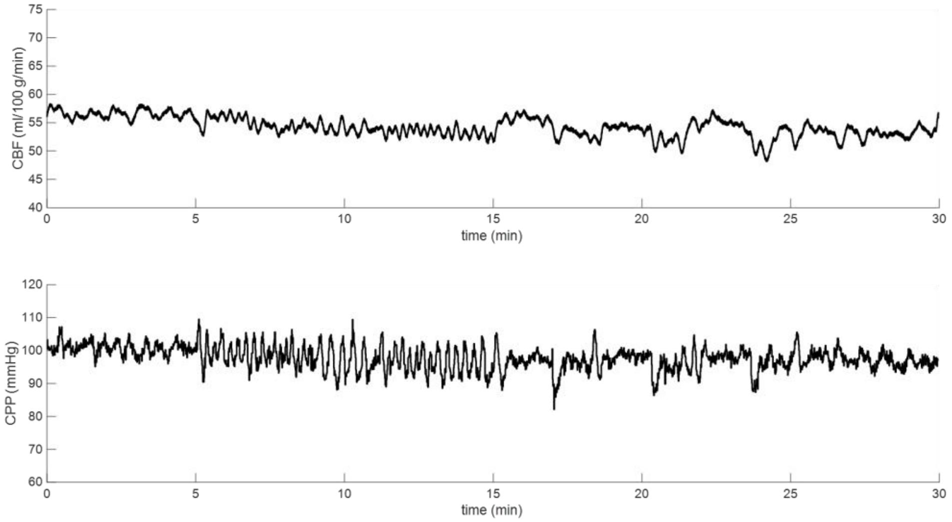

Figure 4.11. Top panel: Time trace of cerebral blood flow (CBF). Bottom panel: Time trace of cerebral perfusion pressure (CPP).

Given CBF and MAP, we compared them in a scatter plot and imposed them on a static autoregulation curve. The scatter plot does not cover a wide enough range of mean arterial pressures to comment on the limits of static autoregulation for this patient. We present Figure 4.12 only to visualize how our computation of CBF could be compared with MAP to analyze static autoregulation in the case that there is a larger range of MAP.

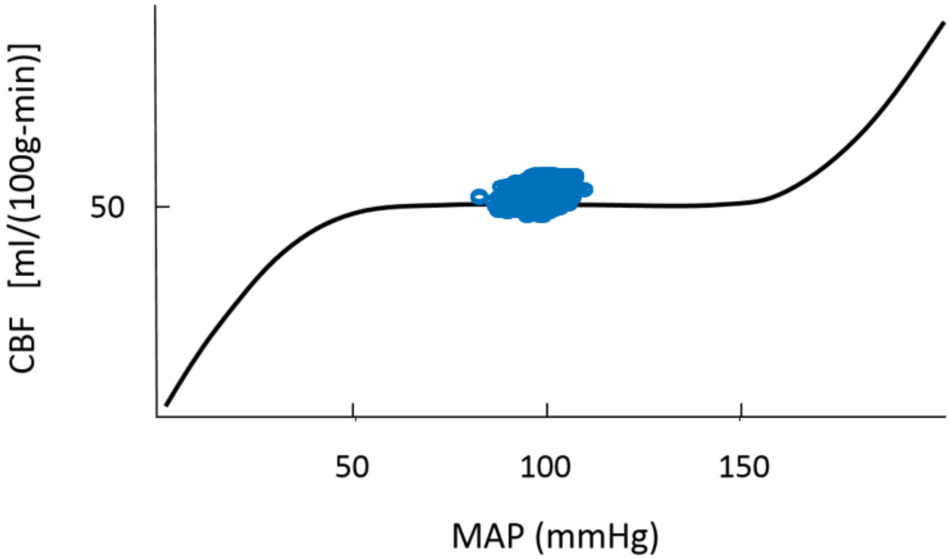

Figure 4.12. A classic static autoregulation curve with points from Figure 4.11 imposed.

4.4 Discussion

The value of 0.0014 Hz for $f_c^{(\mathrm{AR})}$ indicates a low efficiency of autoregulation in the NCCU patient within the cerebral region measured. In healthy subjects, we have found $f_c^{(\mathrm{AR})}$ to be between 0.01 to 0.03 Hz. The absolute CBF of 56 ml/100g/min well within the normal range for CBF. As described earlier, the patient was discharged from the hospital with a Glasgow coma scale value of 15 which is the best possible response.

The value of transit time of the blood in the capillaries determined by the model fit , $t^{(c)}$=0.30 ± 0.67 s, has a very large standard deviation. In future work, we aim to parametrize the low-pass filter relation between Δ[HbT] and Δ[MAP] with parameters from the hemodynamic model rather than the general gain factor, K, and time constant τ we have used up to now. In this way, the variability of the model parameters may be reduced.

An additional challenge with the study was in the low success rate of inducing oscillations in MAP whose effects could be measured by NIRS. The challenge with inducing coherent oscillations in all patients is what drove the transition from the Hilbert transform approach of analyzing the data to the STFT approach with coherence thresholding. This has enabled us to move from fitting to the hemodynamic model with a few points (5 or less) to several points [118]. Also, since the study, we have applied the cuff inflation protocols over a wider range of frequencies and have tested alternative approaches to the protocol such as the chirp-like oscillations in healthy subjects (Chapter 3). The improvement of our techniques for inducing and measuring reliable coherent oscillations is an active area of research.

4.5 Conclusion

In the beginning applications of coherent hemodynamics spectroscopy (CHS), we used a Hilbert transform approach for computing the spectra of oxyhemoglobin and deoxyhemoglobin. We removed noise from the spectra with thresholding based on standard deviations of the computed amplitude ratios and phase differences (as described in Chapter 2). In the work presented here, we have made improvements to the data analysis framework. First, we used a sliding short time Fourier transform (STFT) to efficiently perform transfer function analysis within a frequency range of interest, rather than segmenting the sections of the experiment where cuff oscillations were performed. This has enabled us to detect induced as well as spontaneous oscillations of hemoglobin that are coherent with MAP. Second, the coherence thresholding we have performed, introduced in Chapter 3, is a more robust approach for eliminating noise from the spectra. Third, we have performed a characterization of the relationship between cerebral blood volume and MAP which can be used to inform the updated hemodynamic model. By fitting all these pieces together for NIRS-CHS, we move closer to the goal of a bedside tool for monitoring microvascular cerebral health.

Chapter 5: Future directions

5.1 Responses to carbon dioxide

Carbon dioxide inhalation, mixed with room air or oxygen, is a useful approach for studying the sensitivity of cerebral blood flow measurement techniques. Carbon dioxide (CO_2) is a regulator of vascular tone. Changes in the partial pressure of CO_2 in arterial blood ($PaCO_2$) can induce an increase of CBF during hypercapnia, due to vessel dilation [119], or a decrease of CBF during hypocapnia, due to vasoconstriction [120]. In normal subjects, CBF increases linearly by 2% to 4% /mmHg of $PaCO_2$ within the range of 25 to 75 mmHg [3]. This translates to a change in CBF of about 1-2 ml/100 g/min per 1 mm Hg of $PaCO_2$. CO_2 also has an effect on the efficiency of autoregulation. Aaslid et al showed that, in the case of hypocapnia (~22 mmHg $PaCO_2$), CBFV is faster to recover from a rapid drop in ABP relative to during normocapnia (~37 mmHg $PaCO_2$) . In the case of hypercapnia (~47 mmHg $PaCO_2$) , CBFV is slower to recover from a rapid drop in ABP [13]. Therefore, future work for analysis of the relationship between Δ[HbT] and ΔMAP and for analysis of the hemodynamic model of CHS will include a study in which we characterize the changes we measure in cerebral blood volume, blood flow, and autoregulation efficiency due to changes in end tidal CO_2 in healthy subjects.

In addition to CBF and autoregulation, CO_2 also affects cerebral blood volume and vessel compliance. Grubb et al found that cerebral blood volume increased by 0.041 ml/100g per 1 mmHg of $PaCO_2$ [121]. If we assume a hemoglobin concentration in blood of 2300 micromoles HbT/L blood, we can translate these results to say that total hemoglobin concentration in tissue increases by about 1 μM per 1 mmHg $PaCO_2$. Grub et al also found the following relationship between changes in blood volume and changes in $PaCO_2$, depends on the absolute value of MAP (for MAP between 100 and 170 mmHg):

$$\frac{\Delta \mathrm{CBV}}{\Delta \mathrm{PaCO_2}} \cong 0.006\mathrm{MAP}-0.04$$

Carrera et al studied the effects of hypo- and hypercapnia in healthy subjects by measuring arterial compliance with the use of transcranial Doppler and CBFV measurements [69]. They found a decrease of arterial compliance during hypocapnia and no change to arterial compliance during hypercapnia (relative to normocapnia). These results make sense when we consider the vasoconstriction that occurs during hypocapnia. These relationships have been summarized in Table 4.

Table 4. Expected responses to hypo- and hypercapnia. Up arrow: increase, down arrow: decrease, horizontal line: stay the same. $EtCO_2$ stands for end tidal carbon dioxide.

Condition	cerebral blood flow	capillary transit time	autoregulation efficiency	cerebral blood volume	arterial compliance
Hypocapnia $EtCO_2$: 25-35 mmHg	↓	↑	↑	↓	↓
Hypercapnia $EtCO_2$: 45-60 mmHg	↑	↓	↓	↑	—

To test the sensitivity of the hemodynamic model, we intend to perform a study as follows. Subjects will wear the typical monitoring equipment of our studies (NIRS probes, respiration belt, arterial blood pressure cuffs) while also wearing a capnography system that can measure end tidal CO_2. A hypocapnia portion of the experiment will consist of 2-3 minutes of controlled hyperventilation. A hypercapnia portion of the experiment will consist of breathing 5% CO_2 mixed with room air for 2-3 minutes. During each portion of the experiment, an abbreviated version of the cuff inflation protocol will be performed. We may fit the data of the experiment and relate the end tidal CO_2 to the computed absolute CBF, capillary transit time, and autoregulation efficiency. This will allow us to determine how our measurements, in absolute units, scale with CO_2 changes in comparison to the expected changes that have been well established in the medical literature. Deviations from expected trends will inform improvements to the model going forward. An important assumption for measuring CBF changes with this protocol is that there are no concurrent changes in the cerebral metabolic rate of oxygen ($CMRO_2$), because we would not be able to separate their independent contributions to changes in [HbO] and [Hb]. Chen and Pike determined that there is no significant change in global $CMRO_2$ with hypercapnic and hypocapnic challenges[122].

As described in Chapter 3, we hypothesize that the relationship between Δ[HbT] and ΔMAP are determined by contributions from cerebral autoregulation, microvascular transit time, and vessel compliance. All of these factors are affected during hypercapnia and hypocapnia. We intend to further develop the RC low-pass filter model of Chapter 3 to consider these contributing factors as separate parameters rather than as their lumped effects as they contribute to the gain and single time constant. The experiment described in this section will also enable us to test a more detailed model for Δ[HbT] and ΔMAP. We may then determine if the parameters change in the expected directions as described in Table 4.

5.2 New protocols and spontaneous oscillations

As introduced in Chapter 1, the human body has many naturally occurring hemodynamic oscillations and there are also a variety of protocols for inducing oscillations. Among the protocols are paced breathing [32], thigh cuff inflation and deflation [45], squat-stand maneuvers [31], leg lifts [123], and oscillatory lower body negative pressure [124]. In terms of simplicity of implementation, minimization of motion artifacts, and minimization of active participation by the subject, we have found that the thigh cuff inflation procedure is the most favorable. We found that the protocol involving thigh cuff inflation to a pressure above systolic pressure was well tolerated by all but one of the patients in the neurocritical care unit study. As indicated in Table A3, inducing MAP oscillations and transient changes with thigh cuffs inflation/deflation did not work for all patients. One challenge is the time it takes to collect data at multiple oscillations which is not practical for bedside use in a busy clinical setting. It was challenging for some patients to remain still for a full 30 minutes and shorter measurement times are preferable. We have begun to explore alternative approaches such as the chirp-like protocol described in Chapter 3. Future work may include applying this protocol to more subjects and for multiple times within a day as well as across multiple days in order to test the repeatability of the protocol. It may also be considered as an option for the protocol to use during the CO_2 experiments previously suggested. Another interesting protocol to try is a pseudo-random binary sequence which has been implemented by Katsogridakis et al[125]. In their work, the on and off times of cuff inflation were selected randomly to enhance blood pressure variability. We may explore this approach or randomized approaches similar to it which do not require separately induced oscillations but rather introduce multiple frequencies within a short time span.

While the thigh cuff inflation protocols are relatively simple to implement and typically do not result in subject discomfort, the ideal CHS experiment would rely on spontaneous oscillations of the body for generating spectra. Several groups have studied spontaneously occurring oscillations with NIRS [65]–[67], [75], [84], [85], [126]. Future studies for NIRS-CHS may include comparison of long baseline measurements while the subject lays in a bed or recliner followed by a typical thigh cuff inflation protocol. We may then apply our data analysis techniques to both portions of the experiment and compare them. Our continued study of thresholding techniques for detecting oscillations that are suitable for analysis with the hemodynamic model ([79]) will assist us in investigating the potential of spontaneous oscillations measured during baseline for CHS.

5.3 Association of cerebral blood flow and autoregulation with outcomes in the neurocritical care unit

Cerebral blood flow and autoregulation are often affected in patients in the neurocritical care unit (NCCU)[8]. We intend to apply NIRS-CHS to NCCU patients throughout their hospital stay and correlate the findings for cerebral blood flow and autoregulation to patient recovery and final outcome. Throughout a patient’s stay in the NCCU, multiple NIRS-CHS measurements may be performed to characterize repeatability within one day and changes across time. Patient status in outcome will be quantified with the relevant clinical scale based on their injury. This may include the Glasgow Coma Scale, the Hunt and Hess Scale, and/or the FOUR (Full Outline of Unresponsiveness) score. Intracranial pressure monitoring, cerebral perfusion pressure monitoring, and transcranial Doppler recordings can also be recorded and provide an indication on if NIRS-CHS is providing additional information due to its localized sensitivity to the microvasculature.

5.4 Future outlook

Near-infrared spectroscopy is a promising tool for use in monitoring cerebrovascular diseases and brain injuries. It performs real time monitoring safely and noninvasively. By combining it with coherent hemodynamics spectroscopy, the measurements of oxyhemoglobin and deoxyhemoglobin may be quantitatively related to the underlying changes in cerebral blood flow, cerebral blood volume, and cerebral metabolic rate of oxygen. The pathophysiology of both acute and chronic cerebral diseases is complex, with many factors contributing to cerebral recovery, and is also diverse. Personalized thresholds and treatment regimens are an active area of interest to physicians. NIRS-CHS stands in a good position to assist with development of personalized treatment, because it can safely perform multiple measurements at the hospital bedside. For example, the optimal value of cerebral perfusion pressure (CPP) for hospital patients may vary depending on their level of cerebral autoregulation, with a particular CPP being optimal for enabling cerebral recovery.

Presently, there is not a gold standard for the computation of cerebral autoregulation efficiency, and it is still a growing area of research in the fields of both transcranial Doppler ultrasound and diffuse biomedical optics. NIRS-CHS stands to contribute to the growing body of knowledge about autoregulation due to its sensitivity to the microvasculature and its ability to describe the interplay between flow changes, volume changes, and the efficiency of cerebral autoregulation.

Validation of the parameters NIRS-CHS measures, via CO_2 studies as well as comparisons to other modalities, is critical for the acceptance of the technique. One approach for comparison to other modalities is to compare relative blood flow changes computed with CHS to relative blood flow changes computed with DCS. DCS has been compared to multiple gold standard CBF measurement modalities. The sensitivity of both DCS and NIRS to the arterial, capillary, and venous compartments of the microvasculature would make this a reasonable comparison. Validation of NIRS-CHS for absolute CBF measurements could potentially be done with imaging modalities like positron emission tomography or arterial spin labeling magnetic resonance imaging. With this approach, selecting appropriate tissue volumes for comparison would be a challenge to consider.

Measurements of oscillations in hemoglobin concentrations have been performed for several years in NIRS research. NIRS-CHS makes use of measurements at multiple frequencies of oscillations by relating the phases and amplitudes of oxyhemoglobin and deoxyhemoglobin at these frequencies to the underlying physiologic changes. With our recent work in coherence thresholding and transfer function analysis, we have been able to expand our analysis to not only known frequencies of induced oscillations but also to those that are spontaneously occurring. There are additional new directions that our approach has enabled. For example, in Figure 5.1, we present the coherence between arterial blood pressure and total hemoglobin concentration up to 1.7 Hz for Subject 5 from the study in Chapter 3. In Figure 3.5, we considered only the low frequencies of oscillations. In Figure 5.1, we can see a high level of coherence at frequencies around the heart rate. The oscillations within this frequency range may provide additional information for fitting to the hemodynamic model.

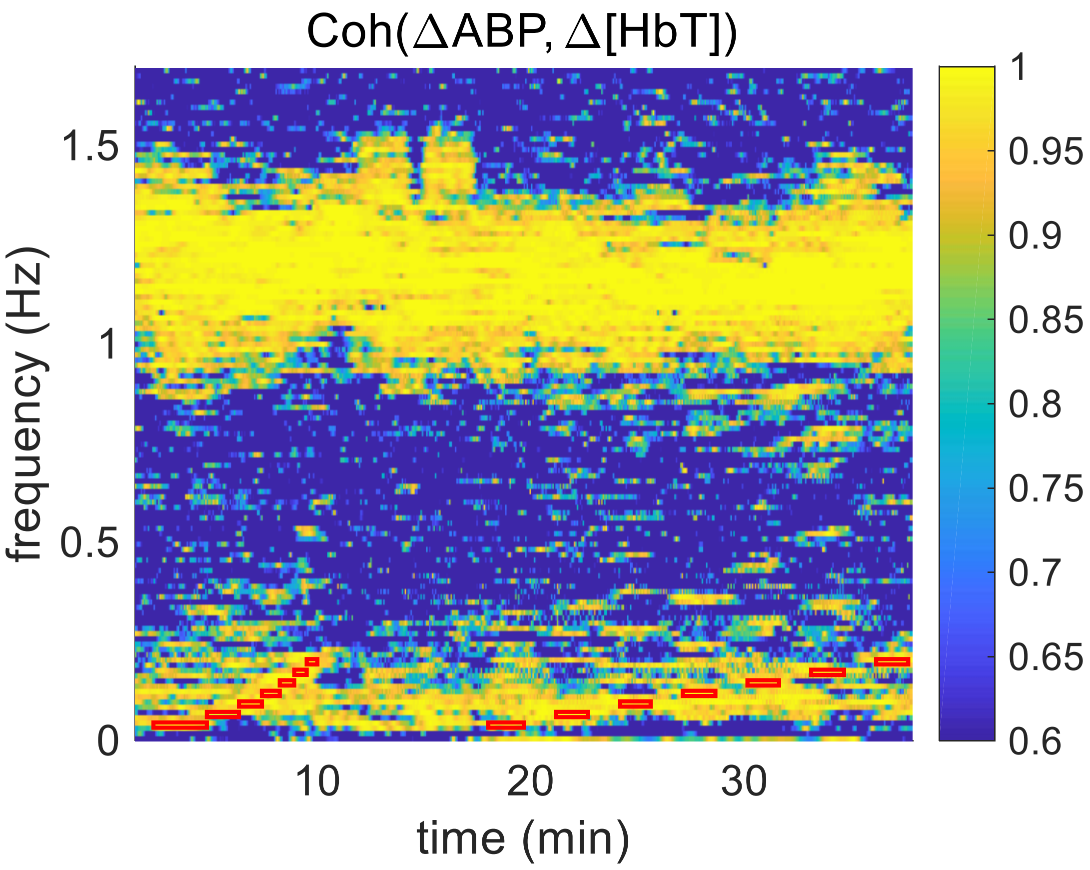

Figure 5.1. Coherence between arterial blood pressure and total hemoglobin concentration for Subject 5 from Chapter 3. The range of the y-axis has been expanded to show up to 1.7 Hz.

Figure 5.2 shows the times and frequencies at which arterial blood pressure and total hemoglobin concentration were coherent with each other, where yellow pixels passed the coherence threshold. From this figure, we observe the pixels outlined by the red boxes which indicate the times and frequencies of the induced thigh cuff oscillations. We also see a broad range of frequencies around the heart rate which passed the coherence threshold.

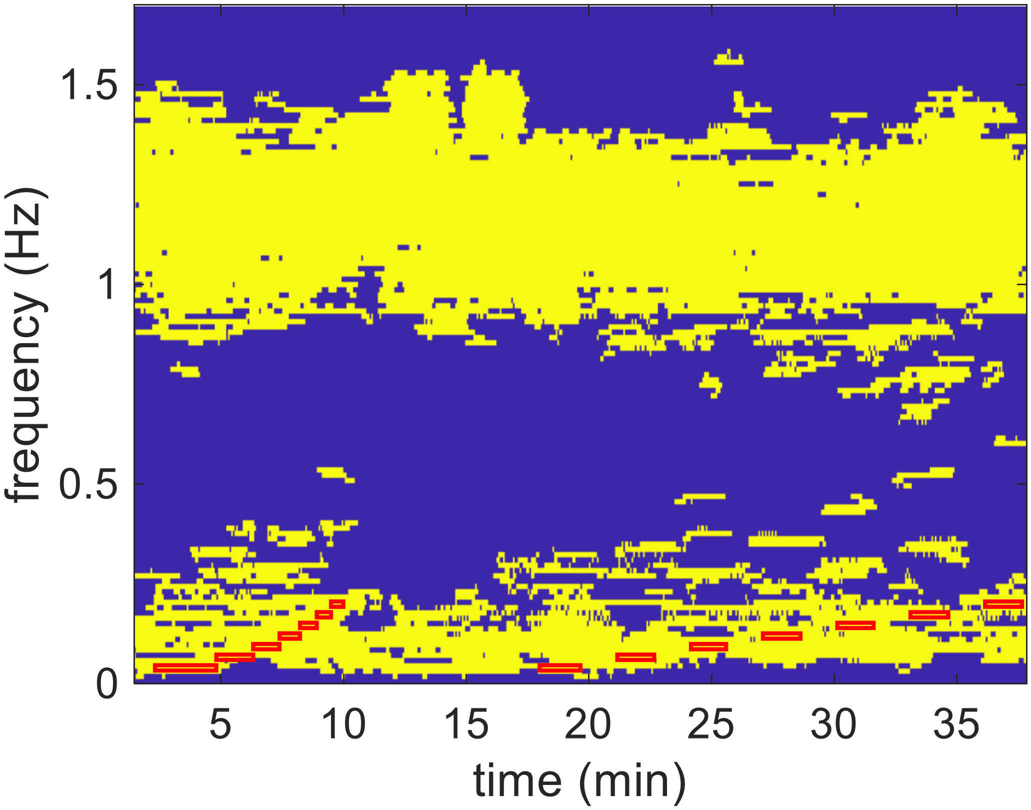

Figure 5.2. Binary coherence between arterial blood pressure and total hemoglobin concentration for Subject 5 of Chapter 3. Yellow pixels passed the coherence threshold and blue pixels did not. Red boxes indicate the time and bandwidth of induced oscillations from thigh cuffs.

Figure 5.3 shows a zoomed in version of Figure 5.2 during the second half of the experiment. From this figure, we see that the thigh cuffs have not only induced coherent oscillations at the intended frequencies (indicated by the red boxes) but also at harmonics of those frequencies. These exciting results indicate the potential of using harmonics in CHS to obtain frequencies for model fitting within the frequency range between the respiratory rate and the heart rate.

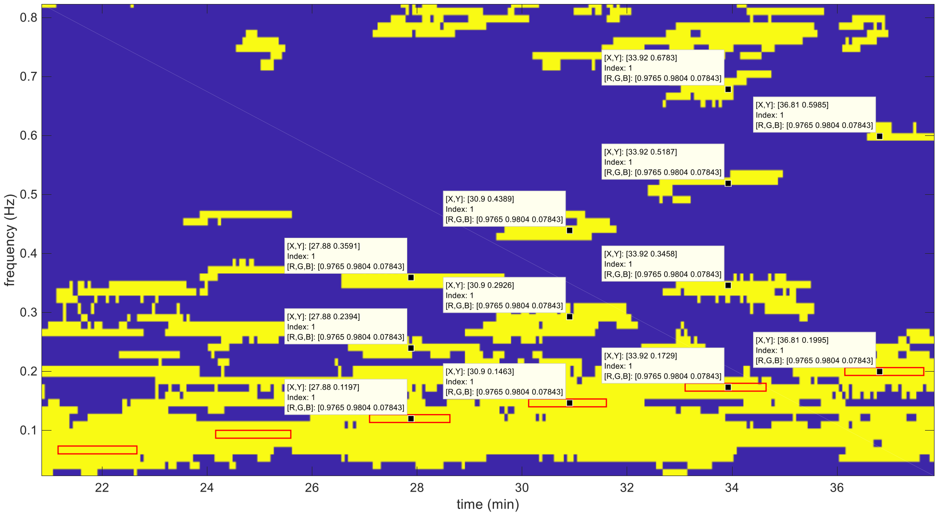

Figure 5.3. Binary coherence between arterial blood pressure and total hemoglobin for Subject 5 of Chapter 3. Induced oscillations are marked with red boxes. Markers in the figure indicate harmonics of the induced oscillations.

The future directions of NIRS-CHS present opportunities for improving fundamental understanding of cerebral health in relation to autoregulation and the interplay between blood pressure, blood volume, and blood flow. Further, NIRS-CHS has potential as a clinical tool for patient cerebral monitoring.

Funding acknowledgements

This research was supported by the National Institutes of Health Grants No. R01-NS095334, R21-EB020347, and R01-CA154774. The neurocritical care unit study was supported by the Neuroscience and Pain Research Unit at Pfizer Inc.

Appendix

A1

Table A.1. Acronyms reported in this work with associated definitions.

Acronym/Symbol	Definition
ABP	arterial blood pressure
BP	blood pressure
CA	cerebral autoregulation
cbf	cerebral blood flow (relative changes)
CBF	cerebral blood flow
CBFv	cerebral blood flow velocity
CHS	coherent hemodynamics spectroscopy
$CMRO_2$	cerebral metabolic rate of oxygen
CPP	cerebral perfusion pressure
CSF	cerebral spinal fluid
CVR	cerebrovascular resistance
DCS	diffuse correlation spectroscopy
FD	frequency domain
GCS	Glasgow coma scale
[Hb]	tissue concentration of deoxyhemoglobin
[HbO]	tissue concentration of oxyhemoglobin
[HbT]	tissue concentration of total hemoglobin
HVx	hemoglobin volume index
ICP	intracranial pressure
MAP	mean arterial pressure
MRI	magnetic resonance imaging
MSC	mean squared coherence
NCCU	neurocritical care unit
NIRS	near-infrared spectroscopy
PET	positron emission tomography
PRx	pressure reactivity index
SAH	subarachnoid hemorrhage
STFT	short time Fourier transform
TBI	traumatic brain injury
TCD	transcranial Doppler
TD	time domain
TFA	transfer function analysis

A2

Table A.2 Summary of subjects. Column 1: subject number, column 2: female or male (F or M), column 3: age, column 4: number of channels/side (right, R or left L), column 5: position (chair with feet on floor or bed with feet parallel to floor), column 6: frequencies of oscillations that had spacing in between, column 7: frequencies of oscillations that had no spacing in between such that they were chirp-like. Data for subjects 13 -21 was taken from the study described in [76].

Subject #	**F/M**	**Age**	**Num. of chan.**	**Position**	**Frequencies spaced with baseline periods (Hz)**	**Frequencies with no spacing (chirp-like) (Hz)**
1	F	27	8	Chair	n/a	0.040, 0.067, 0.093, 0.120, 0.146, 0.173, 0.200
2	M	27	8	Chair	0.040, 0.067, 0.093, 0.120, 0.146	0.040, 0.067, 0.093, 0.120, 0.146, 0.173, 0.200
3	M	27	8	Chair	0.040, 0.067, 0.093, 0.120, 0.146	0.040, 0.067, 0.093, 0.20, 0.146, 0.173, 0.200

4	F	28	8	Bed	0.040, 0.067, 0.093, 0.120, 0.146	0.040, 0.067, 0.093, 0.120, 0.146, 0.173, 0.200
5	M	31	8	Bed	0.040, 0.067, 0.093, 0.120, 0.146, 0.173, 0.200	0.040, 0.067, 0.093, 0.120, 0.146, 0.173, 0.200
6	M	32	8	Bed	0.040, 0.067, 0.093, 0.120, 0.146, 0.173, 0.200	0.040, 0.067, 0.093, 0.120, 0.146, 0.173, 0.200
7	F	26	8	Bed	0.040, 0.067, 0.0932, 0.120, 0.146, 0.173, 0.200	0.040, 0.067, 0.0932, 0.120, 0.146, 0.173, 0.200
8	F	27	8	Chair	0.042, 0.056, 0.069, 0.083, 0.097, 0.111, 0.125	n/a
9	F	33	1 (R)	Chair	0.050,0.063,0.076, 0.090	0.050,0.063,0.076,0.090

10	M	28	1 (R)	Chair	0.040, 0.067, 0.093, 0.120, 0.146, 0.173, 0.200	0.040, 0.067, 0.093, 0.120, 0.146, 0.173, 0.200
11	M	21	1 (R)	Chair	0.040, 0.067, 0.093, 0.120, 0.146, 0.173, 0.200	0.040, 0.067, 0.093, 0.120, 0.146, 0.173, 0.200
12	F	24	1 (R)	Chair	0.040, 0.093, 0.146, 0.200	0.040, 0.067, 0.093, 0.120, 0.146, 0.173, 0.200
13	F	30	1 (L)	Chair	0.063, 0.083, 0.056, 0.071, 0.046	n/a
14	F	25	1 (L)	Chair	0.063, 0.083, 0.056, 0.071, 0.046	n/a
15	F	32	1 (L)	Chair	0.063, 0.083, 0.056, 0.071, 0.046	n/a

16	F	24	1 (L)	Chair	0.063, 0.083, 0.056, 0.071, 0.046	n/a
17	F	25	1 (L)	Chair	0.063, 0.083, 0.056, 0.071, 0.046	n/a
18	F	25	1 (L)	Chair	0.063, 0.083, 0.056, 0.071, 0.046	n/a
19	F	27	1 (L)	Chair	0.063, 0.083, 0.056, 0.071, 0.046	n/a
20	F	24	1 (L)	Chair	0.063, 0.083, 0.056, 0.071, 0.046	n/a
21	F	27	1 (L)	Chair	0.063, 0.083, 0.056, 0.071, 0.046	n/a
22	M	51	1 (L)	Chair	0.036, 0.058, 0.080, 0.102, 0.124, 0.146, 0.168, 0.190	n/a

A3

Table A3 contains a summary of the patients that were enrolled in the study in the neurocritical care unit described in Chapter 4. Column 1 is the patient number. Column 2 indicates the patient's sex. Column 3 is the primary illness of the patient. Column 4 is the number of optical measurement sessions performed. Column 5 is the optical data quality rating with scores of 0-4 where 0 is the worst and 4 is the best. A score of 0 is for data that is not usable. A score of 1 is for data that is only usable in 30-60 second segments due to motion artifacts that occurred often. Scores of 2-4 indicate increasing quality of optical data and decreasing number of motion artifacts or issues with arterial blood pressure (BP) recordings. Column 6 contains notes with a further description of the reason for the particular rating of the data quality. In total, 67 measurements sessions were performed for this study. The results we present in Chapter 4 are for Patient 5. Patient 5 had the most coherent oscillations induced and therefore provided the best data for presenting our data analysis approach.

Table A.3. Summary of patients and experiments. ICP stands for intracranial pressure and BP stands for blood pressure.

Patient #	Female (F) or Male (M)	Primary Illness	# of measurements	Data quality	Notes
1	F	Chronic hydrocephalus	2	0	No ICP data, poor contact with optical probes
2	M	Traumatic brain injury, stroke in right hemisphere	9	2	No continuous BP, only spontaneous oscillations

3	M	Craniotomy for evacuation of hematoma	9	3	Issues with continuous BP, some induced oscillations
4	F	Infected shunt (hydrocephalus)	6	3	Issues with continuous BP, some induced oscillations
5	M	Intraventricular hemorrhage	9	4	Best measurements – especially for day 2
6	M	Shunt failure with post-op hemorrhage	6	2	Motion artifacts
7	F	Aneurysm in frontal lobe	2	2	Motion artifacts
8	F	Subarachnoid hemorrhage, vasospasm in the left hemisphere	8	1	Many motion artifacts
9	F	Subarachnoid hemorrhage from aneurysm	5	3	Good data quality but only spontaneous oscillations
10	F	Ruptured arteriovenous malformation (AVM)	3	2	Good data quality but not clear if oscillations were induced
11	F	Subarachnoid hemorrhage	1	1	Many motion artifacts, did not use cuffs due to patient discomfort
12	M	Brainstem stroke	7	4	Good data, did not induce many oscillations

References

[1] M. Zamir, *Hemo-Dynamics*. Springer, 2016.

[2] "Cerebrovasculaur Disease or Stroke," 2017. [Online]. Available: https://www.cdc.gov/nchs/fastats/stroke.htm.

[3] M. S. Vavilala, L. A. Lee, and A. M. Lam, "Cerebral blood flow and vascular physiology," *Anesthesiol. Clin N Am*, vol. 20, pp. 247–264, 2002.

[4] M. J. Cipolla, "The Cerebral Circulation," in *The Cerebral Circulation*, San Rafael, CA: Morgan & Claypool Life Sciences, 2009.

[5] J. Donnelly, K. P. Budohoski, P. Smielewski, and M. Czosnyka, "Regulation of the cerebral circulation: Bedside assessment and clinical implications," *Crit. Care*, vol. 18, pp. 1–17, 2016.

[6] P. Le Roux, "Invasive Neurological and Multimodality Monitoring in the NeuroICU," in *Textbook of Neurointensive Care*, A. J. Layon, A. Gabrielli, and W. A. Friedman, Eds. Springer London, 2013, pp. 127–145.

[7] N. A. Lassen, "Normal Average Value of Cerebral Blood Flow in Younger Adults Is 50 ml/100 g/min," *J. Cereb. Blood Flow Metab.*, vol. 5, pp. 347–349, 1985.

[8] S. Fantini, A. Sassaroli, K. T. Tgavalekos, and J. Kornbluth, "Cerebral blood flow and autoregulation: current measurement techniques and prospects for noninvasive optical methods," *Neurophotonics*, vol. 3, no. 3, p. 31411, 2016.

[9] M. Wintermark, M. Sesay, E. Barbier, K. Borbély, W. P. Dillon, J. D. Eastwood, T. C. Glenn, C. B. Grandin, S. Pedraza, J.-F. Soustiel, T. Nariai, G. Zaharchuk, J.-M. Caillé, V. Dousset, and H. Yonas, "Comparative overview of brain perfusion imaging techniques.," *Stroke*, vol. 36, no. 9, pp. e83-99, Sep. 2005.

[10] J. A. . Blokland, P. Trindev, M. P. . Stokkel, and E. K. . Pauwels, "Positron emission tomography: a technical introduction for clinicians," *Eur. J. Radiol.*, vol. 44, no. 1, pp. 70–75, Oct. 2002.

[11] R. Aaslid, T.-M. Markwalder, and H. Nornes, "Noninvasive transcranial Doppler ultrasound recording of flow velocity in basal cerebral arteries," *J. Neurosurgey*, vol. 57, no. 6, pp. 769–774, 1982.

[12] W. A. Friedman, *Textbook of Neurointensive Care*, 2nd ed. London: Springer London, 2013.

[13] R. Aaslid, K. F. Lindegaard, W. Sorteberg, and H. Nornes, "Cerebral autoregulation dynamics in humans," *Stroke*, vol. 20, pp. 45–52, Jan. 1989.

[14] J. A. Claassen, A. S. Meel-van den Abeelen, D. M. Simpson, and R. B. Panerai, "Transfer function analysis of dynamic cerebral autoregulation: A white paper from the International Cerebral Autoregulation Research Network," *J. Cereb. Blood Flow Metab.*, vol. 36, no. 4, pp. 665–80, Apr. 2016.

[15] A. H. van Beek, J. A. Claassen, M. G. O. Rikkert, and R. W. Jansen, “Cerebral autoregulation: an overview of current concepts and methodology with special focus on the elderly.,” *J. Cereb. Blood Flow Metab.*, vol. 28, no. 6, pp. 1071–85, Jun. 2008.

[16] T. S. Leung, I. Tachtsidis, M. Tisdall, M. Smith, D. T. Delpy, and C. E. Elwell, “Theoretical investigation of measuring cerebral blood flow in the adult human head using bolus Indocyanine Green injection and near-infrared spectroscopy,” *Appl. Opt.*, vol. 46, no. 10, p. 1604, 2007.

[17] B. Hallacoglu, A. Sassaroli, M. Wysocki, E. Guerrero-Berroa, M. Schnaider Beeri, V. Haroutunian, M. Shaul, I. H. Rosenberg, A. M. Troen, and S. Fantini, “Absolute measurement of cerebral optical coefficients, hemoglobin concentration and oxygen saturation in old and young adults with near-infrared spectroscopy,” *J. Biomed. Opt.*, vol. 17, no. 8, p. 81406, Aug. 2012.

[18] I. J. Bigio and S. Fantini, *Quantitative Biomedical Optics*. Cambridge University Press, 2016.

[19] M. Ferrari and V. Quaresima, “A brief review on the history of human functional near-infrared spectroscopy (fNIRS) development and fields of application,” *Neuroimage*, vol. 63, no. 2, pp. 921–35, Nov. 2012.

[20] B. J. Tromberg, B. W. Pogue, K. D. Paulsen, A. G. Yodh, D. A. Boas, and A. E. Cerussi, “Assessing the future of diffuse optical imaging technologies for breast cancer management,” *Med. Phys.*, vol. 35, no. 6, pp. 2443–2451, 2008.

[21] S. Fantini and A. Sassaroli, “Near-infrared optical mammography for breast cancer detection with intrinsic contrast,” *Ann. Biomed. Eng.*, vol. 40, no. 2, pp. 398–407, Mar. 2012.

[22] S. J. Matcher, C. E. Elwell, C. E. Cooper, M. Cope, and D. T. Delpy, “Performance Comparison of Several Published Tissue Near-Infrared Spectroscopy Algorithms,” *Anal. Biochem.*, vol. 227, pp. 54–68, 1995.

[23] A. Villringer and B. Chance, “Non-invasive optical spectroscopy and imaging of human brain function,” *Trends Neurosci.*, vol. 20, no. 10, pp. 435–42, Oct. 1997.

[24] W. B. Baker, “Optical Cerebral Blood Flow Monitoring of Mice To Men,” University of Pennsylvania, 2015.

[25] S. Fantini, “A new hemodynamic model shows that temporal perturbations of cerebral blood flow and metabolic rate of oxygen cannot be measured individually using functional near-infrared spectroscopy.,” *Physiol. Meas.*, vol. 35, no. 1, pp. N1-9, Jan. 2014.

[26] S. Fantini, D. Hueber, M. A. Franceschini, E. Gratton, W. Rosenfeld, P. G. Stubblefield, D. Maulik, and M. R. Stankovic, “Non-invasive optical monitoring of the newborn piglet brain using continuous-wave and frequency-domain spectroscopy,” *Phys. Med. Biol.*, vol. 44, no. 6, pp. 1543–63, Jun. 1999.

[27] S. Fantini, M. A. Franceschini, J. B. Fishkin, B. Barbieri, and E. Gratton, “Quantitative determination of the absorption spectra of chromophores in strongly scattering media: a light-emitting-diode based technique.,” *Appl. Opt.*, vol. 33, no. 22, pp. 5204–13, Aug. 1994.

[28] S. Fantini, M. A. Franceschini-Fantini, J. S. Maier, S. A. Walked, B. Barbieri, and E. Gratton, “Frequency-domain multichannel optical detector for noninvasive tissue spectroscopy and oximetry,” *Opt. Eng.*, vol. 34, no. 1, p. 32, 1995.

[29] M. Reinhard, F. K. Schumacher, S. Rutsch, M. Oeinck, J. Timmer, I. Mader, B. Schelter, C. Weiller, and C. P. Kaller, “Spatial mapping of dynamic cerebral autoregulation by multichannel near-infrared spectroscopy in high-grade carotid artery disease.,” *J. Biomed. Opt.*, vol. 19, no. 9, p. 97005, Sep. 2014.

[30] R. Aaslid, M. Blaha, G. Sviri, C. M. Douville, and D. W. Newell, “Asymmetric dynamic cerebral autoregulatory response to cyclic stimuli,” *Stroke*, vol. 38, no. 5, pp. 1465–9, May 2007.

[31] J. A. H. R. Claassen, B. D. Levine, and R. Zhang, “Dynamic cerebral autoregulation during repeated squat-stand maneuvers,” *J. Appl. Physiol.*, vol. 106, pp. 153–60, Jan. 2009.

[32] M. Reinhard, E. Wehrle-Wieland, D. Grabiak, M. Roth, B. Guschlbauer, J. Timmer, C. Weiller, and A. Hertzel, “Oscillatory cerebral hemodynamics-the macro- vs. microvascular level,” *J. Neurol. Sci.*, vol. 250, pp. 103–9, Dec. 2006.

[33] M. L. Pierro, A. Sassaroli, P. R. Bergethon, B. L. Ehrenberg, and S. Fantini, “Phase-amplitude investigation of spontaneous low-frequency oscillations of cerebral hemodynamics with near-infrared spectroscopy: A sleep study in human subjects,” *Neuroimage*, vol. 63, no. 3, pp. 1571–84, Nov. 2012.

[34] S. Fantini, “Dynamic model for the tissue concentration and oxygen saturation of hemoglobin in relation to blood volume, flow velocity, and oxygen consumption: implications for functional neuroimaging and coherent hemodynamics spectroscopy (CHS),” *Neuroimage*, vol. 85, pp. 202–21, Jan. 2013.

[35] J. M. Kainerstorfer, A. Sassaroli, K. T. Tgavalekos, and S. Fantini, “Cerebral autoregulation in the microvasculature measured with near-infrared spectroscopy.,” *J. Cereb. Blood Flow Metab.*, pp. 1–8, Feb. 2015.

[36] M. L. Pierro, J. M. Kainerstorfer, A. Civiletto, D. E. Weiner, A. Sassaroli, B. Hallacoglu, and S. Fantini, “Reduced speed of microvascular blood flow in hemodialysis patients versus healthy controls: a coherent hemodynamics spectroscopy study,” *J. Biomed. Opt.*, vol. 19, no. 2, pp. 26005-1-26005–9, Feb. 2014.

[37] S. Fantini, A. Sassaroli, J. M. Kainerstorfer, K. T. Tgavalekos, and X. Zang, “Non-invasive assessment of cerebral microcirculation with diffuse optics and coherent hemodynamics spectroscopy,” *Proc. SPIE*, vol. 9690B, 2016.

[38] A. Bruns, “Fourier-, Hilbert- and wavelet-based signal analysis: are they really different approaches?,” *J. Neurosci. Methods*, vol. 137, no. 2, pp. 321–32, Aug. 2004.

[39] C. H. Schmitz, D. P. Klemer, R. Hardin, M. S. Katz, Y. Pei, H. L. Graber, M. B. Levin, R. D. Levina, N. A. Franco, W. B. Solomon, and R. L. Barbour, “Design and implementation of dynamic near-infrared optical tomographic imaging instrumentation for simultaneous dual-breast measurements,” *Appl. Opt.*, vol. 44, no. 11, pp. 2140–53, 2005.

[40] S. A. Carp, J. Selb, Q. Fang, R. Moore, D. B. Kopans, and D. A. Boas, “Dynamic functional and mechanical response of breast tissue to compression.,” *Opt. Express*, vol. 16, no. 20, pp. 16064–78, 2008.

[41] C. M. Carpenter, R. Rakow-Penner, S. Jiang, B. L. Daniel, B. W. Pogue, G. H. Glover, and K. D. Paulsen, “Inspired gas-induced vascular change in tumors with magnetic-resonance-guided near-infrared imaging: human breast pilot study,” *J. Biomed. Opt.*, vol. 15, no. 3, pp. 3026-1-3026–5, 2010.

[42] M. L. Flexman, H. K. Kim, J. E. Gunther, E. A. Lim, M. C. Alvarez, E. Desperito, K. Kalinsky, D. L. Hershman, and A. H. Hielscher, “Optical biomarkers for breast cancer derived from dynamic diffuse optical tomography,” *J. Biomed. Opt.*, vol. 18, no. 9, pp. 96012-1-96012–9, Sep. 2013.

[43] T. Parks and J. McClellan, “Chebyshev Approximation for Nonrecursive Digital Filters with Linear Phase,” *IEEE Trans. Circuit Theory*, vol. 19, no. 2, pp. 189–194, 1972.

[44] B. Boashash, “Estimating and interpreting the instantaneous frequency of a signal-part 1 : fundamentals,” *Proc. IEEE*, vol. 80, no. 4, pp. 520–538, 1992.

[45] M. L. Pierro, B. Hallacoglu, A. Sassaroli, J. M. Kainerstorfer, and S. Fantini, “Validation of a novel hemodynamic model for coherent hemodynamics spectroscopy (CHS) and functional brain studies with fNIRS and fMRI.,” *Neuroimage*, vol. 85, pp. 222–33, Jan. 2014.

[46] J. M. Kainerstorfer, A. Sassaroli, and S. Fantini, “Coherent hemodynamics spectroscopy in a single step,” *Biomed. Opt. Express*, vol. 5, no. 10, pp. 3403–3616, 2014.

[47] J. M. Kainerstorfer, A. Sassaroli, B. Hallacoglu, M. L. Pierro, and S. Fantini, “Practical steps for applying a new dynamic model to near-infrared spectroscopy measurements of hemodynamic oscillations and transient changes: implications for cerebrovascular and functional brain studies,” *Acad. Radiol.*, vol. 21, no. 2, pp. 185–96, Feb. 2014.

[48] J. H. Zar, “Circular Distributions,” in *Biostatistical Analysis*, 5th ed., Upper Saddle River: Pearson Prentice Hall, 2010, pp. 612–623.

[49] M. A. Franceschini, D. A. Boas, A. Zourabian, S. G. Diamond, S. Nadgir, D. W.

Lin, J. B. Moore, and S. Fantini, “Near-infrared spiroximetry: noninvasive measurements of venous saturation in piglets and human subjects,” *J. Appl. Physiol.*, vol. 92, pp. 372–384, 2002.

[50] C. W. Yoxail and A. M. Weindling, “Measurement of venous oxyhaemoglobin saturation in the adult human forearm by near infrared spectroscopy with venous occlusion,” *Med. Biol. Eng. Comput.*, vol. 35, pp. 331–336, 1997.

[51] A. Samani, J. Zubovits, and D. Plewes, “Elastic moduli of normal and pathological human breast tissues: an inversion-technique-based investigation of 169 samples.,” *Phys. Med. Biol.*, vol. 52, no. 6, pp. 1565–76, Mar. 2007.

[52] P. Vaupel, F. Kallinowski, and P. Okunieff, “Blood flow, oxygen and nutrient supply, and metabolic microenvironment of human tumors: a review.,” *Cancer Res.*, vol. 49, no. 23, pp. 6449–65, Dec. 1989.

[53] J. M. Kainerstorfer, A. Sassaroli, and S. Fantini, “Optical oximetry of volume-oscillating vascular compartments: Contributions from oscillatory blood flow,” *J. Biomed. Opt.*, vol. 21, no. 10, 2016.

[54] L. Rivera-Lara, A. Zorrilla-Vaca, R. G. Geocadin, R. J. Healy, W. Ziai, and M. A. Mirski, “Cerebral Autoregulation-Oriented Therapy at the Bedside A Comprehensive Review,” *Anesthesiology*, vol. 126, pp. 1187–1199, 2017.

[55] M. Czosnyka, P. J. Hutchinson, M. Balestreri, M. Hiller, P. Smielewski, and J. D. Pickard, “Monitoring and interpretation of intracranial pressure after head injury,” *Acta Neurochir. Suppl.*, vol. 96, no. 114–8, 2006.

[56] J. K. Lee, K. K. Kibler, P. B. Benni, R. B. Easley, M. Czosnyka, P. Smielewski, R. C. Koehler, D. H. Shaffner, and K. M. Brady, “Cerebrovascular Reactivity Measured by Near-Infrared Spectroscopy,” *Stroke*, vol. 40, no. 5, pp. 1820–6, May 2009.

[57] J. Diedler, C. Zweifel, K. P. Budohoski, M. Kasprowicz, E. Sorrentino, C. Haubrich, K. M. Brady, M. Czosnyka, J. D. Pickard, and P. Smielewski, “The Limitations of Near-Infrared Spectroscopy to Assess Cerebrovascular Reactivity: The Role of Slow Frequency Oscillations,” *Anesth. Analg.*, vol. 113, no. 4, pp. 849–57, Oct. 2011.

[58] C. Zweifel, G. Castellani, M. Czosnyka, A. Helmy, A. Manktelow, E. Carrera, K. M. Brady, P. J. A. Hutchinson, D. K. Menon, J. D. Pickard, and P. Smielewski, “Noninvasive Monitoring of Cerebrovascular Reactivity with Near Infrared Spectroscopy in Head-Injured Patients,” *J. Neurotrauma*, vol. 27, pp. 1951–8, Nov. 2010.

[59] C.-A. Porret, N. Stergiopulos, and J.-J. Meister, “Flow-driven Diameter Response in Rat Femoral Arteries Perfused In Vitro,” *Ann. Biomed. Eng.*, vol. 26, pp. 526–533, 1998.

[60] M. Jacob, D. Chappell, and B. F. Becker, “Regulation of blood flow and volume

exchange across the microcirculation," *Crit. Care*, vol. 20, pp. 1–13, 2016.

[61] K. P. Budohoski, M. Czosnyka, N. De Riva, P. Smielewski, J. D. Pickard, D. K. Menon, P. J. Kirkpatrick, and A. Lavinio, "The relationship between cerebral blood flow autoregulation and cerebrovascular pressure reactivity after traumatic brain injury," *Neurosurgery*, vol. 71, no. 3, pp. 652–660, 2012.

[62] P. Nissen, H. Pacino, H. J. Frederiksen, S. Novovic, and N. H. Secher, "Near-infrared Spectroscopy for Evaluation of Cerebral Autoregulation During Orthotopic Liver Transplantation," *Neurocrit. Care*, vol. 11, pp. 235–41, Jan. 2009.

[63] K. P. Budohoski, C. Zweifel, M. Kasprowicz, E. Sorrentino, J. Diedler, K. M. Brady, P. Smielewski, D. K. Menon, J. D. Pickard, P. J. Kirkpatrick, and M. Czosnyka, "What comes first? The dynamics of cerebral oxygenation and blood flow in response to changes in arterial pressure and intracranial pressure after head injury," *Br. J. Anaesth.*, vol. 108, no. 1, pp. 89–99, Jan. 2012.

[64] C. Zweifel, G. Castellani, M. Czosnyka, E. Carrera, K. M. Brady, P. J. Kirkpatrick, J. D. Pickard, and P. Smielewski, "Continuous Assessment of Cerebral Autoregulation with Near-Infrared Spectroscopy in Adults after Subarachnoid Hemorrhage," *Stroke*, vol. 41, pp. 1963–8, Sep. 2010.

[65] K. Brady, B. Joshi, C. Zweifel, P. Smielewski, M. Czosnyka, B. R. Easley, and C. W. Hogue Jr, "Real-time continuous monitoring of cerebral blood flow autoregulation using near-infrared spectroscopy in patients undergoing cardiopulmonary bypass," vol. 344, no. 6188, pp. 1173–1178, 2015.

[66] D. Hori, C. W. Hogue, A. Shah, C. Brown, K. J. Neufeld, J. V. Conte, J. Price, C. Sciortino, L. Max, A. Laflam, H. Adachi, D. E. Cameron, and K. Mandal, "Cerebral Autoregulation Monitoring with Ultrasound-Tagged Near-Infrared Spectroscopy in Cardiac Surgery Patients," *Anesth. Analg.*, vol. 121, no. 5, pp. 1187–93, Nov. 2015.

[67] L. A. Steiner, D. Pfister, S. P. Strebel, D. Radolovich, P. Smielewski, and M. Czosnyka, "Near-Infrared Spectroscopy can Monitor Dynamic Cerebral Autoregulation in Adults," *Neurocrit. Care*, vol. 10, pp. 122–8, Jan. 2009.

[68] A. B. Parthasarathy, K. P. Gannon, W. B. Baker, C. G. Favilla, R. Balu, S. E. Kasner, A. G. Yodh, J. A. Detre, and M. T. Mullen, "Dynamic autoregulation of cerebral blood flow measured non-invasively with fast diffuse correlation spectroscopy," *J. Cereb. Blood Flow Metab.*, 2017.

[69] E. Carrera, D.-J. Kim, G. Castellani, C. Zweifel, P. Smielewski, J. D. Pickard, and M. Czosnyka, "Effect of Hyper- and Hypocapnia on Cerebral Arterial Compliance in Normal Subjects," *J. Neuroimaging*, vol. 21, pp. 121–125, 2011.

[70] M. Fabiani, K. A. Low, C.-H. Tan, B. Zimmerman, M. A. Fletcher, N. Schneider-Garces, E. L. Maclin, A. M. Chiarelli, B. P. Sutton, and G. Gratton, "Taking the pulse of aging: Mapping pulse pressure and elasticity in cerebral arteries with

optical methods," *Psychophysiology,* vol. 51, pp. 1072–1088, 2014.

[71] C. H. Tan, K. A. Low, T. Kong, M. A. Fletcher, B. Zimmerman, E. L. Maclin, A. M. Chiarelli, G. Gratton, and M. Fabiani, "Mapping cerebral pulse pressure and arterial compliance over the adult lifespan with optical imaging," *PLoS One,* vol. 12, no. 2, 2017.

[72] Y.-C. Tzeng and P. N. Ainslie, "Blood pressure regulation IX: cerebral autoregulation under blood pressure challenges.," *Eur. J. Appl. Physiol.*, vol. 114, no. 3, pp. 545–59, Mar. 2014.

[73] R. Zhang, J. H. Zuckerman, C. A. Giller, and B. D. Levine, "Transfer function analysis of dynamic cerebral autoregulation in humans," *Am. J. Physiol.*, vol. 274, no. 1, pp. 233–241, 1998.

[74] P. Kvandal, L. Sheppard, S. A. Landsverk, A. Stefanovska, and K. A. Kirkeboen, "Impaired cerebrovascular reactivity after acute traumatic brain injury can be detected by wavelet phase coherence analysis of the intracranial and arterial blood pressure signals," *J. Clin. Monit. Comput.*, vol. 27, no. 4, pp. 375–383, 2013.

[75] H. Obrig, M. Neufang, R. Wenzel, M. Kohl, J. Steinbrink, K. Einhäupl, and A. Villringer, "Spontaneous Low Frequency Oscillations of Cerebral Hemodynamics and Metabolism in Human Adults," *Neuroimage,* vol. 12, no. 6, pp. 623–39, Dec. 2000.

[76] K. T. Tgavalekos, J. M. Kainerstorfer, A. Sassaroli, and S. Fantini, "Blood-pressure-induced oscillations of deoxy- and oxyhemoglobin concentrations are in-phase in the healthy breast and out-of-phase in the healthy brain," *J. Biomed. Opt.*, vol. 21, no. 10, p. 101410, Oct. 2016.

[77] D. M. Hueber, S. Fantini, A. E. Cerussi, and B. Barbieri, "New Optical Probe Designs for Absolute (Self-calibrating) NIR Tissue Hemoglobin Measurements," *Proc SPIE Opt. Tomogr. Spectrosc. Tissue III,* vol. 3597, pp. 618–631, 1999.

[78] P. D. Welch, "The Use of Fast Fourier Transform for the Estimation of Power Spectra: A Method Based on Time Averaging Over Short, Modified Periodograms," *IEEE Trans. Audio and Electroacoustic,* vol. AU-15. pp. 70–73, 1967.

[79] A. Sassaroli, K. Tgavalekos, and S. Fantini, "The meaning of 'coherent' and its quantification in coherent hemodynamics spectroscopy," *Prep.*, 2018.

[80] L. Ljung, *System Identification: Theory for the User*. Englewood Cliffs: PTR Prentice Hall, 1987.

[81] J. M. Bland and D. G. Altman, "Statistical Methods for Assessing Agreement Between Two Methods of Clinical Measurement," *Lancet,* vol. 8, no. 1, pp. 307–10, 1986.

[82] M. Orini, R. Bailón, L. T. Mainardi, P. Laguna, and P. Flandrin, "Characterization of Dynamic Interactions Between Cardiovascular Signals by Time-Frequency

Coherence," *IEEE Trans. Biomed. Eng.*, vol. 59, no. 3, pp. 663–673, 2012.

[83] Z. Li, M. Zhang, Q. Xin, J. Li, G. Chen, F. Liu, and J. Li, "Correlation analysis between prefrontal oxygenation oscillations and cerebral artery hemodynamics in humans," *Microvasc. Res.*, vol. 82, pp. 304–310, 2011.

[84] A. B. Rowley, S. J. Payne, I. Tachtsidis, M. J. Ebden, J. P. Whiteley, D. J. Gavaghan, L. Tarassenko, M. Smith, C. E. Elwell, and D. T. Delpy, "Synchronization between arterial blood pressure and cerebral oxyhaemoglobin concentration investigated by wavelet cross-correlation," *Physiol. Meas.*, vol. 28, pp. 161–173, 2007.

[85] F. Tian, T. Tarumi, H. Liu, R. Zhang, and L. Chalak, "Wavelet coherence analysis of dynamic cerebral autoregulation in neonatal hypoxic-ischemic encephalopathy," *NeuroImage Clin.*, vol. 11, pp. 124–32, Jan. 2016.

[86] Y. Gao, M. Zhang, Q. Han, W. Li, Q. Xin, Y. Wang, and Z. Li, "Cerebral autoregulation in response to posture change in elderly subjects-assessment by wavelet phase coherence analysis of cerebral tissue oxyhemoglobin concentrations and arterial blood pressure signals," *Behav. Brain Res.*, vol. 278, pp. 330–6, Feb. 2015.

[87] P. S. Addison, "A Review of Wavelet Transform Time-Frequency Methods for NIRS-Based Analysis of Cerebral Autoregulation," *IEEE Rev. Biomed. Eng.*, vol. 8, pp. 78–85, 2015.

[88] C. R. Ilvedson, "Transfer Function Estimation Using Time-Frequency Analysis," Massachusetts Institute of Technology, 1996.

[89] E. Feron, M. Brenner, J. Paduano, and A. Turevskiy, "Time-Frequency Analysis for Transfer Function Estimation and Application to Flutter Clearance," *J. Guid. Control. Dyn.*, vol. 21, no. 3, pp. 375–382, May 1998.

[90] M. Nitzan, B. Khanokh, and Y. Slovik, "The difference in pulse transit time to the toe and finger measured by photoplethysmography," *Physiol. Meas.*, vol. 23, pp. 85–93, 2002.

[91] P. M. Nabeel, J. Jayaraj, and S. Mohanasankar, "Single-source PPG-based local pulse wave velocity measurement : a potential cuffless blood pressure estimation technique," *Physiol. Meas.*, vol. 38, pp. 2122–2140, 2017.

[92] C. M. Rovainen, T. A. Woolsey, N. C. Blocher, D.-B. Wang, and O. F. Robinson, "Blood Flow in Single Surface Arterioles and Venules on the Mouse Somatosensory Cortex Measured with Videomicroscopy, Fluorescent Dextrans, Nonoccluding Fluorescent Beads, and Computer-Assisted Image Analysis," *J. Cereb. Blood Flow Metab.*, vol. 13, pp. 359–371, 1993.

[93] R. Aaslid, D. W. Newell, R. Stooss, W. Sorteberg, and K.-F. Lindegaard, "Assessment of Cerebral Autoregulation Dynamics From Simultaneous Arterial and Venous Transcranial Doppler Recordings in Humans," *Stroke*, vol. 22, no. 9,

pp. 1148–1155, 1991.

[94] S.-P. Lee, T. Q. Duong, G. Yang, C. Iadecola, and S.-G. Kim, "Relative Changes of Cerebral Arterial and Venous Blood Volumes During Increased Cerebral Blood Flow: Implications for BOLD fMRI," *Magn. Reson. Med.*, vol. 45, pp. 791–800, May 2001.

[95] M. J. P. Barrett, M. H. Tawhai, and V. Suresh, "Arteries dominate volume changes during brief functional hyperemia: Evidence from mathematical modelling," *Neuroimage*, vol. 62, pp. 482–492, 2012.

[96] T. Kim and S.-G. Kim, "Temporal dynamics and spatial specificity of arterial and venous blood volume changes during visual stimulation: implication for BOLD quantification," *J. Cereb. Blood Flow Metab.*, vol. 31, pp. 1211–1222, 2011.

[97] H. Ito, I. Kanno, H. Iida, J. Hatazawa, E. Shimosegawa, H. Tamura, and T. Okudera, "Arterial fraction of cerebral blood volume in humans measured by positron emission tomography," *Ann. Nucl. Med.*, vol. 15, no. 2, pp. 111–116, 2001.

[98] J.-J. Wang, J. A. Flewitt, N. G. Shrive, K. H. Parker, and J. V. Tyberg, "Systemic venous circulation. Waves propagating on a windkessel: relation of arterial and venous windkessels to systemic vascular resistance," *Am J Physiol Hear. Circ Physiol*, vol. 290, pp. H154–H162, 2005.

[99] C. D. Fraser III, K. M. Brady, C. J. Rhee, R. B. Easley, K. Kibler, P. Smielewski, M. Czosnyka, D. W. Kaczka, D. B. Andropoulos, and C. Rusin, "The frequency response of cerebral autoregulation," *J. Appl. Physiol.*, vol. 115, pp. 52–6, Jul. 2013.

[100] A. B. Rowley, S. J. Payne, I. Tachtsidis, M. J. Ebden, J. P. Whiteley, D. J. Gavaghan, L. Tarassenko, M. Smith, C. E. Elwell, and D. T. Delpy, "Synchronization between arterial blood pressure and cerebral oxyhaemoglobin concentration investigated by wavelet cross-correlation," *Physiol. Meas.*, vol. 28, pp. 161–173, 2007.

[101] S. J. Payne, J. Selb, and D. A. Boas, "Effects of Autoregulation and CO2 Reactivity on Cerebral Oxygen Transport," *Ann. Biomed. Eng.*, vol. 37, no. 11, pp. 2288–2298, 2009.

[102] C. M. Quick, D. S. Berger, and A. Noordergraaf, "Appartent arterial compliance," *Am. J. Physiol*, vol. 274, pp. H1393–H1403, 1998.

[103] C. M. Quick, D. S. Berger, D. A. Hettrick, and A. Noordergraaf, "True Arterial System Compliance Estimated From Apparent Arterial Compliance," *Ann. Biomed. Eng.*, vol. 28, pp. 291–301, 2000.

[104] W. B. Baker, A. B. Parthasarathy, K. P. Gannon, V. C. Kavuri, D. R. Busch, K. Abramson, L. He, R. C. Mesquita, M. T. Mullen, J. A. Detre, J. H. Greenberg, D. J. Licht, R. Balu, W. A. Kofke, and A. G. Yodh, "Noninvasive optical monitoring

of critical closing pressure and arteriole compliance in human subjects," *J. Cereb. Blood Flow Metab.*, p. 0271678X1770916, 2017.

[105] R. Zhang, K. Behbehani, and B. D. Levine, "Dynamic pressure-flow relationship of the cerebral circulation during acute increase in arterial pressure," *J. Physiol.*, vol. 587, no. 11, pp. 2567–2577, 2009.

[106] H. Ito, M. Ibaraki, I. Kanno, H. Fukuda, and S. Miura, "Changes in the arterial fraction of human cerebral blood volume during hypercapnia and hypocapnia measured by positron emission tomography," *J. Cereb. Blood Flow Metab.*, vol. 25, pp. 852–7, Jul. 2005.

[107] M. Kasprowicz, J. Diedler, M. Reinhard, E. Carrera, L. A. Steiner, P. Smielewski, K. P. Budohoski, C. Haubrich, J. D. Pickard, and M. Czosnyka, "Time Constant of the Cerebral Arterial Bed in Normal Subjects," *Ultrasound Med. Biol.*, vol. 38, no. 7, pp. 1129–1137, 2012.

[108] S. J. Payne, J. Mohammad, M. M. Tisdall, and I. Tachtsidis, "Effects of arterial blood gas levels on cerebral blood flow and oxygen transport," *Biomed. Opt. Express*, vol. 2, no. 4, p. 966, Mar. 2011.

[109] X. Hu, A. A. Alwan, E. H. Rubinstein, and M. Bergsneider, "Reduction of compartment compliance increases venous flow pulsatility and lowers apparent vascular compliance : Implications for cerebral blood flow hemodynamics," *Med. Eng. Phys.*, vol. 28, pp. 304–314, 2006.

[110] G. L. Baumbach and D. D. Heistad, "Regional, segmental, and temporal heterogeneity of cerebral vascular autoregulation," *Ann. Biomed. Eng.*, vol. 13, pp. 303–310, 1985.

[111] O. Onaizah, T. L. Poepping, and M. Zamir, "A model of blood supply to the brain via the carotid arteries: Effects of obstructive vs . sclerotic changes," *Med. Eng. Phys.*, vol. 49, pp. 121–130, 2017.

[112] C. A. Figueroa and J. D. Humphrey, "Pressure wave propagation in full-body arterial models : A gateway to exploring aging and hypertension," *Procedia IUTAM*, vol. 10, pp. 382–395, 2014.

[113] L. A. Steiner, J. P. Coles, M. Czosnyka, P. S. Minhas, T. D. Fryer, F. I. Aigbirhio, J. C. Clark, P. Smielewski, D. A. Chatfield, T. Donovan, J. D. Pickard, and D. K. Menon, "Cerebrovascular pressure reactivity is related to global cerebral oxygen metabolism after head injury," *J Neurol Neurosurg Psychiatry*, vol. 74, pp. 765–770, 2003.

[114] E. Carrera, L. a Steiner, G. Castellani, P. Smielewski, C. Zweifel, C. Haubrich, J. D. Pickard, D. K. Menon, and M. Czosnyka, "Changes in cerebral compartmental compliances during mild hypocapnia in patients with traumatic brain injury.," *J. Neurotrauma*, vol. 28, no. 6, pp. 889–96, 2011.

[115] M. Reinhard, F. K. Schumacher, S. Rutsch, M. Oeinck, J. Timmer, I. Mader, B.

Schelter, C. Weiller, and C. P. Kaller, “Spatial mapping of dynamic cerebral autoregulation by multichannel near-infrared spectroscopy in high-grade carotid artery disease,” *J. Biomed. Opt.*, vol. 19, no. 9, p. 97005, Sep. 2014.

[116] K. Khaksari, K. Tgavalekos, A. Sassaroli, and S. Fantini, “Depth-Resolved Measurements of Oscillatory Hemodynamics in Cerebral Near-Infrared Spectroscopy,” *Prep.*, 2018.

[117] B. Efron and R. J. Tibshirani, *An Introduction to the Bootstrap*, 1st ed. Dordrecht: Springer-Science+Business Media, 1993.

[118] K. T. Tgavalekos, A. Sassaroli, X. Cai, J. Kornbluth, and S. Fantini, “Coherent hemodynamics spectroscopy: initial applications in the neurocritical care unit,” *Proc. SPIE*, 2017.

[119] J. S. Meyer, F. Gotoh, Y. Takagi, and R. Kakimi, “Cerebral Hemodynamics, Blood Gases , and Electrolytes during Breath-Holding and the Valsalva Maneuver,” *Circulation*, pp. 35–48, 1966.

[120] C. Gilbert, “Hyperventilation and the body,” *Accid. Emerg. Nurs.*, vol. 7, no. 3, pp. 130–140, Jul. 1999.

[121] R. L. Grubb, M. E. Raichle, J. O. Eichling, and M. M. Ter-Pogossian, “The Effects of Changes in PaCO2 on Cerebral Blood Volume , Blood Flow , and Vascular Mean Transit Time,” *Stroke*, vol. 5, pp. 630–639, 1974.

[122] J. J. Chen and G. B. Pike, “Global cerebral oxidative metabolism during hypercapnia and hypocapnia in humans: implications for BOLD fMRI,” *J. Cereb. Blood Flow Metab.*, vol. 30, no. 6, pp. 1094–9, Jun. 2010.

[123] J. W. Elting, M. J. H. Aries, J. H. van der Hoeven, P. C. A. J. Vroomen, and N. M. Maurits, “Reproducibility and variability of dynamic cerebral autoregulation during passive cyclic leg raising,” *Med. Eng. Phys.*, vol. 36, pp. 585–591, 2014.

[124] J. W. Hamner, M. A. Cohen, S. Mukai, L. A. Lipsitz, and J. A. Taylor, “Spectral indices of human cerebral blood flow control: responses to augmented blood pressure oscillations,” *J. Physiol.*, vol. 559, no. 3, pp. 965–73, Sep. 2004.

[125] E. Katsogridakis, G. Bush, L. Fan, A. A. Birch, D. M. Simpson, R. Allen, J. F. Potter, and R. B. Panerai, “Detection of impaired cerebral autoregulation improves by increasing arterial blood pressure variability,” *J Cereb Blood Flow Metab*, vol. 33, no. 4, pp. 519–523, 2013.

[126] H. Watanabe, Y. Shitara, Y. Aoki, T. Inoue, S. Tsuchida, N. Takahashi, and G. Taga, “Hemoglobin phase of oxygenation and deoxygenation in early brain development measured using fNIRS,” *Proc. Natl. Acad. Sci.*, vol. 114, no. 9, pp. E1737–E1744, 2017.